A Piezoelectric Translational Flow Agitator for Active Air Cooling of Electronics

A DISSERTATION
SUBMITTED TO THE FACULTY OF THE GRADUATE SCHOOL
OF THE UNIVERSITY OF MINNESOTA
BY

TAIHO YEOM

IN PARTIAL FULFILLMENT OF THE REQUIREMENTS
FOR THE DEGREE OF
DOCTOR OF PHILOSOPHY

TIANHONG CUI, TERRENCE W. SIMON

AUGUST, 2012

Acknowledgements

Financial support of this work was provided in part by the Defense Advanced Research Projects Agency (DARPA) through the MACE Program. I appreciate for their support.

I would like to give special thanks to my advisors, Prof. Tianhong Cui and Prof. Terry Simon, for their generous support and guidance for my PhD study. They have always encouraged and inspired me to keep progress whenever I feel difficulties and lack of knowledge. Many thanks go to my PhD committee members for their guidance and patience. I also very much appreciate Prof. Frank Kelso for his useful and invaluable comments on developing theoretical analyses of this study. I also would like to thank the students and the postdocs who worked on the MACE project for their help and discussions: Dr. Min Zhang, Dr. Youmin Yu, Dr. Xuelin Zhu, Dr. Tao Zhang, Dr. Congshun Wang, Smita Agrawal, and Longzhong Huang. I am also grateful to Dr. North and many others at Thermacore who have assisted me in this work for preparing many experimental facilities.

Finally, I would like to give my deep gratitude to my parents for their endless support throughout my life. I appreciate the patience and encouragement provided by my wife, Sohye, during my PhD study. I thank to my son, Jihoon, for refreshing my tired body and mind with beautiful smile everyday ever since he was born.

To all of these wonderful people, I am pleased to express my gratitude.

Taiho Yeom

Abstract

A Piezoelectric Translational Flow Agitator for Active Air Cooling of Electronics

As heat dissipation from electronic components dramatically increases due to the rapid development of integrated circuits with micro-nano fabrication, the need increases for powerful cooling facilities. Different cooling schemes such as liquid cooling, direct sprays, boiling heat transfer, etc. have been developed to meet the needs of heat removal. Air cooling still has potential for improvement and continues to hold many advantages over liquid cooling in terms of simplicity, reliability, cost, etc. Conventional heat sink systems with blowers or fans are approaching maximum thermal management capability due to dramatically increased heat dissipation from the chips of high power electronics. In order to increase thermal performance of air-cooled heat sink systems, more active or passive cooling components are continually being considered.

One technique is to agitate the flow in the heat sinks to replace or aid conventional blowers. In the present study, an active heat sink system that is coupled with a piezoelectric translational agitator and micro pin fin arrays on the heat sink surfaces is considered. The piezoelectric translational agitator generates high frequency and large displacement motion to a blade. It is driven by an oval loop shell that amplifies the small displacement of the piezo stack actuator to the several-millimeter range. Detailed vibration characteristics were studied through theoretical and experimental analyses. Dynamic operating frequency and displacement were estimated through the theoretical analysis. The blade, made of carbon fiber composite, is easily extended to a multiple-blade system without adding much mass. The micro pin fin arrays were created with the LIGA photolithography technique. The cooling performance of the heat sink system was demonstrated in single-channel and multiple-channel test facilities employing either plain or micro pin-fin surfaces. Intensive heat transfer experimental results are provided. A total Reynolds number was defined to characterize the combined effects of cross flow and agitation. The Stanton number developed from the relationship between the total Reynolds number and heat transfer coefficients enables predicting operating performance. Different configurations of the translational agitator with multiple blades were fabricated and tested in a 26-channel, full-size heat sink. The experimental results showed that the proposed active air cooling has a promising potential for the thermal management of high power electronics.

Table of Contents

List of Tables

List of Figures

Figure Page

Nomenclatures

A	Convection surface area
A_{actual}	Actual increased convection area due to micro pin fins
A_{base}	Base area of micro pin fin plate
A_b	Blade area
A_c	Cross sectional area of copper block
A_{sink}	Convection surface area of the virtual active heat sink
A_{conv}	Convection surface area of the single channel heat sink
a	Height of the arc beam of the oval loop shell structure
b	Length of the arc beam of the oval loop shell structure
c	Specific heat of air
COP	Coefficient of Performance
CFM	Cubic feet per minute
D_b	Hydraulic diameter of the blade
D_h	Hydraulic diameter of the channel
D	Pin fin diameter
f	Friction factor
$f_{L1,L2}$	Friction factor of upstream and downstream extensions of single channel
f_p	Friction factor of plain copper surface
g	Standard gravity
h	Heat transfer coefficient
H	Pin fin height
H1	Channel height
K_h	Spring constant of the oval loop shell in the horizontal direction
$K_{loss,inlet}$	Inlet loss coefficient
K_v	Spring constant of the oval loop shell in the vertical direction
k	Thermal conductivity of copper
k_p	Thermal conductivity of thermal paste
k_{air}	Thermal conductivity of air
l	Distance between convection surface and temperature measuring point
LPM	Liters per minute
LMTD	Log mean temperature difference
L_{pre}	Pre-stressed length of the oval loop shell structure
$\dot{m}$	Mass flow rate
M	Moment
N	Normal force
N_{mp}	Number of pin fins
Nu	Nusselt number
Nu_p	Nusselt number of plain copper surface
P	Force from the PZT stack actuator
P_{static}	Static pressure
P_{total}	Total pressure
P_{to}	Total power consumption of the active heat sink

P_{blower}	Blower power consumption
$P_{agitator}$	Agitator power consumption
ΔP_{static}	Static pressure drop
ΔP_{total}	Total pressure drop
ΔP_{test}	Pressure drop across the test section of the single channel
PI	Performance index
Pr	Prandtl number
p_b	Perimeter of the agitator blade
P_e	Electrical power consumption
Q	Fictitious force
Q_{sink}	Volumetric flow rate of the virtual active heat sink
q	Heat input
q_{sink}	Heat input of the virtual active heat sink
q_{single}	Heat input of the single channel heat sink
R	Arc beam radius of the oval loop shell structure
Re	Reynolds number
Re_c	Channel Reynolds number
Re_{pta}	The Reynolds number of PTA
Re_{tot}	Total Reynolds number
R_{th}	Thermal resistance
St	Stanton number
S	Pitch of micro pin fins
T_{air}	Ambient air temperature
T_{base}	Base temperature of the single channel heat sink
$T_{fin,in}$	Fin temperature of the single channel heat sink at inlet
$T_{fin,out}$	Fin temperature of the single channel heat sink at outlet
T_{in}	Channel inlet temperature
T_{out}	Channel outlet temperature
T_{sink}	Active heat sink base temperature
T_{sur}	Averaged surface temperature
T_{sub}	Temperature measured below the convection surface
ΔT_{LMTD}	Log Mean Temperature difference
t	Thickness of the arc beam of the oval loop shell structure
U	Strain Energy
V	Shear force
V_{in}	Inlet velocity
V_{out}	Outlet velocity
V_{L1}	Velocity at the section L1
V_{L2}	Velocity at the section L2
V_{con}	Contraction velocity at the outlet adaptor
ν	Kinematic viscosity
w	Channel width
x	Gap distance at the interface between micro pin fin plate and copper block
z	Manometer reading

Greek symbols

ω	Angular frequency
ρ_{air}	Density of air
ρ_{water}	Density of water
ξ	Porosity of micro pin fin arrays
ε	Relative surface roughness
η	Efficiency
δ_h	Horizontal displacement of the oval loop shell
δ_v	Vertical displacement of the oval loop shell
σ_a	Alternative stress applied to the oval loop shell actuator
σ_{max}	Maximum stress applied to the oval loop shell actuator
σ_m	Mean stress applied to the oval loop shell actuator
σ_{min}	Minimum stress applied to the oval loop shell actuator
σ_{pre}	Pre-stress applied to the oval loop shell actuator

Chapter 1: Introduction

1.1 Background and Motivation

Electronics industry has been continuously pushed by the desire for fast processing speed and powerful computational capability, as the amount of data and information that we need to handle is dramatically increasing. Fortunately, highly advanced micro- and nano-fabrication technologies enabled the evolution of the integrated circuit (IC), a vital component of almost all the electronics, by placing numerous tiny transistors on a very small area of substrate. However, advanced integrated circuits generate massive heat that potentially degrades the functionality of electronic devices. By the end of the 1990s, heat removal requirement of integrated circuits was already expected to exceed hundred of watts from a single-chip [1]. Nowadays, the Intel® Core™-i7, one of the fastest processors for personal desktop or laptop computers, requires about 130 W of Thermal Design Power (TDP), which represents the amount of heat that cooling systems need to dissipate, maintaining the chip below its maximum junction temperature [2]. Cooling for military applications becomes even more challenging due to its severe environmental situations such as high ambient temperature, dust, high altitude, etc. [3]. In addition, high-speed processors are being combined with various electronics from cell-phones to the ones for transportations making them progressively smarter and smarter. Therefore, cooling ranks as one of the most critical issues for electronics since the failure of efficient heat removal results in severe damage to the systems. As a result, there has been a strong

need for effective and powerful electronic cooling systems.

A variety of cooling techniques utilizing air, liquid, sprays, jets, boiling heat transfer, microfluidics, etc. have been developed to meet the thermal management requirements of electronics. The liquid cooling, including single-phase liquid loops, single- and two-phase direct sprays or jet impingements, micro channels with two phase boiling, and pool boiling heat transfer, can provide fairly large cooling capability compared to air cooling due to the superior inherent thermo-physical properties of liquid over air. Water has very high specific heat and thermal conductivity, which make it one of the most powerful liquid coolants [4]. Salem et al. [5] investigated two different types of water-cooled heat sink systems and achieved a thermal resistance of 0.174 K/W from a liquid-microchannel heat sink. However, water has some drawbacks such as leakage and corrosion. Non-water based, dielectric liquid coolants have gained attraction, but they are high-cost and have poor thermal characteristics [4]. Many previous works about single-phase liquid cooling in microchannels have been conducted and provided substantial cooling performance enhancement [6-8]. Linan et al. [9, 10] investigated forced convection boiling heat transfer in a microchannel heat sink with water. They provided detailed studies about bubble formation mechanism in a microchannel with different channel sizes, input powers, and flow rates. It is apparent that the addition of microchannel heat sink to liquid could significantly boast cooling performance. However, the microchannel comes with significantly increased pressure drop up to several tens of kPa, which requires excessive pumping power to the liquid loop [11], as well as large temperature gradient along the streamwise direction of the microchannel [12].

Boiling heat transfer stands at the high-end in electronics cooling in terms of its thermal performance. Extensive studies about characteristics of pool boiling heat transfer have been conducted with wide operating conditions [13-19] and the possibilities for electronics cooling were examined [20, 21]. Arik et al. [19] achieved a maximum heat flux of 47 W/cm² on the diamond-based silicon heater with microporous coatings immersed in a dielectric liquid, FC-72. This was about 60 % enhancement over un-treated surfaces. Recently, pool boiling heat transfer with nanoparticles has been widely investigated. You et al. [22] found that a small amount of nanoparticles immersed in water enhanced critical heat flux (CHF), which describes the phenomenon of a sudden decrease of heat transfer. The CHF enhancement was about 200 % compared to the pure water case. However, the effect of nanoparticles on heat transfer coefficients was insignificant. Kwark et al. [23] revealed that a thin nanoparticle film was deposited during nanofluid boiling heat transfer. Experimental studies were performed to examine the causes and results of nano-film depositions on boiling heat transfer.

Another promising high-end technique for electronics cooling is a direct impingement of liquid-jet (orifice) or –spray (nozzle) onto heated surfaces. This scheme provides excellent cooling capability in terms of heat removal per unit flow rate [24]. In addition, the direct impinging to heat sources minimizes contact thermal resistance resulting from interfaces between heat spreaders and heat sources [25]. A considerable amount of works has been accumulated for the past decades to unveil fundamental characteristics of this cooling scheme [26-30]. Oliphant et al. [31] experimentally compared a single-phase liquid jet and spray on a flat heated surface. They reached the

conclusion that the spray cooling could provide similar heat transfer performance with a lower mass flux compared to the jet. Fabbri et al. [32] also performed a similar comparison between single-phase sprays and microjets. However, their result was reversed as the microjets showed better performance with less pumping power per unit heat removed. A 4 x 6 array of microjets generated a heat flux of 300 W/cm² at 80°C. Fabbri and Dhir [25] tested different arrays of microjets using water on a heated flat surface. A maximum heat flux of 310 W/cm² was achieved with jets of 173.6 μm diameter orifices. A two-phase, boiling condition is triggered when the surface temperature of a heated surface rises above the saturation temperature of impinging liquid [31]. The liquid impingement with phase change can greatly take advantages of latent heat during sub-cooled nucleate boiling and direct evaporation from a liquid film formed at a heated surface. Lin and Ponnappan [33] studied closed loop spray cooling with various nozzles and liquid coolants. They achieved a maximum CHF of 500 W/cm² with pure water as a coolant. Visaria and Mudawar [34] examined the effects of different impacting angles of spray on a heated surface both experimentally and theoretically. The conclusions include that changes in inclination angles of spray have small effect on a boiling curve and it eventually decreases CHF. The results also indicated that the impingement normal to the heated surface ensured a maximum CHF. Visaria and Mudawar [35] proposed a design methodology and intensive database of two-phase cone nozzle spray cooling that could be applicable for electronics cooling with different coolants, nozzles, flow rates, and orientations. A new CHF correlation for predicting the performance of spray cooling was recommended. Pautsch and Shedd [24, 36] studied the

thermal performance of single- and multiple- nozzle spray cooling accompanied with a two-phase boiling heat transfer. The highest heat flux was without phase change. They provided visualization studies and empirical models to better understand spray cooling and CHF. Sung and Mudawar [12] explored the combined liquid cooling scheme of single-phase jet impingement and the use of micro channels with HFE 7100 dielectric coolant. A single slot and multiple circular jets were used. The results showed that heat transfer performance of the combined system has strong dependency on the micro channel height. A highest heat flux of 1127 W/cm² was achieved from circular jet impingements into micro channel.

As discussed so far, the liquid cooling schemes have the capability of dealing with very large heat flux from high power electronics. However, liquid cooling has a potential reliability problem regarding leakage, condensation, corrosion, etc. and requires complex components such as a pump, pipe, hose, container, reservoir, nozzle, and orifices. There are also many electronics systems that need to be operated in extreme environmental conditions, and this generates stringent constraints and limitations to the liquid cooling schemes. However, air cooling is very reliable and environmentally favorable. In addition, air is the most abundant and natural cooling medium compared to the artificial dielectric liquid coolants that need special pre- and post-treatments. Therefore, air cooling still remains attractive for many cooling applications of electronics, where the liquid coolings cannot satisfy requirements and constraints of such systems. As a passive approach for air cooling, natural convection on different types of heat sinks was widely investigated experimentally and numerically. Most focused on design optimization of heat sinks with

rectangular fins [37-40], radial fins [41], and circular pin fins [42]. Harahap and Setio [43] proposed several correlations based upon experimental studies on variously-arranged finned arrays. However, the cooling capability of natural convective heat sink is far from the desired performance for modern power electronics due to the intrinsic limitations of natural convection. To enhance performance, a fan or a blower, which can generate strong air flow through finned arrays, was adapted together with optimized heat sinks. This scheme has become the most widely adopted method for electronic cooling. Researchers have recently focused on developing and optimizing different kinds of heat sinks with forced convection [44-46]. In spite of the addition of forced convection with a fan or blower, thermal management through air cooling continues to require more powerful cooling capability as integrated circuit fabrication technologies continue to evolve. As a result, more powerful active cooling components that can enhance, or replace, the fan or blower are presently of interests.

A synthetic jet has been researched and continuously raised as a promising active cooling device for the last decade. A periodically oscillating diaphragm at one side of a cavity generates zero-net mass flow through an orifice forming a train of vortex rings due to the separation at the edges of the orifice. The synthetic jet still has many of characteristics of a continuous jet issuing out of the cavity, since half of the cycle is a jetting-out flow. Hydrodynamic characteristics of continuous jets were studied for cross flow effects [47-50]. In addition, intensive studies on the formation, evolution, and inherent features of the synthetic jet were conducted by [51, 52]. Beratlis and Smith [53] performed a numerical study to optimize a synthetic jet for cooling a vertical cavity

surface of emitting laser array. Their optimization parameters were the angle of the synthetic jet and vertical and horizontal distances from the laser array. Mahalingam et al. [54] fabricated a synthetic jet ejector that generates a secondary flow in a channel and studied the effect of channel width on induced flow characteristics and thermal performance. An active heat sink combined with the synthetic jet ejector was tested for dissipation of 110 W of heat while maintaining a heat sink temperature of around 100 °C. This was a 350 % improvement compared to natural convection. Mahalingam [55] developed a model to predict the thermal performance of the synthetic jet ejector. Wang et al. [56] fabricated a synthetic jet substrate embedded into a printed wiring board that potentially can be used for the thermal management of microelectronics. A flexible polymeric diaphragm was driven by an electromagnetic driver. The synthetic jet achieved a peak jet velocity of 14 m/s with a power consumption of 60 mW. The active cooling achieved a heat flux removal of 3.6 W/cm² maintaining a surface temperature as 70°C. Pavlova and Amitay [57] found that synthetic jets are three times more effective for heat transfer compared to normal continuous jets at the same Reynolds number. They conducted detailed flow visualization studies to understand the cooling mechanisms at different jet formation frequencies of 1200 Hz and 420 Hz. Arik [58] investigated the localized heat transfer performance of a piezoelectric synthetic jet driven at a resonance frequency between 2000 Hz and 6000 Hz. They also studied the effects of different applied voltages, frequencies, and heater lengths on synthetic jet's performance. The synthetic jet obtained 10 times of thermal enhancement over the heater with a length of 6.25 mm compared to natural convection condition. Chaudhari et al. [59, 60] studied heat

transfer characteristics of synthetic jet on a heated flat surface with different orifice: shapes, diameters, plate thicknesses, and aspect ratios, different cavity depths, etc. The results indicated that the square orifice generated the maximum heat transfer coefficient among rectangular, circular, and square shapes. The cavity depth has small effect on heat transfer performance. For the rectangular shaped orifices, a small aspect ratio performed better. At the larger axial distances, thermal performance decreased with increasing aspect ratio. The comparisons between synthetic and continuous jets were provided, and both showed similar cooling performances. The maximum heat transfer coefficient of around 160 W/m² K was achieved from the synthetic jet operating at 250 Hz with an orifice diameter and cavity depth of 14 mm and 6.3mm, respectively.

A piezoelectric fan is one of the newly focused methods for the active air cooling of electronics. A bi- or mono-morph layer of piezoelectric ceramic patches generates flapping motion to the thin elastic shim blade in the center at its resonance yielding air currents from a flapping tip. A variety of piezoelectric fans with different configurations have been reported in the literature since Toda and Osaka [61] raised the possibility as a cooling device. Yoo et al. [62] investigated the vibration characteristics of a bimorph piezoelectric fan with an operating frequency of 60 Hz. The length of the fans ranges from 28.6 mm to 69 mm. Different shim materials were tried and analyzed theoretically. They revealed that the length of the shim blade and the resonant frequency have inverse relationships. The maximum peak to peak displacement of 35.5 mm was achieved from the phosphor bronze-made fan at a voltage of 220 V. The operating frequency was 60 Hz. Açikalin et al.[63] conducted the study of piezoelectric fans for small portable electronics

as the fan has a low noise and low power consumption level. The length of the piezoelectric fan was 63.5 mm; it generated a peak-to-peak amplitude of 15 mm at an operating frequency of 20 Hz. They studied thermal performance of the fan with different overlapping lengths and mounting configurations relative to a heat sink. As a result, half overlapped and horizontally positioned piezoelectric fan provided the largest heat transfer coefficient of around 102 W/m² K. In addition, they have demonstrated the thermal performance of the fan in the laptop environment. Flow visualization was also provided for a more detailed study. The use of higher resonance modes of piezoelectric fans was investigated by Wait et al. [64] with finite element and experimental methods. They concluded that the second mode of fan operation is most desirable in terms of the electromechanical coupling factor, which describes the conversion effectiveness from electrical to mechanical energy of the fan. However, the higher mode operations came with increased power consumption and losses. Açikalin and Garimella [65] predicted fundamental characteristics of the piezoelectric fan such as flow fields around the fans, fan curves, and heat transfer performance utilizing numerical analysis. Kimber et al. [66] confirmed localized heat transfer of a heated flat surface cooled by the piezoelectric flapping fans operating at 60 Hz with an amplitude of between 6.35 mm to 10 mm. The experimental results suggested that the localized heat transfer rate was maximized in the vibration envelop region. The heat transfer coefficients of their fans were less than 100 W/m² K at the highest spot of the vibration envelop. They also found that the optimal gap is closely related to the vibration amplitude of the fan. Liu et al. [12] examined the influences of fan geometry, horizontal/vertical arrangement, and overlap position

between a heat sink and fan, with six different mono-morph piezoelectric fans. The operating frequencies of their fans ranged from 28 Hz to 53 Hz. The thermal enhancement ratios of their fans were up to the order of 3 compared to natural convection cases. Petroski [67] proposed optimized heat sink designs specially adapted to the oscillating piezoelectric fans. The combined system of optimized heat sink and embedded piezoelectric fan achieved a thermal resistance of 1 °C/W. As discussed so far, the piezoelectric fan with the operating frequency of less than 100 Hz has various merits suitable for small electronics such as low noise level, low power consumption, compactness, etc. However, its localized heat transfer performance and relatively poor cooling capability such as heat transfer coefficient of around 100 W/m² K makes the flapping fans not suitable for high power electronics cooling.

The active air cooling devices discussed above are very novel, but the localization and weak cooling performance of around 100 W/m² K seems not enough to postpone the transition to the liquid cooling for high power electronics. It is rather considered to be suitable for small portable or compact moderate speed electronics as a spot cooling device. Thus, the desire for more effective and powerful active air cooling system remains unfilled.

1.2 Objective of the Work

The objective of current study is to develop and demonstrate the powerful active heat sink system that can push the limit of air cooling scheme to the extreme for high power electronics. The active component of the system denotes a translational flow agitator that can be embedded between the heat sink fins and boost convective heat

transfer of heated surfaces coupled with an external blower or fan. In addition to this active component, micro pin-fin surfaces are introduced onto the heat sink surfaces that allow a dramatic increase of heat transfer area. Figure 1.1 shows a schematic of the active heat sink with agitator blades operating between channel walls. Heat from a chip dissipates through a heat spreader and thermal interfaces to a heat sink, and is carried away by a fan. In a traditional heat sink channel, the flow induced by fan is not strong enough to disturb stabilized laminar thermal boundary layers on the fin surfaces. On the other hand, in the active heat sink system, the blade oscillates with a high frequency and a large translational displacement. It directly disturbs the thermal boundary layers on the fin walls using strong favorable and adverse pressure gradients. A micro pin fin array is another feature of the active heat sink that is a passive way of enhancing heat transfer by adding more heat transfer area as well as disturbing thermal boundary layers.

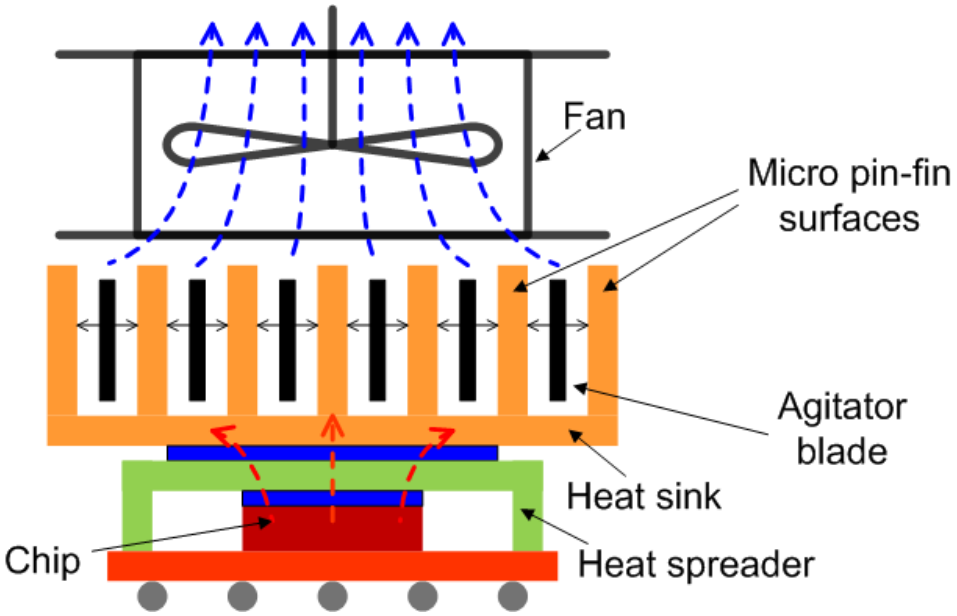

Figure 1.1: Conceptual illustration of active heat sink with agitator blades embedded between heat sink channel walls and schematic of staggered arrays of micro pin fins on the active heat sink channel walls.

In this study, detailed discussion about the driving mechanism of the translational agitator is presented. This includes vibrational and structural analyses of the agitator that are performed through analytical and experimental methods. In addition, thermal performance of the agitator demonstrated in single channel heat transfer experiments is provided. Of particular interest is to figure out thermal characteristics of the agitation effects over the micro pin-fin surfaces and to compare them to cases with plain surfaces. Therefore, intensive experimental studies of micro pin-fin surfaces were performed in a single channel with and without agitation effects and their thermal and hydrodynamic characteristics are discussed. Finally, the full size active heat sink system with various agitators over the micro pin-fin surface is developed and its thermal and hydrodynamic performances are evaluated.

1.3 Methodology

A translational agitator moves a thin and rigid plate back and forth between the heat sink fins and creates very strong air currents around the fin base and side surfaces. Various complex air flow motions are expected as the agitator moves. The air in the contracting area (left side of the agitator blade in the channel of Figure. 1.2) is squeezed out to the opposite section (right side of the agitator blade in the channel) through the narrow gap between the agitator tip and fin base creating a high velocity air jet, which is strong enough to thin the thermal boundary layer of the fin base surface. A similar air flow from the fin base to the tip along the side surface is also expected. In the expanding area, turbulent vortices, which are similar to wing tip vortices of airplanes, could take place and develop along the edges of the agitator plate as the agitator actively oscillates.

These multiple motions of air flow elevate the convective heat transfer rate synthetically and help air to remove more heat from the heat sink. At the end, the channel flow generated by an external blower carries out heated air and provides fresh air.

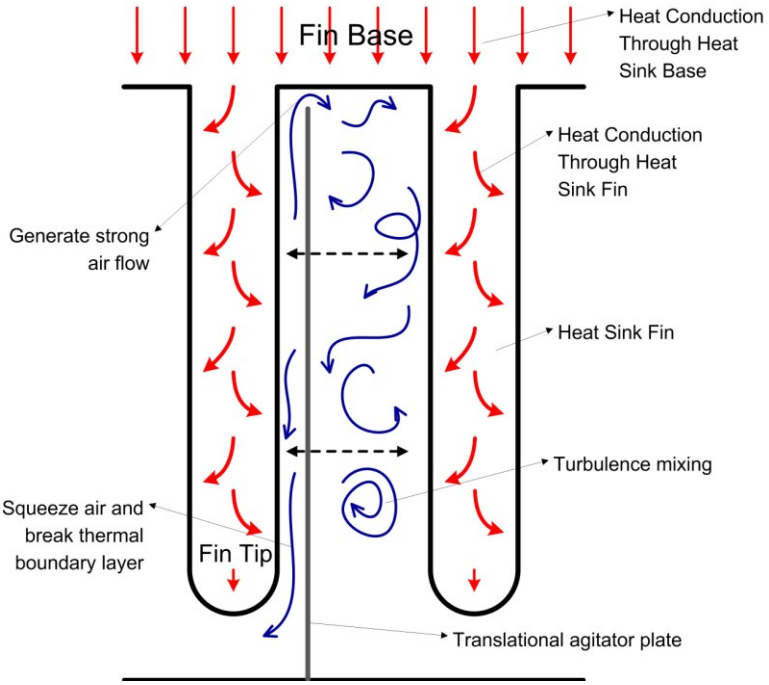

Figure 1.2: Illustration of translational agitator blade in a heat sink channel

Piezoelectricity is the ability of some materials such as crystals and ceramics that create the electrical field when mechanical strain is applied to the materials. Conversely, reverse-piezoelectric materials undergo the physical deformation in response to the applied electrical field. Reverse-piezoelectricity is utilized to realize the concept of the flow agitators. There are some piezoelectric crystals are found in nature and some polycrystalline ceramics are artificially fabricated by advanced engineering techniques. Normally, the ceramics, such as Barium titanate ($BaTiO_3$) and Lead zirconate titanate (PZT), have larger piezoelectric effect than natural piezo-materials, such as Quartz and Tourmaline, showing large piezoelectric constants (D).

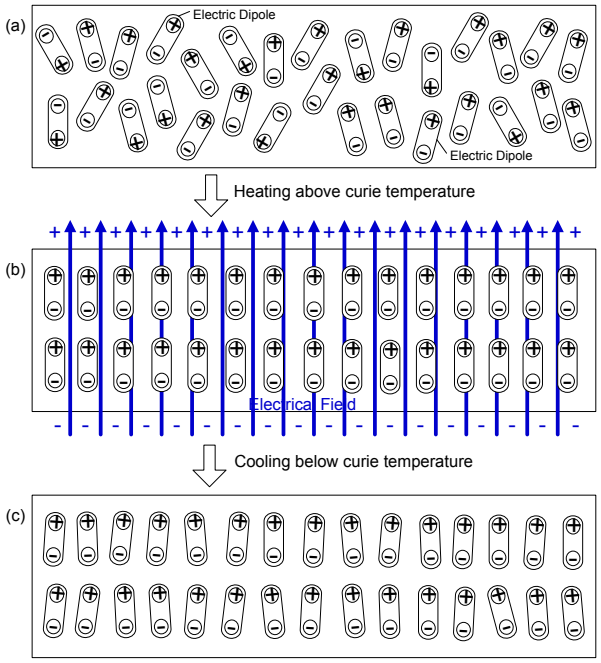

Figure 1.3: Polarization process of piezo ceramic materials; (a) Randomly distributed dipoles before poling process; (b) Well aligned dipoles during poling process; (c) Partially aligned dipoles after poling process.

Contrary to the natural piezoelectric materials, the piezoelectric ceramics need a polarization process for the piezoelectric phenomenon to occur. Dipoles inside the ceramic materials are distributed with random orientations before the polarization process. After heated above a curie temperature of the material, these randomly oriented dipoles could be well-aligned in one direction by applying very strong electrical field of several kV/mm. Followed by a cooling step below the curie temperature with the electrical field removed, the ceramic remains with the partially aligned dipoles and exhibit piezoelectricity when the ceramic is subjected to an external electric field. The polarization process is illustrated in Figure 1.3.

Generally, the direction of the electrical field applied during the poling process indicates polarization directions of the piezoelectric ceramic materials. Physical

deformation rate of the piezoelectric ceramics along this direction is the largest and is defined by piezoelectric constant D. In Figure 1.4(a), the arrow pointing from the bottom to the top represents the poling direction, which is the same direction with the electric field during the poling process. Each side of cylinder is coated with electrodes and they are connected to the electrical source. The piezoelectric cylinder contracts when the same direction of electric field with the poling direction is applied to the cylinder (Figure 1.4(b)). Reversely, the expansion takes place when the opposite electric field is applied to the cylinder (Figure 1.4(c)). The mechanical strain of the piezoelectric cylinder under the contraction or expansion could be expressed as:

$$S = D_{ij}E \tag{1.1}$$

Where S, D_{ij}, and E are the mechanical strain, piezoelectric constant, and applied electrical field, respectively. The subscript i indicates the direction of the electrical field and j indicates the direction of strain occurred. Along the longitudinal direction of 3, the above equation could be switched to the below equation with the substitutions of $S = \Delta L / L$ and $E = V / L$:

$$\Delta L = D_{33}V \tag{1. 2}$$

along the radial direction, the equation could be specified similarly as:

$$\Delta R = D_{31}V \tag{1. 3}$$

Accordingly, the piezoelectric constant along the electrical field direction is a very important parameter to characterize the piezoelectricity of the material. In many engineering applications including, piezo-actuators, -motors, and –sensors, large piezoelectricity is required in order to acquire high dynamic performance of devices.

Thus, the piezoelectric ceramic fabrication technology has been advanced continuously and produced piezo ceramics that have high piezoelectric constants and many other superior properties compared to natural piezoelectric materials. Among the piezoelectric ceramics, the lead zirconate titanate (PZT) is one of the most popular piezoelectric ceramics. It is used widely in many applications.

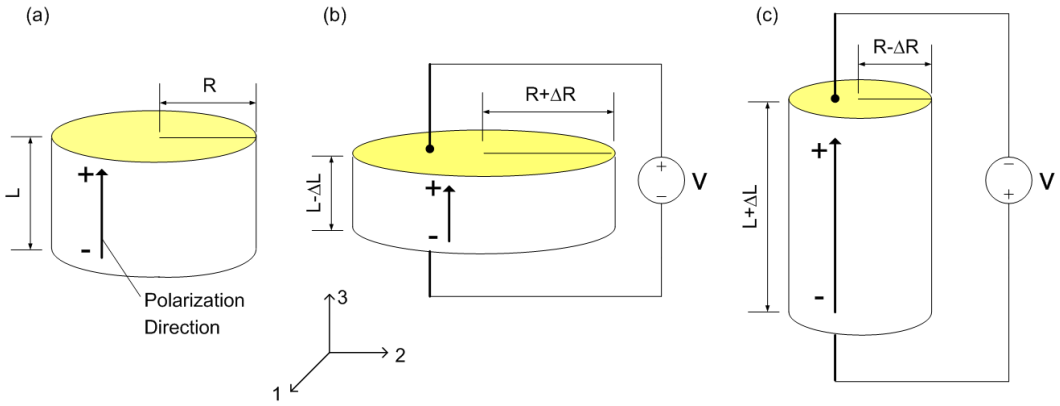

Figure 1.4: Physical deformation of piezoelectric material under applied external electrical field; (a) Polarized piezoelectric cylinder; (b) Contraction with applied voltage; (c) Expansion with reversely applied voltage.

In order for the agitators to have a full stroke in the heat sink channel and break down the thermal boundary layer on the heat sink walls, the dynamic parts of the agitators should oscillate vigorously with a large amplitude and high frequency. Therefore, the PZT ceramics are selected as appropriate piezoelectric material for they have fairly large piezoelectric constant and permittivity. The detailed driving mechanism of the translational agitator utilizing the piezoelectric actuator will be discussed in the following sections.

Chapter 2:
Piezoelectric Translational Agitator

2.1. Introduction

Piezoelectric materials have been utilized in various applications such as micro/nano positioning devices, motors, sensors, actuators, etc. An attractive feature is its high energy density. The optimum actuator should be able to satisfy the criterion of high displacement, large force, broad range of operating frequency, and low electrical power consumption [68]. Even though many piezoelectric actuators have been developed in the past, it is difficult to find examples that achieved all the parameters of large mechanical stroke and force and high operating frequency that are required to realize the concept of a piezoelectric translational agitator. Piezoelectric bending actuators with either unimorph or bimorph piezoelectric ceramics attached to high elastic shim materials can generate flapping motions with sufficiently large displacements [69-72]. However, their blocking force is very small compare to other actuation techniques. Piezoelectric multi-layered stack actuators can provide a very large blocking force with an operating frequency extended to tens of kHz. Unfortunately, only an exceptionally small displacement of a few microns is obtained. Studies have been intensively performed to overcome the shortcoming of the stack actuator. A hydraulic displacement amplification can afford a long augmented stroke and force but with moderately low operating frequencies of below a few hundred Hz [73-76]. The complexity of the mechanical components such as pumps, moving pistons, valves, etc. and reliability problems regarding leakage of liquid restrict

the piezo hydraulic actuators to a narrow area of applications. Relatively large power consumption to achieve high dynamic actuation is another issue of the piezo hydraulic actuators. Many lever mechanisms such as moon- or cymbal-types were developed for displacement amplification [68]. Ham *et al.* [77] developed a piezoelectric pump using a hinge-lever amplification mechanism in order to magnify displacements of piezo stacks. They amplified the displacement up to 683 μm from 28 μm, the original displacement of the piezo stack, with an applied voltage of 100 V. The pump showed maximum capability at an operating frequency of 250 Hz. Joshi and Priya [78] proposed and fabricated an actuator design called the "piezo-bow" which consists of flexural metal caps attached to the piezo stack actuator through metal bars. The "piezo-bow" actuator exhibited about 20 times the amplification ratio, showed a high blocking force, and achieved high frequencies of about 2 kHz. Their amplified displacement was less than one mm. Ma *et al*. [79] proposed a bridge-type flexure hinge for displacement amplification. Numerical and theoretical studies were performed to analyze the ideal displacement amplification ratio of the bridge-type flexure hinge. Furukawa *et al*. [80] developed a flexure-hinged translation mechanism with a push and pull driving system using two piezo stacks suitable for mechanical scanning stages with very high precision. The scanning range of 60 μm and a natural frequency of 1175 Hz were demonstrated with the given amplification system. Juuti *et al*. [81] proposed another bridge-type flexure hinge mechanism to amplify the displacement of the pre-stressed piezo disk actuator. In order to avoid fractures of levers, they applied a laminated two-layered structure cut by a laser. Their maximum amplified displacement was about 1.2 mm from 50 μm piezo

displacement at an applied voltage of 500 V. However, their actuator is not suitable for high frequency application. Mulling *et al*. [82] studied load capabilities of a thin-layered unimorph actuator which is commercially available under the name THUNDER^{TM}. They revealed that end conditions and load capability have a significant effect on the performance of the actuator, interdependently. Kim *et al*. [83] developed a small-scale, three-dimensional, bridge-type flexure hinge mechanism with a maximum operating frequency and displacement of up to several kHz and a few hundred microns, respectively. Lam *et al*. [84] fabricated a cymbal type actuator with a lead-free piezo-ceramic disk. The actuator achieved very high fundamental resonance frequencies, above 80 kHz, with relatively low amplified displacements. Muraoka and Sanada [85] developed a honeycomb-like, successively-connected, lever-hinge mechanism to amplify the displacement of piezo stack actuators. Neal and Asada [86] proposed a piezoelectric actuator that can provide one hundred times amplification using the buckling phenomenon of a flexure-based structure. Ueda et al. [87] developed a new strain amplification design with a nested-rhombus, multilayer system. The multi-layered actuator can generate 21% effective strain from the 12 mm actuator height which is 2.53 mm. However, this mechanism is not appropriate for high-frequency application.

2.2 Objective of the Chapter

In this chapter, we propose piezoelectric actuators with a high frequency of above 1 kHz and a large displacement in the mm range, with low power consumption of less than 10 W, based on an oval-shape loop shell structure. The proposed actuators are utilized as driving mechanisms for translational agitators. The purpose of this section is to address

effective ways of amplifying the very small displacement of piezo stack actuators in highly dynamic actuation modes for realizing a piezoelectric translational agitator. CEDRAT Technologies has developed and commercialized a similar type of actuator using a loop shell structure with the name of APA (Amplified Piezoelectric Actuator) [88]. The APAs can gain an amplified stroke from several tens of microns to about 1 mm. However, their operating frequency is less than 500 Hz when the actuator generates the largest amplified stroke. When the actuators are operating at higher frequencies, above a kHz, the amplified stroke is limited to tens of microns. The proposed actuators used in the present work can utilize the second resonance mode as well as the first mode to maximize the operating frequencies and amplified strokes at the same time. In the following sections, six different oval loop shell piezo actuators which exhibited amplification ratios of several hundreds at the first and second resonant modes with a moderate range of applied voltages, between 20 V and 100 V, are fabricated and their characteristics are analyzed. In addition, detailed vibrational and structural analyses are performed including estimating operating frequencies and fatigue limits of the actuators. At the end, the piezoelectric translational agitators coupled with the oval loop shell piezo actuators and carbon fiber composite blade structures are introduced.

2.3 Oval Loop Shell Piezo Actuator (OLSPA)

2.3.1 Design and Fabrication

A piezoelectric actuator with an oval loop shell amplifier is shown in Figure 2.1. The oval loop shell (Figure 2.1(a)) plays a role of amplifying a displacement from a piezo stack actuator. In order to connect the piezo stack actuator to the oval loop shell, two

inner connectors are attached at the each inner side of the shell with epoxy (Figure 2.1(b)). For an earlier design of the piezo actuator, two inner connectors and the outer shell were cut as one piece. However, due to the characteristics of high duty cycles of the actuator, a fatigue failure occurred within 900,000 cycles at the joint where a large area expansion exists. As a result, the design was changed slightly. The inner connection parts were separated to give large curvature, minimizing stress concentration through the outer shell. The earlier design of the actuator and the fatigue failure point are shown in Figure 2.1(d).

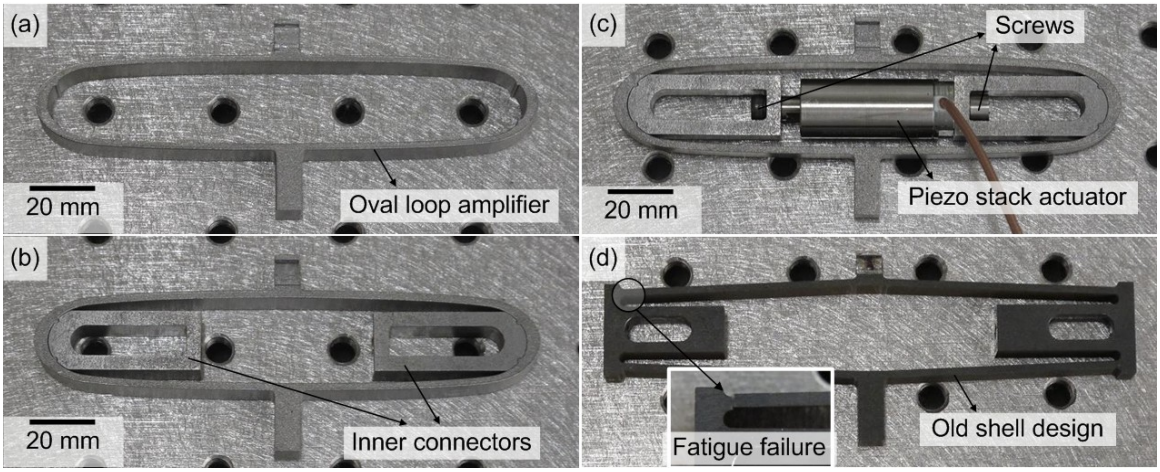

Figure 2.1: (a) Oval loop amplifier, (b) Oval loop amplifier attached with two inner connectors, (c) Oval loop amplifier coupled with piezo stack actuator, (d) Old shell design cut as one piece including inner connector parts. Inset shows the fatigue failure point where the spatial expansion occurs.

In the oval loop shell, the piezo stack actuator should be aligned exactly on the symmetry line dividing the oval loop upper and lower regions. Therefore, screws were used to fix the stack actuator at the correct position between two inner connectors. The piezo stack actuator is pre-stressed by shortening the distance between two inner pieces to less than the length of the stack actuator. Without sufficient pre-stress distance, the actuator could not generate good performance as the actuation energy from the piezo

stack actuator would not be fully transmitted to the oval loop shell structure. The pre-stress distance is around 100 μm. The oval loop shell and the inner pieces were fabricated by wire EDM (Electrical Discharge Machining) using 5160 spring steel. Such steel has been extensively used for spring applications, such as a leaf spring.

In order to achieve a high frequency of above 1 kHz and a large displacement of above the one mm range in an actuator with low power consumption, it was desirable to use the structure's resonance modes. A schematic and the design parameters of the oval loop shell are presented in Figure 2.2(a). The piezo stack actuator generates a translational displacement in the horizontal direction (horizontal arrows in Figure 2.2(b)), and the oval loop shell amplifies the movement in the vertical direction (vertical arrow in Figure 2.2(b)). The shell forms an oval-shaped closed loop with a uniform beam thickness (t) between points x and y. To control and restrict bending motion within the section between x and y, the beam thickness was increased starting from y until it reaches y'. Next, it was decreased to the original thickness (t) from y' to y." In designing the oval loop shell, there are three parameters primarily to be considered to produce an amplified displacement and a high resonance frequency. They are next discussed. A right triangle could be drawn in between vertexes formed in the center and each end of the main beams (dashed lines in Figure 2.2(b)). Two leg, "a" and "b" of the right triangle, are key design parameters as well as the beam thickness "t", an important parameter to affect the resonance frequency of the actuator.

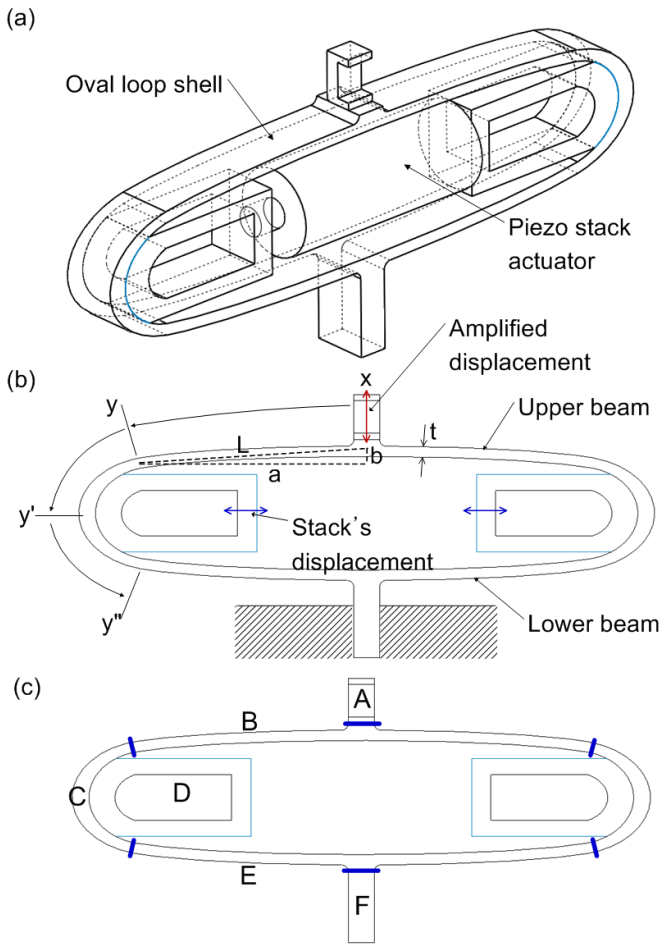

Figure 2.2: (a) 3D view of the piezo actuator, (b) Side view of oval loop shell and design parameters, (c) Various sections of the oval loop shell structure

One of the main design considerations is a size factor. Therefore, "a" is selected to not exceed 50 mm so that the entire length of the actuator could be within 100 mm. As noted previously, the fatigue failure should be overcome because desired actuators have a characteristic of heavy duty cycles due to the high frequency and large displacement. Hence, in addition to the design modification, shot peening was applied onto the surface of the oval loop shells to induce compressive residual stresses in the shell structure. Literature shows that shot peening could enhance fatigue strength significantly. Grinspan and Gnanamoorthy [89] applied an oil jet peening process onto the surface of a carbon

steel cantilever-type specimen. The peening process improved the fatigue strength about 19% compared to unpeened specimens. Aggarwall *et al*. [90] investigated the effect of the shot peening process for minimizing fretting fatigue failure of the spring steel leaf spring. Other researchers employed shot peening to enhance fatigue strength of systems ([91, 92]). A shot-peened shell surface is shown in Figure 2.3, compared with a normally machined 5160 spring steel surface. A specific test to measure lifetime was not performed. However, the modified and shot peened oval loop actuators were shown to withstand at least 18,000,000 cycles without a fatigue failure.

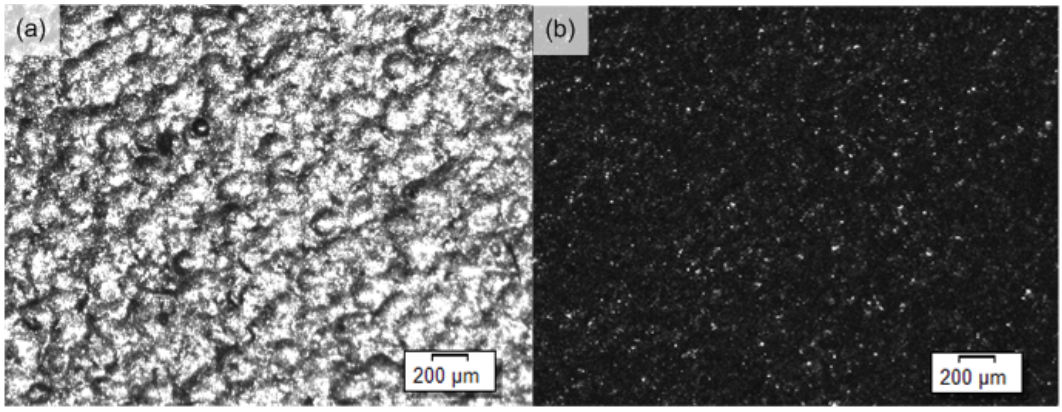

Figure 2.3: (a) Shot peened shell surface, (b) Bare surface of 5160 spring steel after the wire EDM process

Totally, six different oval loop shells were fabricated with different values of "a," "b," and "t" in Figure 2.2(b). The different design parameters of the oval loop shells are listed in Table 2.1. Shell 1 and 2 have the same "a" and "b" but different beam thicknesses of 1.4 mm and 1.6 mm. Shell 3 and 4 are longer than shells 1 and 2. Thus, among these four actuators we can examine effects of shell length and thickness on vibration characteristics at higher resonance modes of the structure.

Table 2.1: Six different oval loop shell designs for vibrational study

Oval loop shells	a (mm)	b (mm)	t (mm)
Shell 1	35	1.8	1.4
Shell 2	35	1.8	1.6
Shell 3	40	1.8	1.4
Shell 4	40	1.8	1.6
Shell 5	35	1.7	1.6
Shell 6	35	1.7	1.7

Shells 5 and 6 are selected mainly to see the effects of "b." For this particular section, the PSt HD 200 piezo stack actuator from APC International, Ltd. was used for all the oval loop shells. Figure 2.4 shows displacements of the stack actuator with different voltages and frequencies. The piezo stack actuator can generate fairly consistent displacements with a voltage below 100 VAC within the 2 kHz frequency range. However, with applied voltages above 100 VAC, the displacement decreases as the frequency exceeds 1 kHz. This is mainly due to insufficient current supply of the piezo amplifier used at higher frequencies and voltages for current study. Therefore, a voltage below 100 VAC is regarded as a proper operating voltage for a given stack actuator in the current application. However, the range of an applied voltage to piezo actuators can be varying according to different types of actuators.

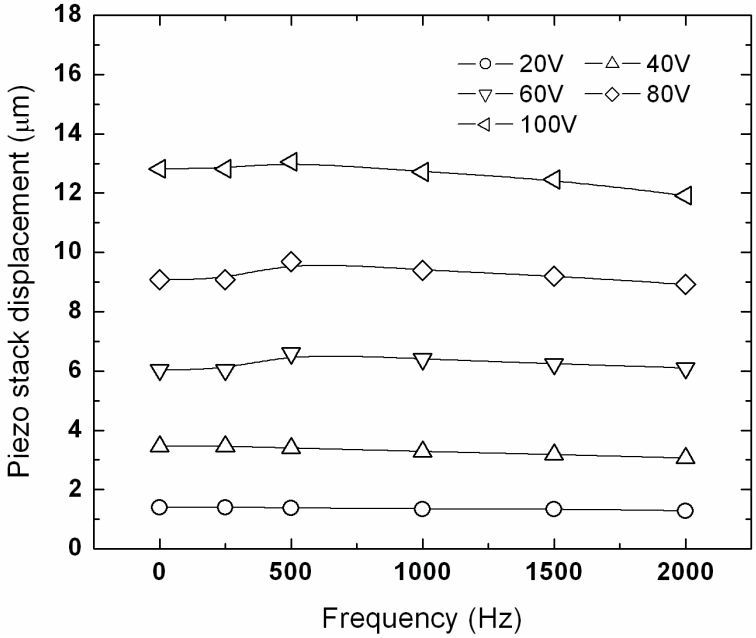

Figure 2.4: Displacement of PSt HD 200 piezo stack actuator with different voltage and frequency

2.3.2 Results of Vibrational Experiments

Vibration characteristics of six fabricated shells were investigated with the PSV-400 laser Doppler vibrometer from Polytec. The VF-500 linear piezoelectric amplifier (Dynamic Structures and Materials, LLC) was used to supply a high voltage to the piezo stack actuator. AC (alternative current) signals were generated by the AFG3102 function generator from Tektronix, Inc. The experimental set up to investigate vibration characteristic using a laser vibrometer is illustrated in Figure 2.5. The piezoelectric oval loop shell actuator is vertically placed on an optical table clamped with a mechanical vice and a laser from the vibrometer head shoots on the upper surface of a rectangular bump in the center of the shell.

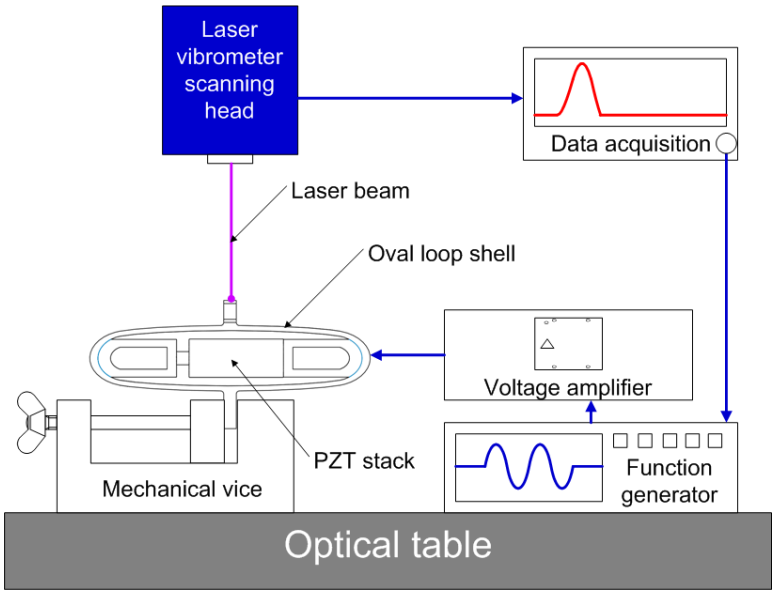

Figure 2.5: Schematic of experimental facilities for measuring vibration characteristics of the actuators

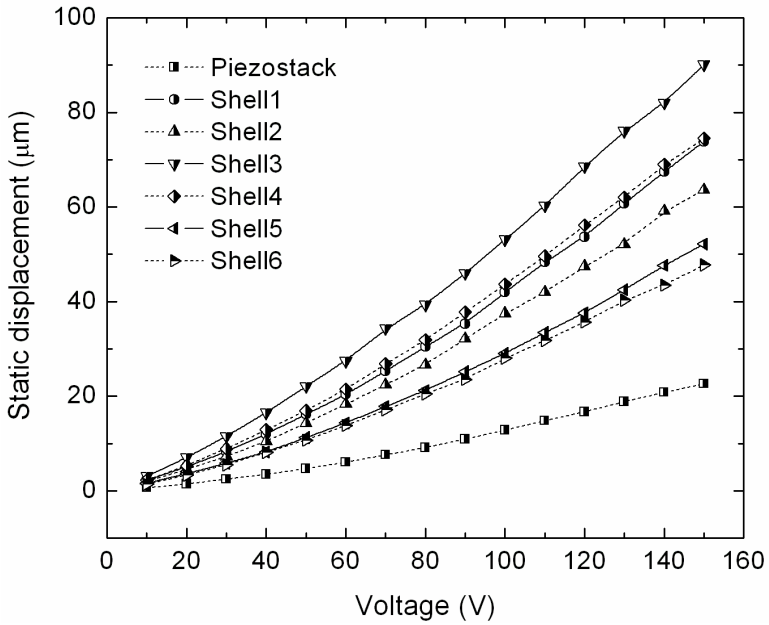

Figure 2.6: Static deformation displacements of the shells compared with the displacements of the piezo stack actuator

Figure 2.6 shows the displacements under a static deformation of the oval loop shells. It is apparent that the longer shells (shell 3 and shell 4) create larger displacements than the shorter shells (shell 1 and shell 2). Shell 3, with a thicker beam, has a larger static displacement than shell 4. The same pattern is seen between shells 1 and 2, which have only a thickness variation. Shell 5, with a decreased "b" of 1.7 mm, produces a smaller static displacement, compared to shell 2. Shell 6 shows the minimum amplified static displacement among the six oval loop shell actuators because it is the smallest in size and the largest in beam thickness.

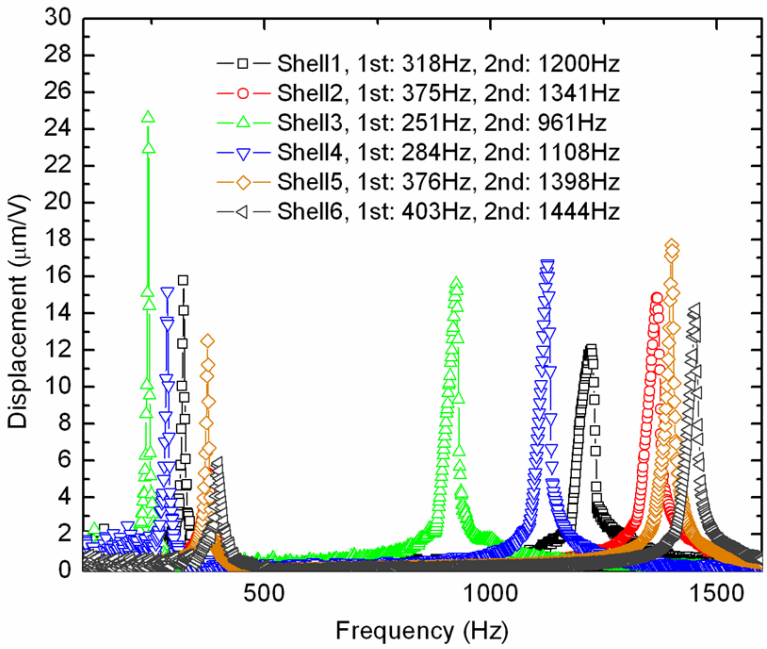

Figure 2.7: Displacement response spectrum of six oval loop shells in the frequency domain from static to 2 kHz

Figure 2.7 presents displacement responses of six oval loop shells in the frequency domain. The response was scanned within a 2 kHz range since two appropriate resonance modes for translational displacement occur inside this frequency range. For all of the shells, two different resonance modes are shown in Figure 2.7. The first mode of

resonance frequencies is below 500 Hz. At the first mode, the lower beams in Fig. 2(b) oscillate, driving the entire shell structure, including the piezo stack actuator, in the vertical direction. In this mode, it is not easy to support the whole body of the vibrating actuator, including the stack. At the second resonance mode, vibrational energy concentrates on the upper beams (Figure 2.2(b)), and only the upper beams flap vigorously creating their translational displacement while the remainder of the actuator body remains stationary. From these results, we see that the resonance frequency rises as the thickness of the beams increases. Thus, shells 2 and 4 have larger resonance frequencies of the first and second modes than shells 1 and 3. Apparently, the resonance frequencies of the shorter loops (shells 1 and 2) are larger than the longer ones (shells 3 and 4). Shell 6 generates the highest resonance frequencies since the shell stiffness is largest, due to the shortest length and the thicker beam 1.7 mm.

Amplified displacements at the first mode of resonance of the shells are presented in Figure 2.8 with different applied voltages between 0 and 100 VAC. For all the cases, the amplified displacements almost linearly increase with increasing voltages. Shell 3 shows the maximum amplified displacement of more than 1.6 mm at an applied voltage of 100 VAC. Surprisingly, shell 5 generated the second largest displacement at 100 VAC. It is shown that the pattern of the displacement amplification at the first resonance mode does not match the static amplification cases.

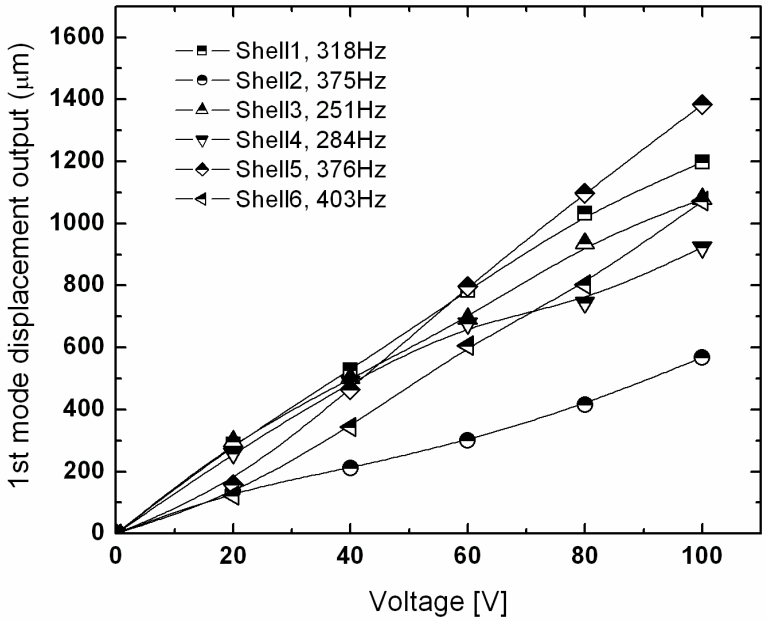

Figure 2.8: Amplified displacements of six oval loop shells at the first mode of resonance

Figure 2.9 represents the amplified displacements at the second mode of resonance. Again, shell 3 produced the largest displacement of more than 2 mm at a resonance frequency of 961 Hz. However, the resonance frequency is the smallest among the six oval loop shell actuators, due to its size being larger than the other shells' sizes. Shell 4 shows the second largest displacement at a resonance frequency of 1,108 Hz. Shell 6 achieved the highest resonance frequency of 1,444 Hz with an amplified displacement of about 1.5 mm at an applied voltage of 100 VAC. All fabricated shells generated amplified displacements of more than 1 mm at the higher frequencies (above 1 kHz) except for shell 3, with a resonance frequency of 961 Hz. The performance of the oval loop shell piezo actuator is compared with other types of amplification mechanisms

in the literature, in terms of the operating frequency and amplified displacement, in Table 2.2.

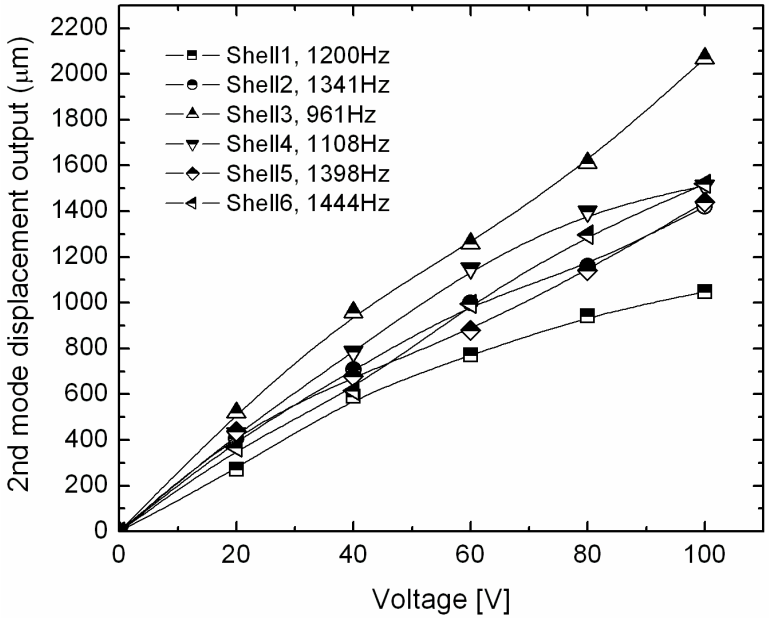

Figure 2.9: Amplified displacements of six oval loop shells at the second mode of resonance

Table 2.2: Performance comparison of the actuators in the literature

	Amplification type	**Frequency**	**Amplified displacement**
Present work (shell 6)	Flexural beam	1444 Hz	1519 μm
Yoon and Washington [75]	Hydraulic	80 Hz	3180 μm
Ham et al. [77]	Hinge-lever	250 Hz	683 μm
Joshi and Priya [78]	Flexural cap	2000 Hz	15 μm
Furukama et al. [80]	Flexure-hinge	1175 Hz	60 μm
Juuti et al. [81]	Bridge	Static condition	1200 μm
Mulling et al. [82]	THUNDER™	Static condition	410 μm
Kim et al. [83]	Bridge	5700 Hz	294 μm
Lam et al. [84]	Cymbal-type	9420 Hz	~ 1 μm
Muraoka and Sanada [85]	Honeycomb link	355 Hz	410 μm
Cedrat Technologies [88]	APA 1000XL	210 Hz	1050 μm
	APA 100MML	1730 Hz	100 μm

Figure 2.10 shows amplification ratios of the shells, both at the static and resonance conditions, with comparison with the static case amplification ratio. At the static conditions (Figure 2.10(a)), shell 3 can amplify the displacement up to 10 times at a

lower voltage of 20 VAC. As the voltage increases, the amplification ratio decreases. This happens to all the cases and all six shells in the static and resonance conditions. At the first mode (Figure 2.10(b)), shell 3 amplifies the displacement 213 times compared to the piezo stack actuator displacement at a voltage of 20 V. When 100 VAC is applied, the amplification ratio of shell 3 is 84. At the second mode (Figure 2.10(c)), the amplification ratios improve over those of the first mode cases. At the applied voltage of 20VAC, shell 3 magnifies the displacement 372 times from the displacement of the stack actuator. In addition, an amplification of 161 was achieved with an applied voltage of 100 VAC for shell 3. Shell 6, operating at the highest frequency of 1,444Hz, gives an amplification of 118 at 100 VAC.

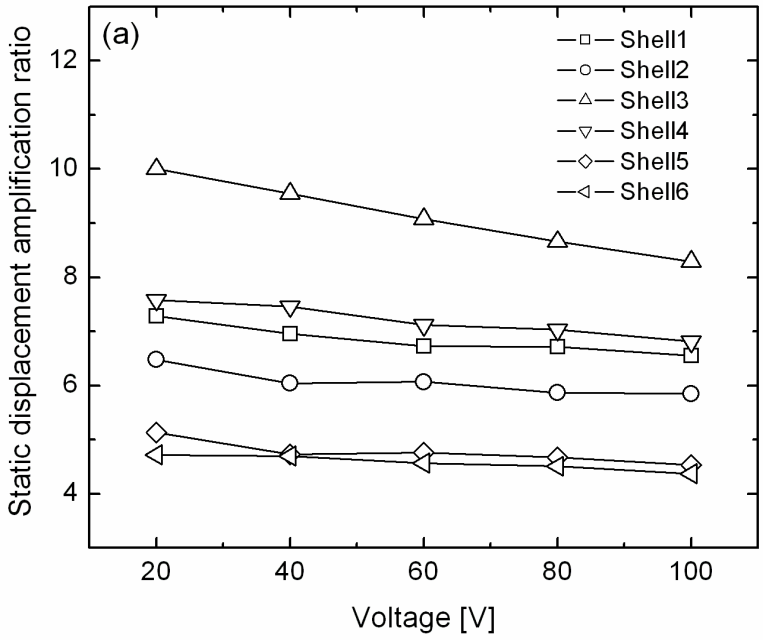

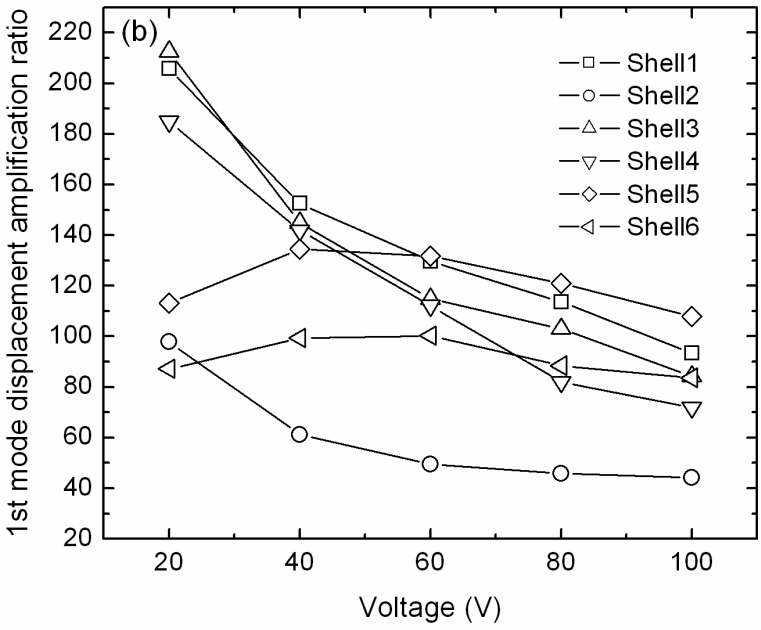

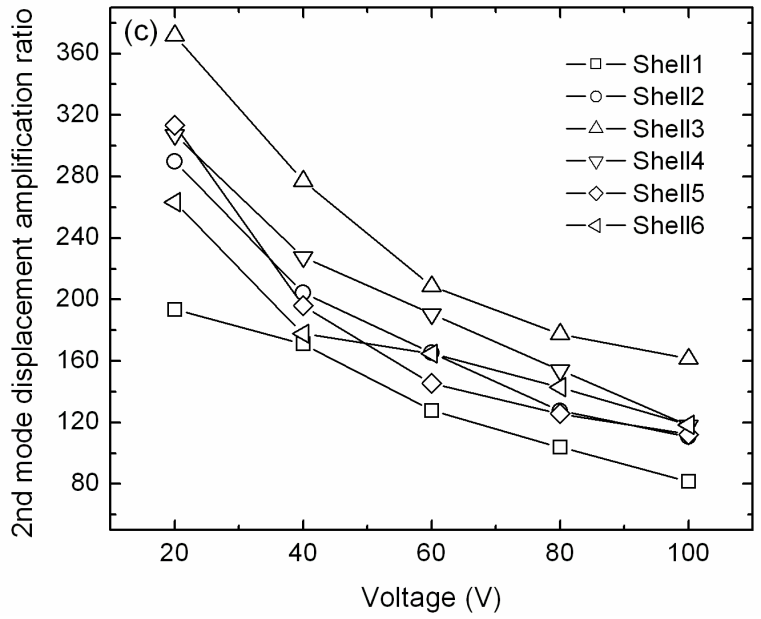

Figure 2.10: Comparisons of amplification ratio, (a) static condition, (b) the first mode, (c) the second mode

2.3.3 Load Capability and Efficiency of OLSPA

An experimental investigation was performed about load capacity and efficiency of the actuator. Shell 3, with the PZT stack actuator P.010.40P from Physik Instrumente (PI) was utilized for the experiments. Load was gradually added by stacking carbon fiber plates on top of the actuator, and dynamic displacements and resonance frequencies at every step were measured with the laser vibrometer. Added mass starts from 3.1 g, which includes the supporting frame and one carbon fiber plate. From the results, it is confirmed that resonance frequency and dynamic displacement reduce as more load is applied to the actuator (Figure 2.11). When around 49 g of mass was loaded to the actuator, the dynamic displacement decayed to around 20 μm. With more load, dynamic displacement became so weak that it is hard to distinguish it from the background noise. Therefore, this load point can be regarded as the maximum dynamic load to shell 3 at the applied voltage of 140 VAC. When the load addition is small, the decreasing rate of resonance frequency with added load is large and becomes smaller as more load is added to the actuator.

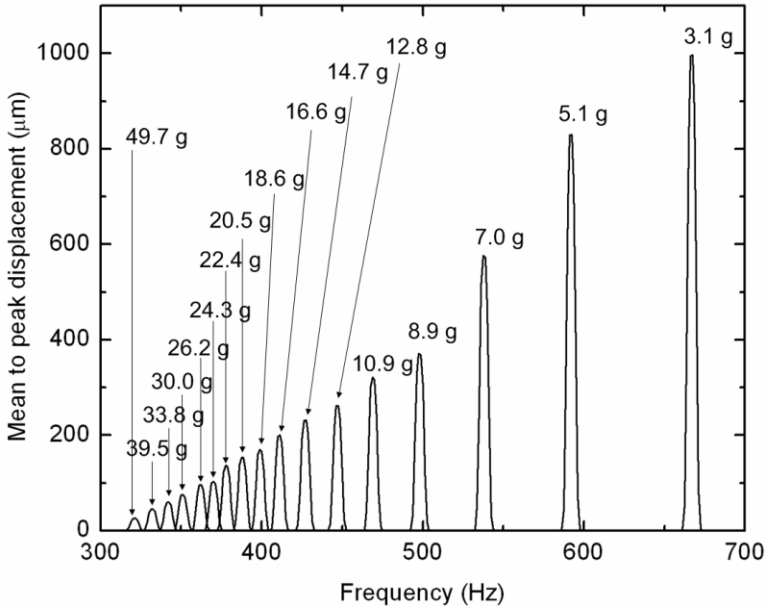

Figure 2.11: Dynamic displacement and resonance frequency shift with different applied loads to shell 3

Electrical power consumption of the actuator was also measured at every step of load addition (Figure 2.12).

$$P_e = \frac{1}{T}\int_0^T V(t)\cdot I(t)dt \qquad (2.1)$$

where T is the period over which data were measured. The varying voltage and current, V(t) and I(t), are measured by a digital oscilloscope between the output of the piezoelectric amplifier and the input to the piezo stack actuator. The current to the piezo stack actuator was measured by placing a resistor of 10 Ω between the ground and the piezo stack actuator. The oscilloscope reads the voltage drop between the two junctions and the current to the stack actuator can be calculated by dividing the voltage drop with the resistance. Electrical power consumption is converging to a linear relation at the high load of around 50 g where very small dynamic displacements are generated. At these very low dynamic condition points, where the peak-to-peak displacements are less than

200 μm, it is assumed that almost all the electrical power input to the actuator is consumed as heat loss at the PZT stack. Furthermore, it is fortunate to know that heat loss of a piezo-actuator has a linear relation with an operating frequency [93]. Therefore, it is reasonable to estimate the heat loss at high dynamic conditions, based on this linear relation from the lower dynamic condition points.

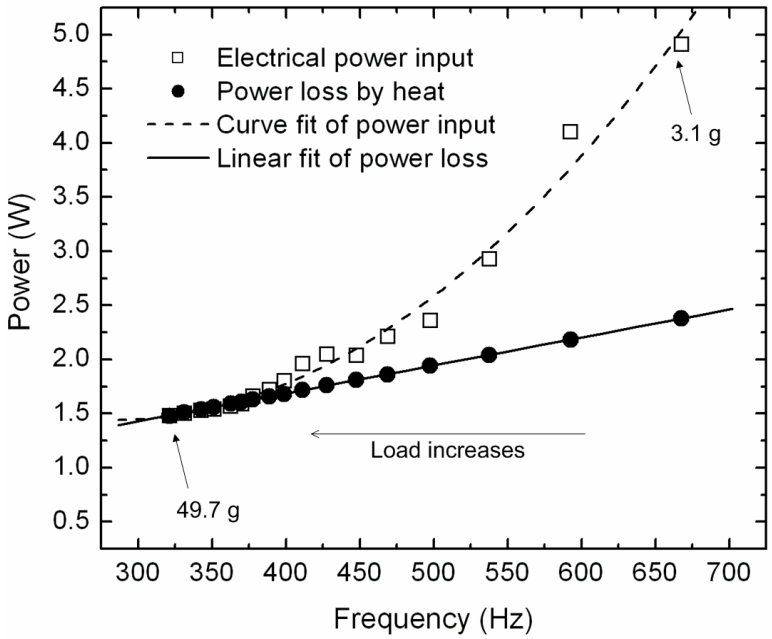

Figure 2.12: Electrical power input and power loss by heat dissipation of the actuator with different applied loads and resonant frequencies

The extrapolation of the heat loss from the low dynamic points to the high dynamic points is shown in Figure 2.12. As a result, the efficiency of the actuator could be defined as:

$$\eta(\%) = \frac{P_{input} - P_{loss}}{P_{input}} \times 100 \tag{2.2}$$

where P_{input} and P_{loss} are the electrical power input to the actuator and power loss by heat dissipation through the PZT stack actuator. The numerator indicates the power consumed

by the mechanical part of the oval loop actuator system. The calculated efficiencies of the actuator from the fit curves of electrical power input and heat loss are shown in Figure 2.13. When 3.1 g of load is applied to the actuator, the efficiency is around 55 %. The efficiency decreases to almost zero when 49.7 g of load is applied. Thus, the actuator generates almost no dynamic performance and all the electric power input at this condition is dissipated through heat loss of the PZT stack actuator.

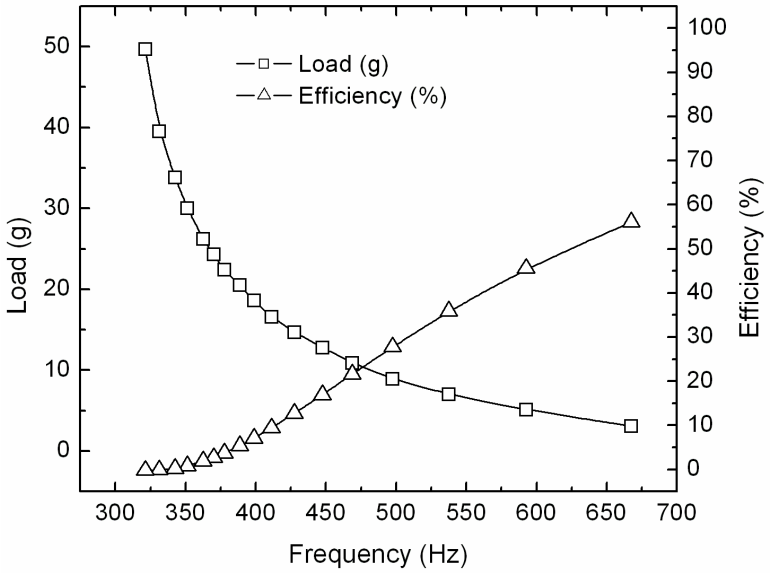

Figure 2.13: Efficiency of shell 3 at different applied loads

2.4 Operating Frequency Estimation of OLSPA

In this section, predicting natural frequencies of the oval loop shell structure was attempted as the first step for theoretically evaluating dynamic characteristics of the actuator. A spring constant of the oval loop shell structure was evaluated in order to define the actuator as a spring-mass system. During the process, assumptions were made to simplify the analysis. First, air viscous damping effects applied to the flapping beam surface were neglected. Second, nonlinear effects of the vibrating shell structure and the

piezo stack actuator due to thermal dissipation from the piezo stack actuator at high dynamic actuation states were not counted. Third, it was assumed that flexural deformation of the beam is restricted in the section between 'x' and 'y' in Figure 2.2(b). Finally, it was regarded that the spring constants of the upper and lower beams are identical, due to the symmetric shape of the oval loop shell.

2.4.1 Force Analysis

When the piezo stack actuator generates the force of 2P stretching out the shell structure in the horizontal direction, the force is distributed to each horizontal direction. The freebody diagram of the oval loop shell structure, when cut along the central, vertical line of symmetry, is shown in Figure 2.14(c). The flexural section of the beam (between 'x' and 'y') can be defined with an angle 'α' starting from the center of the shell ('x') and passing to the end of the flexural section ('y'). In the flexural section, the shell structure has a constant radius of 'R'. Therefore, the relation between 'a,' 'b,' 'α,' and 'R' can be expressed as:

$$\alpha = \tan^{-1}\left(\frac{a}{R-b}\right) \tag{2.3}$$

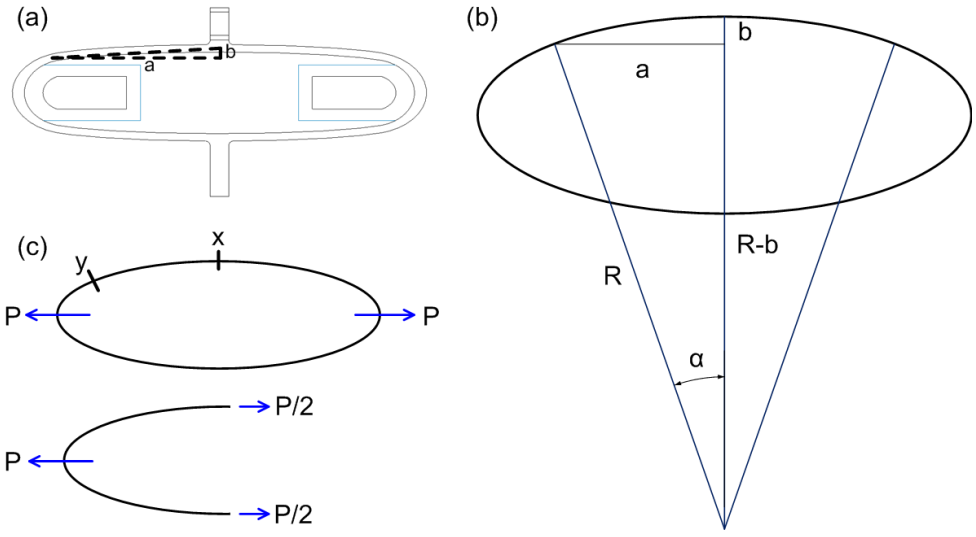

Figure 2.14: (a) Oval loop shell with two design parameters "a" and "b", (b) Radius of the oval loop beam, (c) Free body diagram with the applied force of, P, from the piezo stack actuator

The spring constants of the shell structure in the vertical and horizontal directions can be calculated separately by the use of Castigliano's theorem [94]. In the horizontal direction, the strain energy (U) stored in the flexural section (between 'x' and 'y') can be expressed as:

$$U = \int_0^s \frac{M^2 ds}{2EI} + \int_0^s \frac{N^2 ds}{2EA} + \int_0^s \frac{3V^2 ds}{5GA} \tag{2.4}$$

where S, E, G, A and I are beam length of flexural section, modulus of elasticity, shear modulus of elasticity, cross sectional area of the beam, and moment of inertia, respectively. M, N and V represent moment, normal and shear forces on a cut plane of the beam at arbitrary position within the flexural section (between 'x' and 'y'). Figure 2.15 shows freebody diagrams of the beam with M, N, and V. When the left end of the beam is assumed to be fixed support (since it is the end of the flexural section), initial moment (M_o) and normal force (P/2) are generated at the center cut plane of the oval loop

shell as shown in Figure 2.15(a). Figure 2.15(b) shows the freebody diagram of the beam when it is cut at the arbitrary angle (ø) starting from the center of the structure.

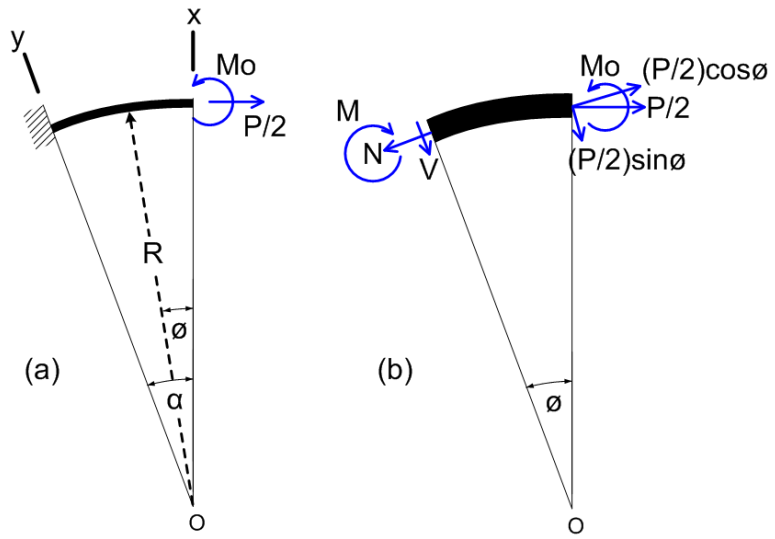

Figure 2.15: Freebody diagrams of the flexural section of the oval loop shell

Therefore, the reactions, M, N and V, at an arbitrary cut plane of the oval loop shell beam are calculated as:

$$N = \frac{P}{2}\cos\phi \tag{2.5}$$

$$V = -\frac{P}{2}\sin\phi \tag{2.6}$$

$$M = M_o - \frac{P}{2}R + \frac{P}{2}R\cos\phi \tag{2.7}$$

Equation (2.4) can be rewritten with as below:

$$U = \int_0^s \frac{M^2 R d\phi}{2EI_z} + \int_0^s \frac{N^2 R d\phi}{2EA} + \int_0^s \frac{3V^2 R d\phi}{5GA} \tag{2.8}$$

Above is the strain energy stored in the quadrant of the entire oval loop shell

structure due to moment, normal force, and shear force induced by the force 'P' from the PZT stack actuator. Therefore, the static horizontal displacement (δ_h) of the oval loop shell structure due to force, P, can be expressed as below:

$$\delta_h = 4\frac{dU_h}{dP} = \frac{4}{EI_z}\int_\beta^\alpha M\frac{dM}{dP}Rd\phi + \frac{4}{EA}\int_\beta^\alpha N\frac{dN}{dP}Rd\phi + \frac{24}{5GA}\int_\beta^\alpha V\frac{dV}{dP}Rd\phi \qquad (2.9)$$

Herein, the flexural section of the beam is re-defined as the bump in the center of the oval loop shell structure (Figure 2.14(a)) is regarded as a rigid section. Thus, 'β' indicates the actual starting angle of the flexural section next to the rigid bump in the center. In order to solve Equation (2.9), the initial moment, M_o, must be addressed. The initial moment (M_o) applied at the center cross section of the beam due to the load, P, can be calculated when assuming that no rotation occurs at the center symmetry plane of the shell structure due to M_o. Therefore, the following is valid:

$$\frac{dU}{dM_o} = \frac{1}{EI_z}\int_0^\alpha \frac{d}{dM_o}\left(\frac{M^2R}{2}\right)d\phi = 0 \qquad (2.10)$$

Equation (2.7) gives:

$$\frac{dM}{dM_o} = 1 \qquad (2.11)$$

and Equation (2.10) becomes:

$$\frac{dU}{dM_o} = \frac{1}{EI_z}\int_0^\alpha M\frac{dM}{dM_o}Rd\phi = 0 \qquad (2.12)$$

With further arrangements with Equation (2.11), Equation (2.12) becomes:

$$\frac{dU}{dM_o} = \int_0^\alpha \left(M_o - \frac{P}{2}R + \frac{P}{2}R\cos\phi\right)Rd\phi = 0 \qquad (2.13)$$

which gives:

$$M_o = \frac{P}{2} R(1 - \frac{\sin\alpha}{\alpha}) \tag{2.14}$$

After substituting Equation (2.14) into Equation (2.7), the moment along the beam becomes:

$$M = \frac{P}{2} R(\cos\phi - \frac{\sin\alpha}{\alpha}) \tag{2.15}$$

2.4.2 Spring Constants of OLSPA

The first term in the right hand side of Equation (2.9) is denoted as $\delta_{h,M}$:

$$\delta_{h,M} = 4\frac{dU_{h,M}}{dP} = \frac{4}{EI_z}\int_{\beta}^{\alpha} M\frac{dM}{dP} Rd\phi \tag{2.16}$$

where $U_{h,M}$ is the strain energy of the beam due to the moment M. Solving Equation (2.16) with Equation (2.15), we get the horizontal displacement of the oval loop shell structure due to the moment, M, as:

$$\delta_{h,M} = \frac{PR^3}{EI_z}\left[\frac{1}{2}\alpha + \frac{1}{4}\sin 2\alpha - \frac{\sin^2\alpha}{\alpha} - \frac{1}{2}\beta - \frac{1}{4}\sin 2\beta - \frac{2\sin\alpha\sin\beta}{\alpha} + \frac{\sin^2\alpha}{\alpha^2}\beta\right] \tag{2.17}$$

Similarly, the horizontal displacements due to the forces, N and V, are denoted as $\delta_{h,N}$ and $\delta_{h,V}$:

$$\delta_{h,N} = 4\frac{dU_{h,N}}{dP} = \frac{4}{EA}\int_{\beta}^{\alpha} N\frac{dN}{dP} Rd\phi \tag{2.18}$$

$$\delta_{h,V} = 4\frac{dU_{h,V}}{dP} = \frac{24}{5GA}\int_{\beta}^{\alpha} V\frac{dV}{dP} Rd\phi \tag{2.19}$$

Therefore, the horizontal displacements ($\delta_{h,N}$ and $\delta_{h,V}$) due to the normal and shear forces are calculated by solving Equations (2.18) and (2.19) with Equations (2.5) and (2.6) as below:

$$\delta_{h,N} = \frac{RP}{EA}\left[\frac{1}{2}(\alpha-\beta)+\frac{1}{4}(\sin 2\alpha-\sin 2\beta)\right] \tag{2.20}$$

$$\delta_{h,V} = \frac{3RP}{5GA}\left[\alpha-\beta+\frac{1}{2}(\sin 2\beta-\sin 2\alpha)\right] \tag{2.21}$$

Combining Equations (2.17), (2.20), and (2.21), the total horizontal displacement of the oval loop shell structure due to the force, P, is:

$$\begin{aligned}\delta_h &= \delta_{h,M}+\delta_{h,N}+\delta_{h,V}\\ &= P\left(\begin{array}{l}\dfrac{R^3}{EI_z}\left[\dfrac{1}{2}\alpha+\dfrac{1}{4}\sin 2\alpha-\dfrac{\sin^2\alpha}{\alpha}-\dfrac{1}{2}\beta-\dfrac{1}{4}\sin 2\beta-\dfrac{2\sin\alpha\sin\beta}{\alpha}+\dfrac{\sin^2\alpha}{\alpha^2}\beta\right]\\ +\dfrac{R}{EA}\left[\dfrac{1}{2}(\alpha-\beta)+\dfrac{1}{4}(\sin 2\alpha-\sin 2\beta)\right]\\ +\dfrac{3R}{5GA}\left[\alpha-\beta+\dfrac{1}{2}(\sin 2\beta-\sin 2\alpha)\right]\end{array}\right)\end{aligned} \tag{2.22}$$

Therefore, the spring constant ($k_{h,OLSPA}$) of the oval loop shell structure in the horizontal direction is:

$$\begin{aligned}k_{h,OLSPA} &= 1/\left(\begin{array}{l}\dfrac{R^3}{EI_z}\left[\dfrac{1}{2}\alpha+\dfrac{1}{4}\sin 2\alpha-\dfrac{\sin^2\alpha}{\alpha}-\dfrac{1}{2}\beta-\dfrac{1}{4}\sin 2\beta-\dfrac{2\sin\alpha\sin\beta}{\alpha}+\dfrac{\sin^2\alpha}{\alpha^2}\beta\right]\\ +\dfrac{R}{EA}\left[\dfrac{1}{2}(\alpha-\beta)+\dfrac{1}{4}(\sin 2\alpha-\sin 2\beta)\right]\\ +\dfrac{3R}{5GA}\left[\alpha-\beta+\dfrac{1}{2}(\sin 2\beta-\sin 2\alpha)\right]\end{array}\right)\end{aligned} \tag{2.23}$$

The spring constant of either upper or lower beam in the horizontal direction is half of $k_{h,OLSPA}$:

$$k_{h,beam} = \frac{1}{2}k_{h,OLSPA} \tag{2.24}$$

The spring constants in the vertical direction can be calculated by repeating the same

process as done for the horizontal direction with the fictitious force Q applied in the vertical direction at the center of the shell structure, as shown in Figure 2.16.

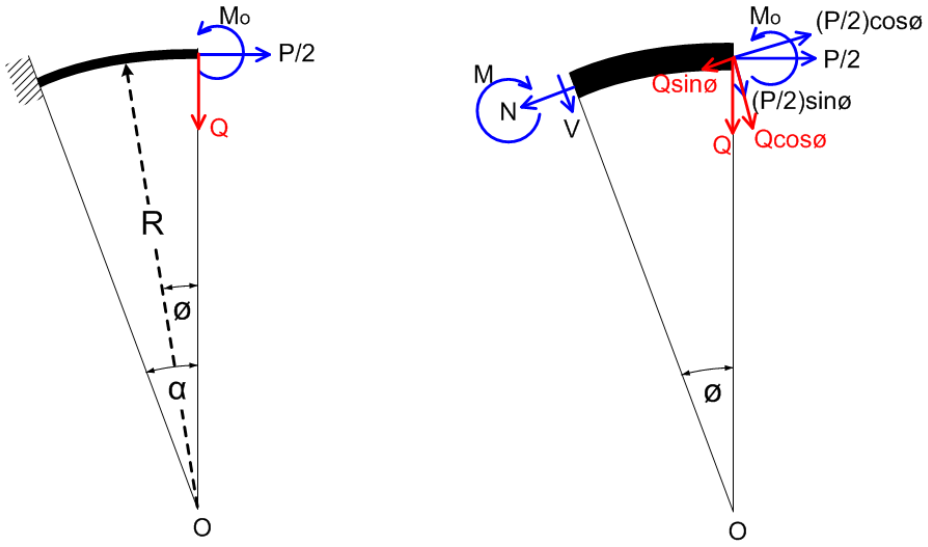

Figure 2.16: Freebody diagrams of the flexural section of the oval loop shell with a fictitious force applied in the vertical direction

Force analysis with the fictitious force, Q, provides new terms for the moment, normal, and shear forces along the cross sections of the beam as:

$$N = \frac{P}{2}\cos\phi - Q\sin\phi \tag{2.25}$$

$$V = -\frac{P}{2}\sin\phi - Q\cos\phi \tag{2.26}$$

$$M = M_o - \frac{P}{2}R + \frac{P}{2}R\cos\phi - RQ\sin\phi \tag{2.27}$$

Repeating the same process, as done through Equations (2.10) and (2.15) for the horizontal direction, the final expression for the moment M is obtained as:

$$M = QR\left(\frac{1-\cos\alpha}{\alpha} - \sin\phi\right) + \frac{P}{2}R\left(\cos\phi - \frac{\sin\alpha}{\alpha}\right) \tag{2.28}$$

Therefore, the static vertical displacement (δ_v) of the oval loop shell structure due to the

fictitious force, Q, can be expressed as below:

$$\delta_v = 4\frac{dU_v}{dQ} = \frac{4}{EI_z}\int_\beta^\alpha M\frac{dM}{dQ}Rd\phi + \frac{4}{EA}\int_\beta^\alpha N\frac{dN}{dQ}Rd\phi + \frac{24}{5GA}\int_\beta^\alpha V\frac{dV}{dQ}Rd\phi \qquad (2.29)$$

After solving each term of Equation (2.29) with the substitutions of Equations (2.25 ~ 2.27) and eliminating the terms with the fictitious force, Q, the vertical displacement, δ_v, becomes:

$$\begin{aligned}\delta_v &= \delta_{v,M} + \delta_{v,N} + \delta_{v,V} \\ &= P\left[\begin{array}{l}\dfrac{2R^3}{EI_z}\left[\begin{array}{l}\dfrac{1}{4}\cos 2\alpha - \dfrac{\sin\alpha\cos\alpha}{\alpha} - \dfrac{\sin\beta}{\alpha} + \dfrac{\sin\beta\cos\alpha}{\alpha} + \\ \beta\dfrac{\sin\alpha}{\alpha}\dfrac{1-\cos\alpha}{\alpha} - \dfrac{1}{4}\cos 2\beta + \dfrac{\sin\alpha\cos\beta}{\alpha}\end{array}\right] \\ + \dfrac{2R}{EA}\left[\cos(2\alpha) - \cos(2\beta)\right] \\ + \dfrac{12R}{5GA}\left[\cos(2\beta) - \cos(2\alpha)\right]\end{array}\right]\end{aligned} \qquad (2.30)$$

which gives the spring constant of the oval loop shell structure in the vertical direction as:

$$\begin{aligned}k_{v,OLSPA} &= 1/\left[\begin{array}{l}\dfrac{2R^3}{EI_z}\left[\begin{array}{l}\dfrac{1}{4}\cos 2\alpha - \dfrac{\sin\alpha\cos\alpha}{\alpha} - \dfrac{\sin\beta}{\alpha} + \dfrac{\sin\beta\cos\alpha}{\alpha} \\ + \beta\dfrac{\sin\alpha}{\alpha}\dfrac{1-\cos\alpha}{\alpha} - \dfrac{1}{4}\cos 2\beta + \dfrac{\sin\alpha\cos\beta}{\alpha}\end{array}\right] \\ + \dfrac{2R}{EA}\left[\cos(2\alpha) - \cos(2\beta)\right] \\ + \dfrac{12R}{5GA}\left[\cos(2\beta) - \cos(2\alpha)\right]\end{array}\right]\end{aligned} \qquad (2.31)$$

Therefore, the spring constant of either upper or lower beam in the vertical direction is half of $k_{v,OLSPA}$:

$$k_{v,beam} = \frac{1}{2} k_{v,OLSPA} \tag{2.31}$$

2.4.3 Operating Frequency

In Figure 2.17, the piezoelectric translational agitator system is expressed as a simple schematic with two simplified flexural beam elements connected through links and two lumped masses representing effective moving masses of the system.

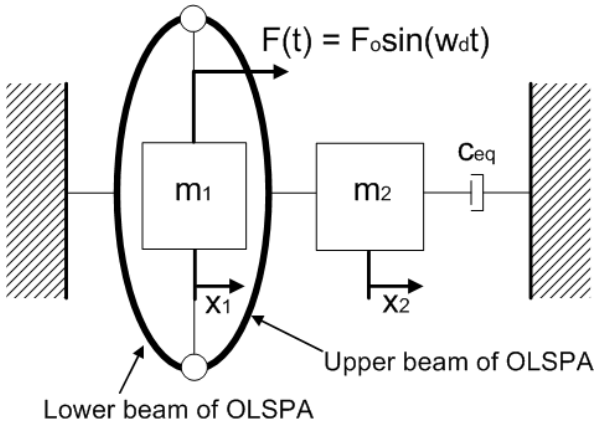

Figure 2.17: Simplified schematic of agitator system

The mass, m_1, includes mass for the PZT stack actuator, stationary parts of the oval loop shell structure, and effective moving mass of the lower beam. The mass, m_2, represents a carbon fiber blade and effective moving mass of the upper beam of the oval loop shell. As the lower beam is fixed at the support (left end of the oval loop shell in Figure 2.17), m_1 and m_2 generate displacements as the PZT stack actuator stretches out in the center of the oval loop shell structure. These displacements of m_1 and m_2 are denoted as x_1 and x_2. Sinusoidal driving force from the PZT stack actuator is F(t). C_{eq} represents a damping coefficient due to the air viscous damping exerted on the oscillating blade when the agitator is its dynamic motion. By replacing two flexural beam elements in Figure

2.17 with springs, the agitator system could be depicted with two-degree-of-freedom (TDOF) system as shown in Figure 2.18.

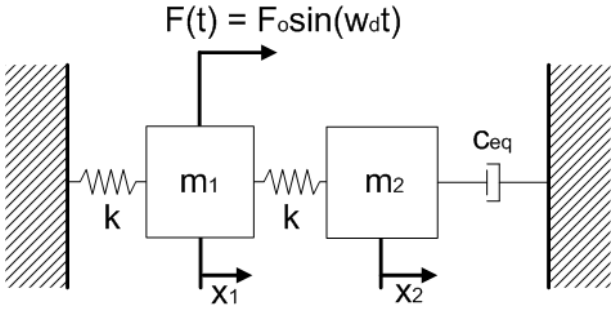

Figure 2.18: Two-degree-of-freedom spring-mass system of piezoelectric translational agitator

The spring constant of either upper or lower beam of the oval loop shell structure has been already defined in the previous section and they are assumed to be identical each other having the same spring constant, k. Therefore, free body diagrams of m_1 and m_2 are defined as shown in Figure 2.19.

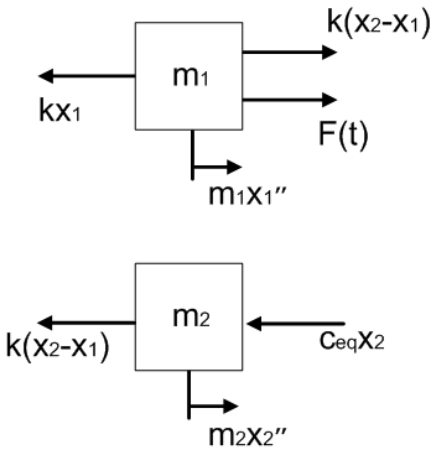

Figure 2.19: Free body diagrams of two moving masses of the agitator

The free body diagrams in Figure 2.19 provide the equations of motion in the vector form as below:

$$\begin{bmatrix} m_1 & 0 \\ 0 & m_2 \end{bmatrix}\begin{bmatrix} x_1'' \\ x_2'' \end{bmatrix}+\begin{bmatrix} 2k & -k \\ -k & k \end{bmatrix}\begin{bmatrix} x_1 \\ x_2 \end{bmatrix}+\begin{bmatrix} 0 \\ c_{eq} \end{bmatrix}\begin{bmatrix} x_1' \\ x_2' \end{bmatrix}=\begin{bmatrix} F(t) \\ 0 \end{bmatrix} \tag{2.32}$$

Solving an eigenvalue problem with Equation (2.32), two natural frequencies of the TDOF spring-mass system can be obtained (currently solved with MATLAB software). The comparison between the estimated natural frequencies from Equation (2.32) and the measured resonance frequencies of the oval loop shell actuators are listed in Table. 2.3.

Table 2.3: Frequency comparisons between the experimental and analytical results

	Experiment (Hz)		**Theory (Hz)**		**Difference (%)**	
	First mode	Second mode	First mode	Second mode	First mode	Second mode
Shell 1	318	1200	333	1186	4.6	-1.2
Shell 2	375	1341	392	1355	4.4	-1.0
Shell 3	251	961	275	960	9.4	-0.3
Shell 4	284	1108	323	1088	13.7	-4.8
Shell 5	376	1398	393	1236	5.8	-4.0
Shell 6	403	1444	428	1422	6.1	-1.5

The analytical calculations predict well two natural frequencies of the oval loop shell structures within an error of 14 %. For the first mode, the analytical modeling overpredicts and shows the largest difference of 13.7 % for shell 4. For the second mode, the analytical method predicts well the natural frequencies and shows error within 5 %.

2.5 Fatigue Analysis

The oval loop shell piezo actuator should provide high-frequency oscillation (up to around 1 kHz) with large translational displacements (around 10% strain of the oval loop shell structure) to the blade using flexural deformation of the beam at the structure's resonance. The agitation should take place for a long period of time to keep electronics or heated components cool during their operations over a reasonable lifetime of device operation. Therefore, these high dynamic operating conditions of the agitator require high

fatigue endurance limit in the design of the oval loop shell structure. Some design features to increase fatigue strength of the shell structure were discussed in the previous section (2.3.1 Design and Fabrication). In this section, the more detailed fatigue analysis of the oval loop shell piezo actuator is performed and the results are provided.

When the PZT stack actuator is squeezed in the center of the oval loop shell structure through the two inner connector pieces, a pre-stress is given to ensure good transmission of energy from the PZT stack to the oval loop shell by shortening the distance between the two inner connectors and the PZT stack. The pre-stress also provides secured dynamic operation of the PZT stack with large applied load according to the supplier's recommendation [95]. Therefore, this pre-stress (σ_{pre}) is the minimum stress applied to the oval loop shell structure during dynamic operation of the agitator.

$$\sigma_{min} = \sigma_{pre} \tag{2.33}$$

The PZT stack actuator generates alternating stress in addition to the pre-stress as it provides an oscillation source to the oval loop structure. Figure 2.20 illustrates a fluctuating stress of the oval loop shell piezo actuator during its dynamic operation.

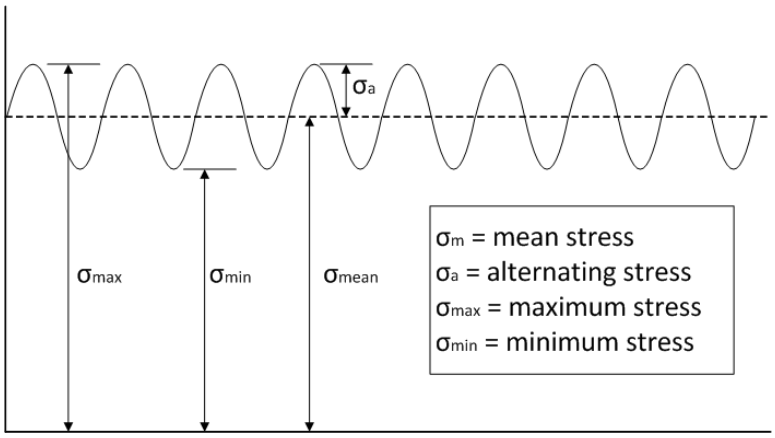

Figure 2.20: Fluctuating stress notation of the oval loop shell piezo actuator

The PZT stack always makes a tensile load, stretching the oval loop shell in the horizontal direction of Figure 2.2(b) as positive sinusoidal voltage is applied during the dynamic operation. Thus, the alternating stress starts from the minimum stress point to its maximum stress point. The relationships between the stresses are summarized as below:

$$\sigma_m = \frac{\sigma_{max} + \sigma_{min}}{2} \tag{2.34}$$

$$\sigma_a = \frac{\sigma_{max} - \sigma_{min}}{2} \tag{2.35}$$

The pre-stressed force ($2P_{pre}$) can be calculated by Hooke's law with the spring constant ($k_{h,OLSPA}$) of the oval loop shell structure in the horizontal direction and pre-stressed length (L_{pre}) that is given for squeezing the stack in the shell structure as:

$$2P_{pre} = k_{h,OLSPA} \times L_{pre} \tag{2.36}$$

The force $2P_{pre}$ is distributed to the both directions of the shell structure. The reactions exerted on the cross sections of the shell due to the force $2P_{pre}$ can be calculated from Equations (2.5), (2.6), and (2.15) as below:

$$N_{pre} = \frac{P_{pre}}{2}\cos\phi \tag{2.37}$$

$$V_{pre} = -\frac{P_{pre}}{2}\sin\phi \tag{2.38}$$

$$M_{pre} = \frac{P_{pre}}{2}R(\cos\phi - \frac{\sin\alpha}{\alpha}) \tag{2.39}$$

The corresponding axial ($\sigma_{pre,n}$), shear (τ_{pre}), and bending ($\sigma_{pre,b}$) stresses due to the force P_{pre} are summarized as below:

$$\sigma_{pre,n} = K_{t,a}\frac{N_{pre}}{A_{sc}} = K_{t,a}\frac{P_{pre}}{2A_{sc}}\cos\phi \tag{2.40}$$

$$\tau_{pre} = \frac{V_{pre}}{A_{sc}} = -\frac{P_{pre}}{2A_{sc}}\sin\phi \tag{2.41}$$

$$\sigma_{pre,b} = K_{t,b}\frac{M_{pre}y_c}{I_z} = K_{t,b}\frac{P_{pre}y_c}{2I_z}R(\cos\phi - \frac{\sin\alpha}{\alpha}) \tag{2.42}$$

where A_{sc}, y_c, and I_z are the cross sectional area of the beam, the distance from the neutral axis, and the moment of inertia of the cross section with respect to the neutral axis. And $K_{t,a}$ and $K_{t.b}$ represent a stress concentration factor associated with geometric configurations for determining maximum stress at design points. A curvature factor is negligible as the radius of the beam is much larger than the thickness of the beam. Therefore, the pre-stress (σ_{pre}) is the sum of $\sigma_{pre,n}$ and $\sigma_{pre,b}$:

$$\sigma_{pre} = \sigma_{pre,n} + \sigma_{pre,b} = \sigma_{min} \tag{2.43}$$

As discussed in Equation (2.33) the pre-stress (σ_{pre}) becomes the minimum stress (σ_{min}) in Figure 2.20. The alternating stress (σ_a) in Figure 2.20 is generated by the PZT stack during the operation. The reactions due to the force, P, generated by the PZT stack

at the cross section of the beam can be obtained from Equations (2.5), (2.6), and (2.15). The corresponding stresses are obtained similarly as done through Equations (2.40), (2.41), and (2.42) for the pre-stress and expressed below:

$$\sigma_n = K_{t,a} \frac{P}{2A_{sc}} \cos\phi \tag{2.44}$$

$$\tau = -\frac{P}{2A_{sc}} \sin\phi \tag{2.45}$$

$$\sigma_b = K_{t,b} \frac{Py_c}{2I_z} R(\cos\phi - \frac{\sin\alpha}{\alpha}) \tag{2.46}$$

Therefore, the alternating stress (σ_a) becomes as:

$$\sigma_a = \frac{\sigma_n + \sigma_b}{2} \tag{2.47}$$

As a result, the mean (σ_m) stress can be obtained from Equations (2.34), (2.35), and (2.47). In Figure 2.21, the stresses due to the forces P_{pre} and P are illustrated in the stress diagrams of the beam element of the shell structure.

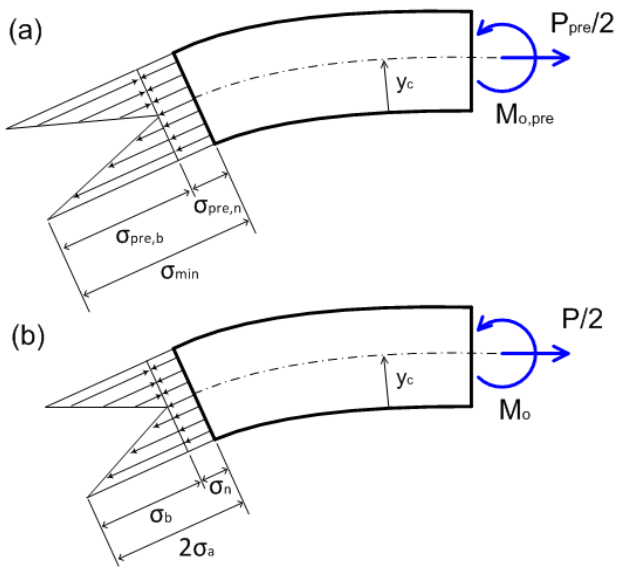

Figure 2.21: Stress diagrams of the beam element, (a) Pre-stresses due to the pre-load 'P_{pre}', (b) Stresses due to the force 'P' from the PZT stack actuator

Shell 3 in Table 2.1 are selected for detailed fatigue analysis since it has the most desirable operating conditions for heat transfer experiments. It is assumed that Shell 3 is operating with an applied voltage of 140 V that produces about 361 N of maximum static tensile force from the PZT stack actuator according to the following equation [95]:

$$P_{max} = k_{PZT} \cdot \Delta d \left(1 - \frac{k_{PZT}}{k_{PZT} + k_{h,OLSPA}} \right) \tag{2.48}$$

where k_{PZT} and Δd are the stiffness and peak-to-peak displacement of the PZT stack actuator. This is a conservative assumption because dynamic force generation from a PZT stack actuator is generally lower than the static force generation [95]. The pre-stress length of 100 μm was given. Shell 3 has a flexural section between ø = 0.009 rad and ø = 0.157 rad as shown in Figure 2.22. The bump in the center of the beam (ø = 0 ~ 0.009 rad) is considered as a rigid section and is not counted as a flexural section for fatigue analysis.

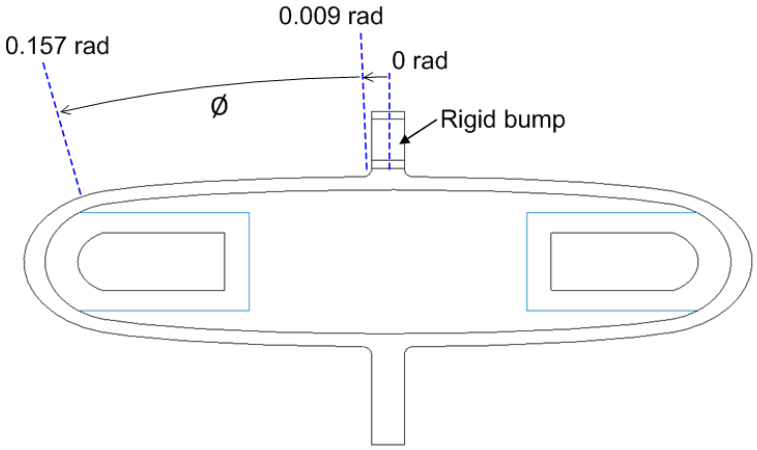

Figure 2.22: Flexural section of the beam from Shell 3

The mean and alternating stresses along the flexural section of the beam from adjacent to the bump to the end of the beam are calculated and plotted in Figure 2.23. When calculating the stresses at the right adjacent to the bump (ø = 0.009 rad), the stress concentration factors (K) of 1.36 and 1.27 are used for the normal and bending stresses, respectively, due to the abrupt spatial contraction.

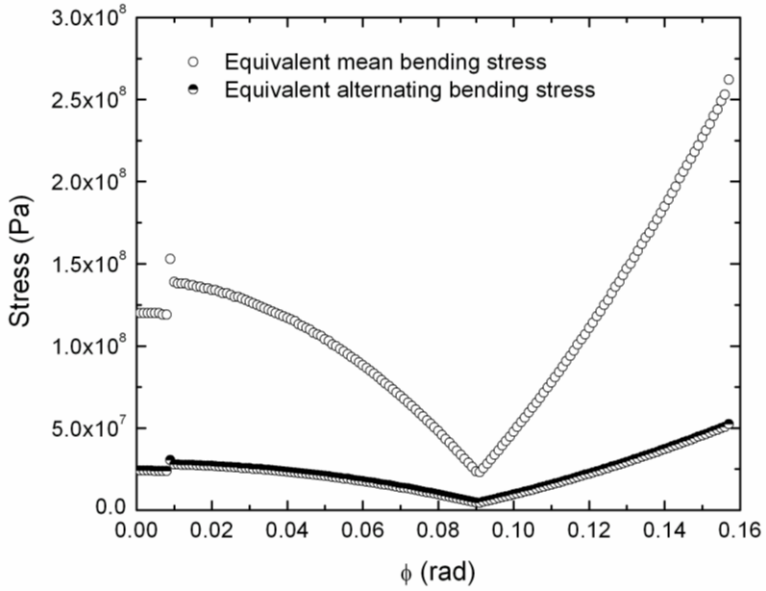

Figure 2.23: Mean and alternating stresses along the flexural beam of the oval loop shell structure, shell 3

The normal and alternating stresses gradually decrease until ø = 0.09 rad with increasing beam angle with an initial sudden drop of stresses at ø = 0.009 rad (next to the bump). After ø = 0.09 rad the stresses turn up and increase until the end of the beam at ø = 0.157 rad. Therefore, fatigue failure is most likely to take place at the end of the flexural section of the beam at ø = 0.157 rad. Figure 2.24 shows a fatigue strength diagram of shell 3 at various points with different angle over the flexural section of the beam. The oval loop shells are made of 5160 spring steel. The material properties and generalized fatigue strength factors [96] for determining the endurance limit are listed in Table 2.4. It is shown that all the points along the flexural section of the beam are far under the endurance limit line indicating that Shell 3 is safe for using it as an agitation cooling device. In addition, Figure 2.25 also shows that six shells from Table 2.1 have infinite lifetime at the end of flexural beam section.

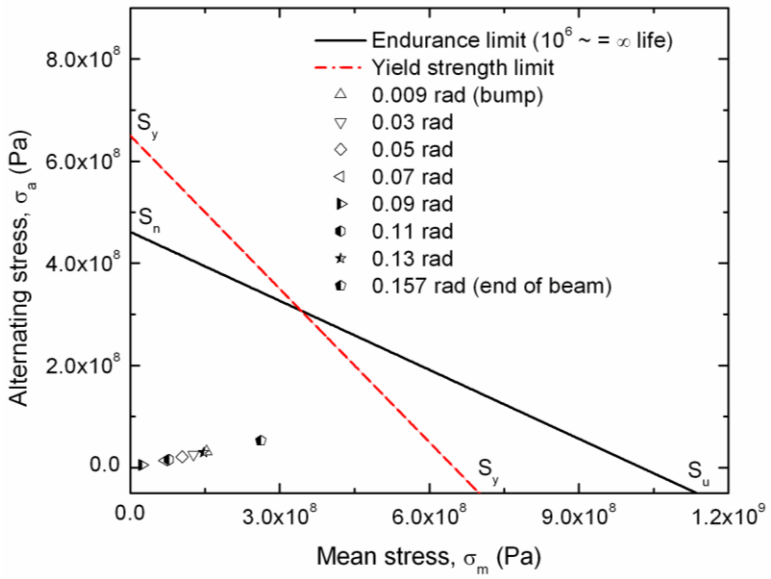

Figure 2.24: Fatigue strength diagram at various points on the flexural beam of Shell 3

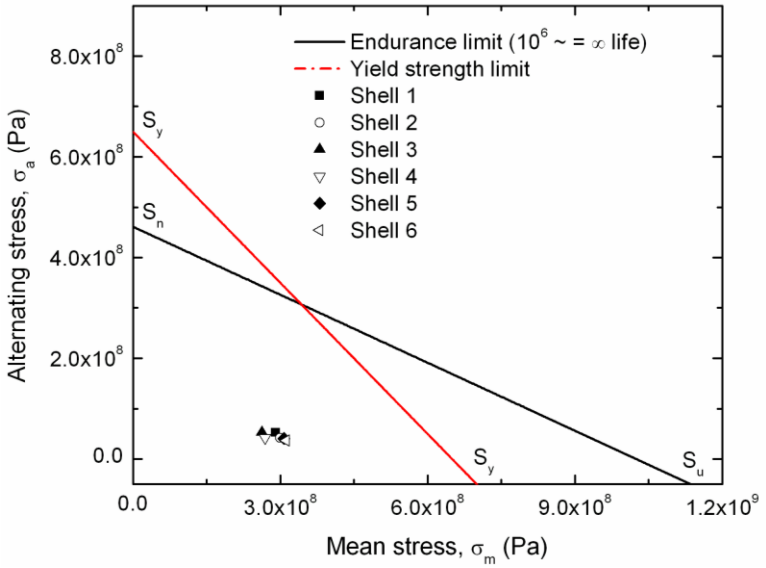

Figure 2.25: Fatigue strength diagram of six shells at the end of flexural beams

Table 2.4: Material properties and generalized fatigue strength factors for fatigue analysis

Material	5160 Spring Steel
Ultimate strength, S_u, (pa)	1.03E+09
Yield strength, S_y, (pa)	6.50E+08
CL (load factor)	1
CG (gradient factor)	1
CS (surface factor)	0.9
$S_n' = 0.5S_u$	5.13E+08
$S_n = S_n' \cdot CL \cdot CG \cdot CS$	4.61E+08

2.6 Single-Blade Piezoelectric Translational Agitator (PTA)

2.6.1 Principle of PTA

An oval loop shell structure and a PZT stack actuator are utilized to achieve high-frequency translational movement of a blade with oscillating amplitudes sufficiently large to provide cooling capability to the heat source. A schematic of the Piezoelectric Translational Agitator (PTA) that consists of the PZT stack actuator, the oval loop shell, and a carbon fiber single-blade structure is shown in Figure 2.26.

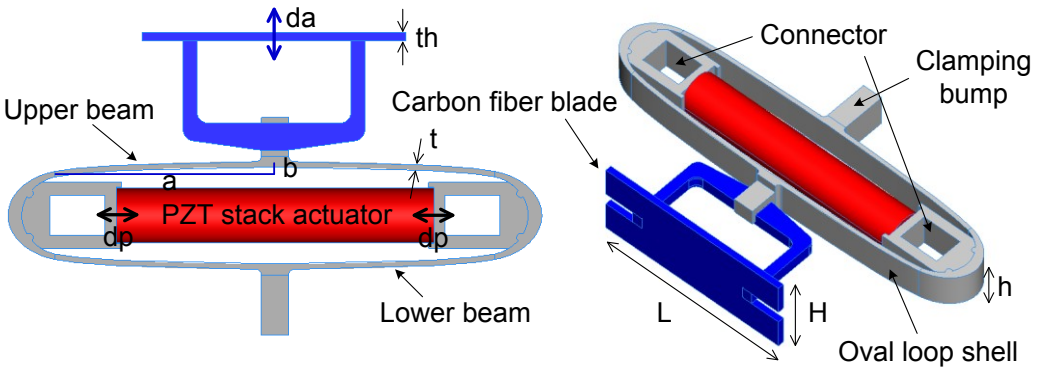

Figure 2.26: Schematic of piezoelectric translational agitator

The PZT stack actuator normally generates very small translational displacements of tens of microns, which is around 0.1% of the strain range of its own actuator. The oval loop shell structure significantly amplifies small displacements of the PZT stack actuator using resonance energy of the structure. The PZT stack actuator generates displacement of "2dp" (Figure 2.26) in the horizontal direction and the oval loop shell amplifies the movement in the vertical direction. When the operating frequency of the PZT stack actuator approaches one of the natural frequencies of the oval loop shell structure, highly amplified translational movement ("da", arrow in Figure 2.26) is generated in the vertical direction and transferred to the blade structure attached to the oval loop shell, providing strong air current that can be used for cooling purposes. At resonance, either the upper or the lower beam of the shell is excited vigorously. There are two appropriate resonance modes of the PTA within a 2 kHz frequency range that can provide amplified translational motion. For the first resonance mode, the bottom beam of the shell is mainly excited, moving the entire agitator body up and down. For the second resonance mode, only the upper beam is excited conveying translational movement to the blade.

The PTA operating at the two resonance modes is shown in Figure 2.27. Figures

2.27 (a) and (b) show the PTA operating at the first resonance mode. In Figure 2.27(b), it is confirmed that the lower beam is flapping and the movement seen as a blur, formed along the entire agitator body, except for the center area of the lower beam. Figures 2.27 (c) and (d) show the PTA operating in the second resonance mode. In Figure 2.27(d), it is clearly seen that the upper beam is strongly excited, providing large translational motion to the blade while the remainder of the agitator is stable.

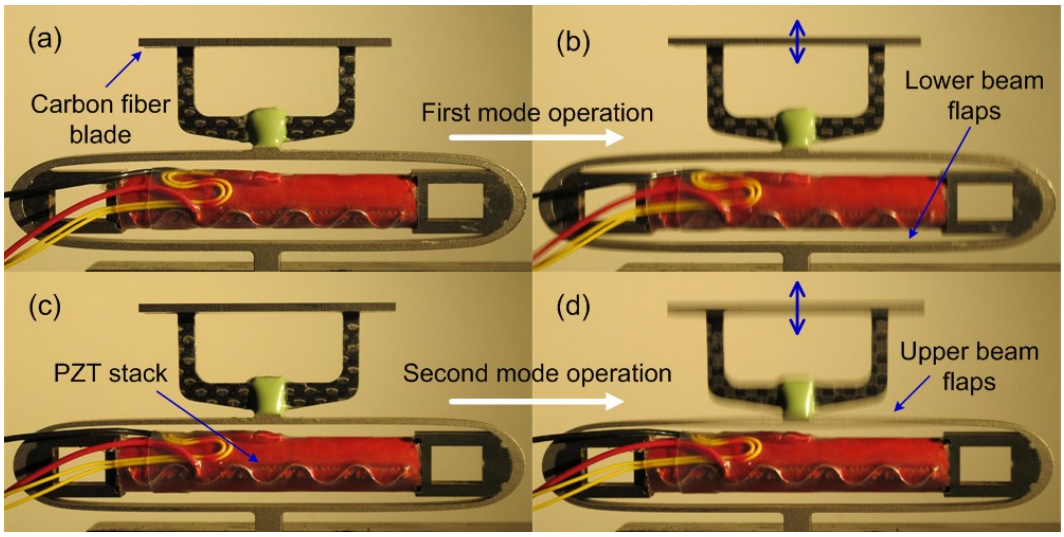

Figure 2.27: PTAs operating under the two different resonance modes

Three design parameters, “a”, “b”, and “t,” shown in Figure 2.26 characterize the operating performance of the shell. A carbon fiber composite plate was used for the blade structure due to its very high stiffness-to-weight ratio compared to metals. The weight of the carbon fiber single-blade structure is about 2 grams. The blade mounted at the top of the oval loop shell produces strong air currents adjacent to the heated surface by generating high-frequency translational oscillation. Four different PTAs with single-blade are designed and fabricated for single channel heat transfer tests. The design parameters and dimensions of the PTAs with the single-blade are summarized in Table 2.5.

Table 2.5: Design parameters and dimensions of the piezoelectric translational agitators

	Oval Loop Shell				Carbon Fiber Blade		
	a (mm)	b (mm)	t (mm)	h (mm)	L (mm)	H (mm)	th (mm)
PTA-1	40	1.8	1.0	8.0	48	18	1.5
PTA-2	40	1.8	1.2	8.0	48	18	1.5
PTA-3	40	1.8	1.6	8.0	48	18	1.5
PTA-4	35	1.7	1.7	8.0	48	18	1.5

2.6.2 Vibrational Characteristics of Single-Blade PTAs

Vibration characteristics of the PTAs are investigated with the PSV-400 laser Doppler vibrometer from Polytec. A schematic of the vibration test arrangement is illustrated in Figure 2.28. This is a similar test facility for investigating the oval loop shell piezo actuators introduced in the previous section. A mechanical vice is used to clamp the PTA on the optical table and a vertically-mounted laser vibrometer scanning head is shooting a laser on the surface of the blade. In order to account for air damping effects of the actuating agitator when it is inside the channel, measurements were taken inside a transparent channel made of clear plastic plates, shown in Figure 2.28.

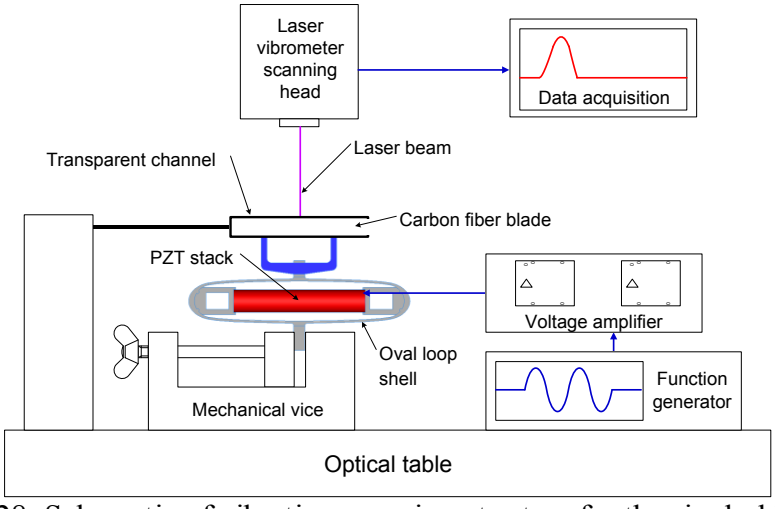

Figure 2.28: Schematic of vibration experiment set up for the single-blade PTA

The VF-500 linear piezoelectric voltage amplifier (Dynamic Structures & Materials, LLC) was used to provide high voltage to the PTAs. Alternative current signals were generated by the AFG3102 function generator from Tektronix, Inc. As shown in Figure 2.29, mean-to-peak displacements per unit of applied voltage of the PTAs were measured in the frequency domain over the range 0 Hz to 2 kHz. For each PTA, two resonance peaks were found in the frequency range. The first mode, which peaks at relatively lower frequencies of less than 500 Hz, exhibits smaller displacements than those of the second mode peaks. The second mode peaks appear at higher frequencies of above 500 Hz and up to 1.1 kHz. In addition, the second mode provides a much larger displacement than the first mode. The resonance frequencies of each PTA are listed in Table 2.6.

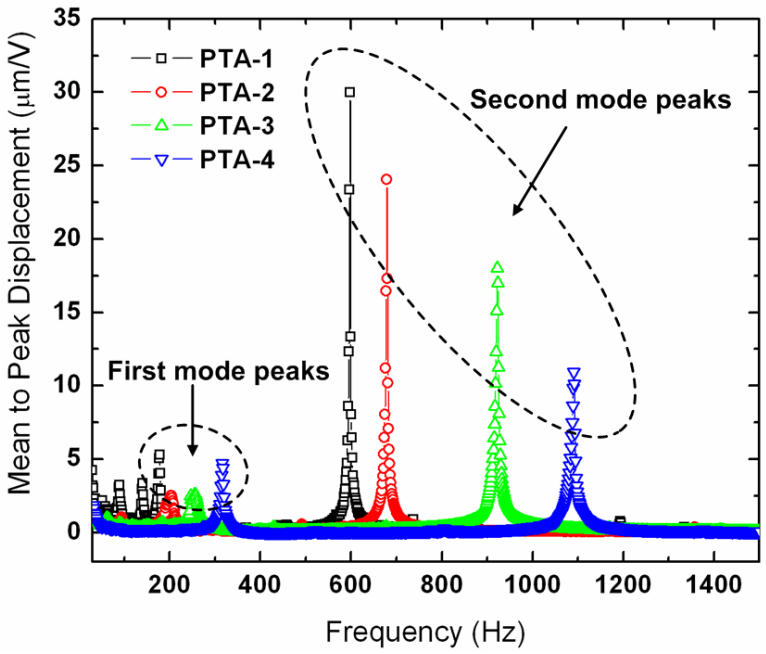

Figure 2.29: Displacements of the single-blade PTAs

Table 2.6: Resonance frequencies of the single-blade PTAs

	Resonance Frequency (Hz)	
	The First Mode	**The Second Mode**
PTA-1	178	596
PTA-2	203	673
PTA-3	256	921
PTA-4	316	1080

Generally, the oval loop shell becomes stiffer as the design parameter "a" decreases and the thickness "t" increases. Therefore, the PTA-4 actuator has the largest resonance frequencies, but produces the smallest displacement with the same applied voltage. On the other hand, the PTA-1 actuator has the smallest resonance frequencies and the largest displacements among the four PTAs. As the second mode operation provides larger displacement and higher frequency than the first mode, the second mode is regarded as the more appropriate for this cooling application. For effective comparisons of heat transfer test results using different PTAs, seven displacements were selected and the corresponding voltages for the various PTAs were measured for the second mode so that the displacement is consistent for each heat transfer test. However, the intrinsic capability of each PTA toward generating dynamic flexural displacement is different due to different stiffnesses of the oval loop shell structures. Therefore, the largest displacements used for the heat transfer testing purpose with PTA-3 and PTA-4 are 1.4 mm and 0.8 mm, respectively, while the largest displacement of PTA-1 or PTA-2 is 1.8 mm. The displacements of each PTA used for heat transfer testing and their corresponding applied voltages are listed in Table 2.7.

Table 2.7: Dynamic displacements of the single-blade PTAs for heat transfer testing and their corresponding applied voltages

Displacement (mm)		0.4	0.6	0.8	1.0	1.2	1.4	1.8
Voltage (V)	PTA-1	11.6	22.0	35.0	49.0	64.0	80.0	126.0
	PTA-2	16.0	30.0	50.0	68.0	90.0	116.0	180.0
	PTA-3	25.8	48.0	72.0	98.0	122.0	152.0	
	PTA-4	45.0	86.0	188.0				

Peak velocities of the PTAs for each displacement value were also measured, as shown in Figure 2.30. Overall, the peak velocities increase almost linearly with increasing displacement. For all the cases, the peak velocities range from 0.7 m/s to 4.6 m/s within the ranges of displacements and frequencies. The largest velocity is from PTA-3, with a displacement of 1.6 mm.

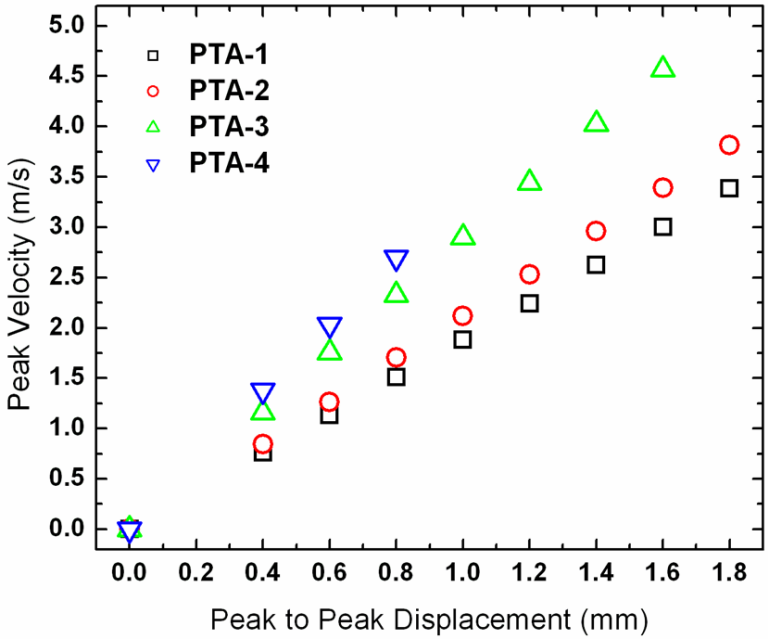

Figure 2.30: Peak velocities of the PTAs at each displacement

2.7 Noise of PTAs

Noise of a cooling device could be an important issue in many engineering applications, including electronics cooling. Therefore, a brief discussion about the noise

aspect of the PTAs is provided in this section. The PTA creates high-frequency and large-displacement oscillating motion to the beam elements of the device; thereby, it generates strong acoustic pressure waves to the ambient air resulting in substantial noise. A 12.5 mm (1/2 inch) Free-field microphone (Type 40AE) from GRAS Sound and Vibration was used to measure the noise. The microphone was placed at one meter away from the PTAs. The A-weighted noise levels for each of PTA-1 and PTA-3 at different displacements are listed in Table 4. The background noise level is around 46 dB, which is in the range of typical noise level in an office environment. The PTA-3 actuator, operating at 921 Hz, generates about 20% larger noise level in dB than the PTA-1 actuator with an operating frequency of 596 Hz for cases of various displacements. The noise level also tends to increase with increasing displacement at a fixed frequency. If the PTA operation raises a noise problem, solutions, such as using a muffler [97, 98], can be found. It is found that a muffler used with PTA actuators similar to those discussed above could lower the noise level 40 dB.

2.8 Conclusion

The piezoelectric actuator with high frequency, large displacement, and low power consumption was successfully designed and fabricated based on the flexural oval loop shell structure. The shell amplifies the displacement of the piezo stack actuator and generates dynamic translational movement using resonant energy of the structure. In order to enhance fatigue strength of the actuator, shot peening was applied to the surfaces of the oval loop shells. After treatment, the fatigue strength was enhancement and the life-time of the actuator increased significantly. A detailed fatigue analysis is provided

and results showed that the given oval loop shell piezo actuators are safe for the agitator purpose. At the second mode of resonance, the highest frequency achieved was 1,444 Hz with an amplified displacement of around 1.5 mm when 100 VAC was applied to the actuator. The largest displacement of more than 2.0 mm was achieved with an operating frequency of 961 Hz. The theoretical solution was proposed to predict the natural frequencies of the oval loop shell actuator and showed a maximum error of around 12 % compared to the results of experiments. The calculated actuator efficiency is around 50 % when the minimal load of 3.1 g is applied to shell 3 with an applied voltage of 140 V. The performance of the actuator is not restricted to the current design parameters in this paper. The operating conditions, such as the resonance frequency and the amplified displacement, can be easily controlled to fulfill needs of specific applications by changing the design parameters. When more electrical power is available to the piezo stack actuator, higher displacement of dynamic actuation is possible. The current piezoelectric oval loop actuators can be utilized in applications where high-frequency translational movement with larger displacements is needed.

Four piezoelectrically-driven, in-channel flow agitator designs were fabricated and tested as potential electronics cooling devices. In order to create a high-frequency and large-displacement translational motion, an oval loop shell structure was made of spring steel. It successfully amplified a few microns of piezoelectric stack range to the millimeter displacement ranges needed for the agitators. The oval loop shell mainly uses the second resonant mode of the structure so that the agitator is excited and the

piezoelectric stack is not. The operating frequencies of the four PTAs range from 596 Hz to 1080 Hz with amplified displacements of up to 1.8 mm.

Chapter 3:
Translational Agitation over a Plain (Smooth) Surface

3.1. Objective of the Chapter

In this section, we investigate thermal performance of a single-blade piezoelectric translational agitator over a plain surface. The piezoelectric translational agitator tested here normally operates at relatively higher frequencies, above 500 Hz up to more than 1 kHz, with large amplitudes of ~1.0 mm. The detailed operating conditions of the agitators are already discussed in the previous sections (Table 2.4 and Table 2.5). Due to the translational movement of a blade, the heated area that falls within the domain of a blade can be provided with consistent cooling from agitator-driven air. In order to investigate cooling performance of the piezoelectric translational agitator either as a stand-alone device or a supplemental device to the fan, heat transfer experiments were performed with the agitator inside a channel that simulates a heat sink channel. For comparison, tests were run with the agitator and with fan assistance or with no fan assistance.

3.2 Single Channel Heat Transfer Experiment

3.2.1 Experimental Set Up

Heat transfer experiments were conducted at various operating conditions for four PTAs to demonstrate the cooling performance of the PTA. The heat transfer facility is illustrated in Figure 3.1. The test section simulates a portion of a heat sink channel with a heated surface on one side. A long, rectangular copper block constitutes the convection

surface. A cartridge heater was inserted at the end of the copper block and the energy conducts from the heater to the exposed surface inside the channel.

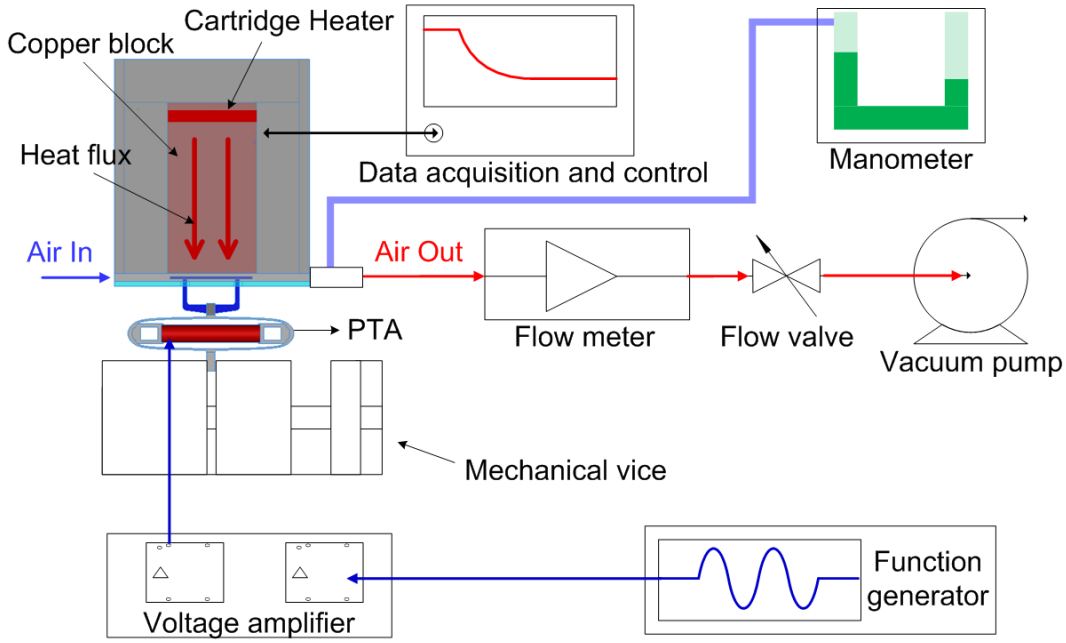

Figure 3.1: Schematic of heat transfer experiment set up for the PTA

The copper block is surrounded by thick Styrofoam insulation blocks to ensure that nearly all the energy from the heater is conducted to the channel wall and is available for convection. A narrow and long channel is formed along the exposed surface of the copper block using transparent plastic plates. The PTA plate oscillates adjacent to the exposed surface. A blower generates flow through the channel. A pressure tap at the outlet of the channel gives access to the exit static pressure. A u-shape water manometer is used to measure the pressure drop from the upstream ambient pressure (the upstream stagnation pressure) to the downstream static pressure, giving the pressure loss through the test section. The function generator provides AC voltage and the piezoelectric voltage

amplifier provides amplified voltage to the PTA. A flow meter between the test section and the vacuum pump measures volume flow rate of the channel flow.

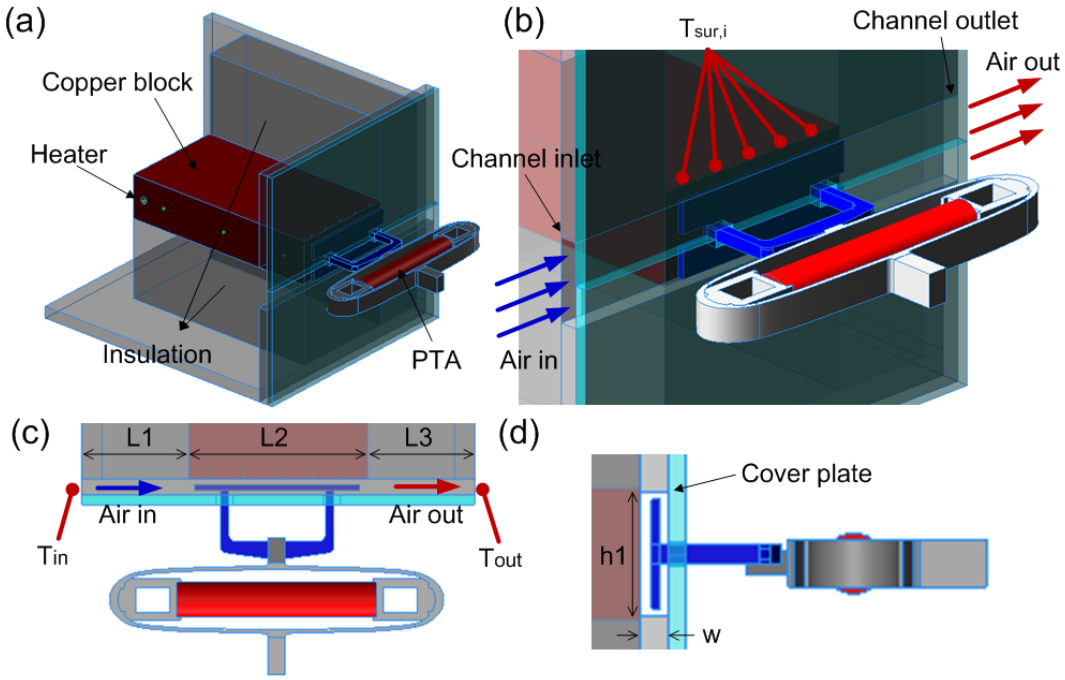

Figure 3.2: Schematic of the test section of the heat transfer experiment

More detailed illustrations of the heat transfer experiment test section are shown in Figure 3.2. Figure 3.2(a) shows the copper block surrounded by insulation and the position of the heater at one end of the block. The PTA is positioned facing the convection surface and frames supporting the carbon fiber blade inside the channel go through the transparent channel wall opposite to the heated surface. The holes for the supporting frames on the channel wall were completely sealed with flexible latex to make sure there is no air leakage to the channel through the holes. At the upstream and downstream edges of the heated area, there are adiabatic extended sections of the channel

to allow for the flow to become fully developed. Dimensions in Figure 3.2: channel height (h1), width (w), upstream length (L1), heated section length (L2), and downstream length (L3), are 20 mm, 4.3 mm, 32 mm, 50 mm, and 32 mm, respectively. Two thermocouples are used to measure air inlet temperature (T_{in}) at the channel entrance and one thermocouple is used to measure outlet temperature (T_{out}), as shown in Figure 3.2(c). Ten thermocouples, denoted as $T_{sub,i,}$ are used to measure temperatures 1mm into the copper block above the convection surface. From these temperatures, the surface temperature ($T_{sur,i}$) can be found by extrapolation to the convection surface, as follows:

$$T_{sur,i} = T_{sub,i} + \frac{q \cdot l}{k \cdot A_c} \tag{3.1}$$

where, q, l, k, and A_c express heat input from the heater, distance of thermocouples from the convection surface, copper thermal conductivity, and cross sectional area of the copper block, respectively. The average temperature of the exposed copper surface, T_{sur}, assumed to be isothermal, is computed as:

$$T_{sur} = \frac{\sum_{i=1}^{N} T_{sur,i}}{N}, \quad N = 10 \tag{3.2}$$

The manometer measures the static pressure drop (P_{static}) at the discharge adaptor in which the pressure tap is located. The static pressure is measured as:

$$P_{static} = 2zg \cdot (\rho_{water} - \rho_{air}) \tag{3.3}$$

where z, g, ρ_{water}, and ρ_{air} are manometer reading, standard gravity, water density, and air density, respectively. The reference pressure is the ambient (also the upstream stagnation pressure). The discharge adaptor at the outlet is connected to the blower through a

contraction section and a flexible hose. The pressure tap is located slightly downstream of this contraction section and, thus, is measuring the static pressure consistent with the velocity in that section. The total pressure at the exit (P_{total}) is:

$$P_{total} = P_{static} + \frac{1}{2}\rho V_{con}^2 \tag{3.4}$$

where V_{con} is the average velocity at the location of the pressure tap. In order to get the pressure loss (ΔP_{test}) across the heated section where the PTA operates, the total pressure losses of the inlet (ΔP_{inlet}), upstream (ΔP_{L1}), and downstream (ΔP_{L2}) were subtracted from the overall total pressure drop ($\Delta P_{total} = P_{ambient} - P_{total,eqn.\ (3.4)}$) as:

$$\Delta P_{test} = \Delta P_{total} - \Delta P_{inlet} - \Delta P_{L1} - \Delta P_{L2} \tag{3.5}$$

Each loss term can be calculated by using the equations shown as:

$$\begin{aligned} \Delta P_{inlet} &= K_{Loss,inlet} \cdot \frac{1}{2}\rho_{air} V_{in}^2 \\ \Delta P_{L1,L2} &= f \frac{L}{2D_h} \rho_{air} V_{L1,L2}^2 \end{aligned} \tag{3.6}$$

where $K_{loss,inlet}$ and f are the inlet loss factor and Darcy friction coefficients at sections L1 and L2, respectively. In addition, D_h, V_{in}, V_{L1}, and V_{L2} represent the hydraulic diameter of the channel, channel inlet velocity, velocity at section L1, and velocity at section L2, respectively. Heat transfer experimental results and measured pressure drops for each case are presented in the following sections.

3.2.2 Experimental Results

For the heat transfer experiments, four different channel flow rates of 10 LPM, 20 LPM, 40 LPM, and 60 LPM were used to investigate the effects of different channel flow

rates on heat transfer performance. The corresponding inlet average velocities and Reynolds numbers are listed in Table 3.1.

Table 3.1: Heat transfer experimental conditions with four different volume flow rates

Cross Flow Rate	**10 LPM**	**20 LPM**	**40 LPM**	**60 LPM**
Inlet Flow Velocity	1.94 m/s	3.88 m/s	7.75 m/s	11.63 m/s
Reynolds Number	823	1646	3293	4938

Upstream of the heated surface, the flow rates of 10 LPM and 20 LPM fall into the laminar regime, based on computed Reynolds numbers and transition criteria taken from the literature, all for a non-agitated channel. The other two flow rates fall in the turbulent regime. For all the test conditions, 5.3 W of heater input was supplied. The cooling performance of the PTAs was mainly investigated by calculating heat transfer coefficients using the Log Mean Temperature Difference (LMTD) method with the following equation:

$$h = q / A \cdot \Delta T_{LMTD} \tag{3.7}$$

where q, A, and ΔT_{LMTD} represent the heater input power, the heated surface area, and the log mean temperature difference, respectively. Herein, ΔT_{LMTD} can be computed by:

$$\begin{aligned} \Delta T_{LMTD} &= \frac{\Delta T_2 - \Delta T_1}{\ln(\Delta T_2 / \Delta T_1)}, \\ \Delta T_1 &= T_{sur} - T_{in}, \\ \Delta T_2 &= T_{sur} - T_{out} \end{aligned} \tag{3.8}$$

An uncertainty analysis was performed to estimate uncertainties in heat transfer coefficients. The heater input power, q, is known to 10% uncertainty according to the power supply manufacturer's manual. Temperature measurements carry a 0.5 °C uncertainty. The uncertainty for the convection area was ignored as it is very small

compared to the other terms. The total uncertainty of heat transfer coefficients propagated from each uncertainty listed above is 10 %. Thus, the total uncertainty is dominated by the uncertainty of the heater input power to the heater. The carbon fiber blade of the PTA is located in the center of the channel. Therefore, the clearance between the blade surface and the heated copper surface is 1.4 mm when the PTA is at the middle of its oscillation cycle. When PTA-1 operates at its maximum peak-to-peak displacement of 1.8 mm, the minimum clearance between the blade and the heated surface becomes 0.5 mm. Figure 3.3 present the comparison of heat transfer coefficients of four PTAs operating at different displacements and channel flow rates.

Overall, heat transfer coefficients increase with increasing displacement, frequency, and flow rate as anticipated. From Figure 3.3, the peak-to-peak displacement of 0 mm represents a condition in which the PTA does not operate. For PTA-1 and PTA-2, the heat transfer coefficients are almost the same when the displacement increases from 0 mm to 0.4 mm and the flow rates are in the upper range of 40 LPM and 60 LPM. This implies that the lower frequency of translational agitation below 700 Hz has no effect on heat transfer under this high channel flow velocity condition. On the other hand, there is slight enhancement of about 5% above the idle state condition in heat transfer coefficient when PTA-3 and PTA-4 operate with 0.4 mm displacement at flow rates of 40 LPM and 60 LPM. At the lower flow rates of 10 LPM and 20 LPM, all the PTAs provided great improvement in heat transfer coefficient once the PTAs are turned on with displacements of 0.4 mm peak-to-peak or larger.

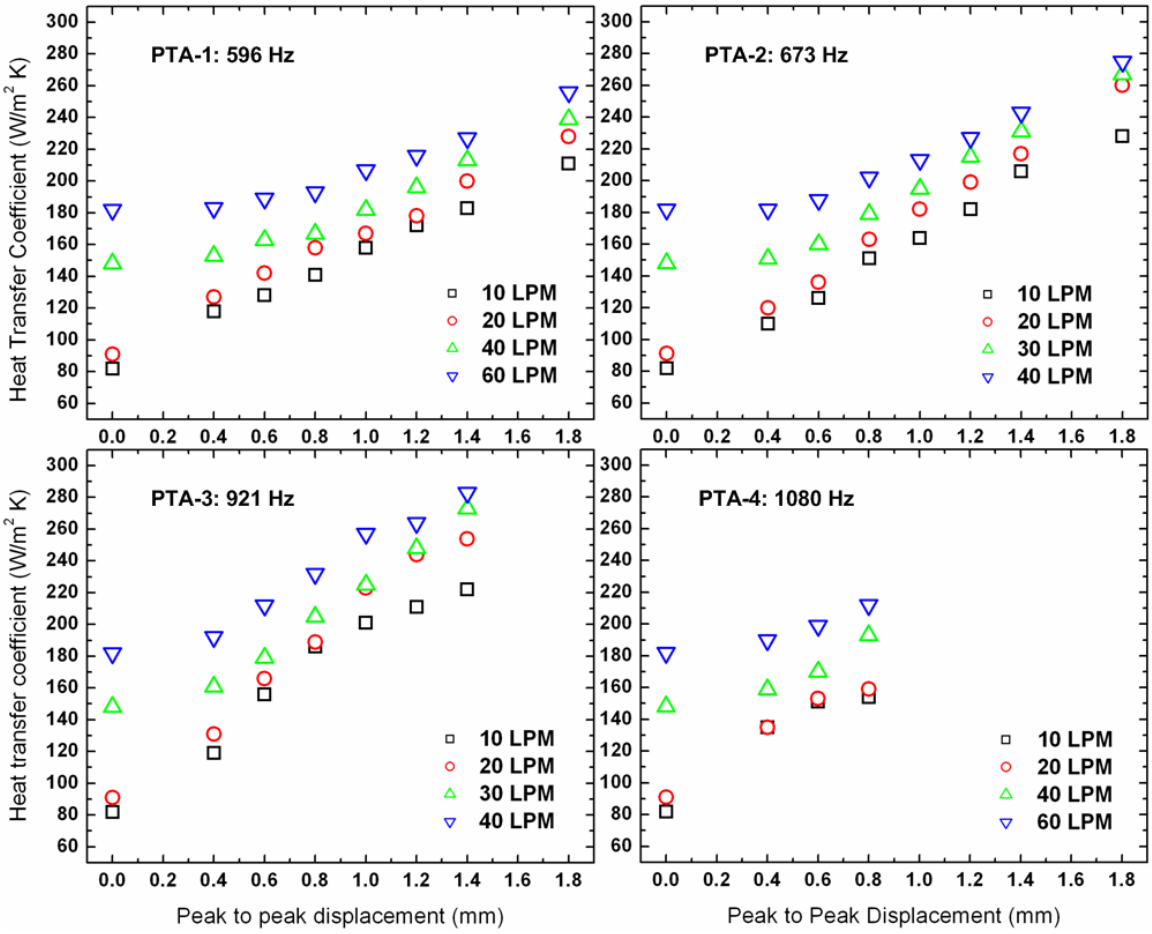

Figure 3.3: Heat transfer coefficient comparisons of four PTAs at different channel flow rates and peak-to-peak displacements

Considering 10% uncertainty in the heat transfer coefficient, one can say that PTA-1 and PTA-2 present almost equivalent cooling performance even though the performance of PTA-2 appears to be slightly better than PTA-1. Agitators PTA-1 and PTA-2 show the best heat transfer enhancement of 158% and 178% compared to no-agitation cases at the lowest flow rates of 10 LPM and with a peak-to-peak displacement of 1.8 mm. Agitator PTA-3 provided the best cooling performance among the four PTAs. The performance of PTA-4 cannot be compared with other cases in a fair way since its available displacement is limited at 0.8 mm. Agitator PTA-3 generated the largest heat

transfer coefficient enhancement, even with the smaller maximum displacement than those of PTA-1 and PTA-2. When PTA-3 operated with 1.4 mm peak-to-peak displacement, the heat transfer coefficient of 283 W/m² K was achieved under a channel flow of 60 LPM. This is a 55% improvement in heat transfer coefficient compared with the non-agitated state. In the laminar flow regimes, heat transfer augmentation by agitation is more significant than the agitation enhancement in the turbulent flow regime.

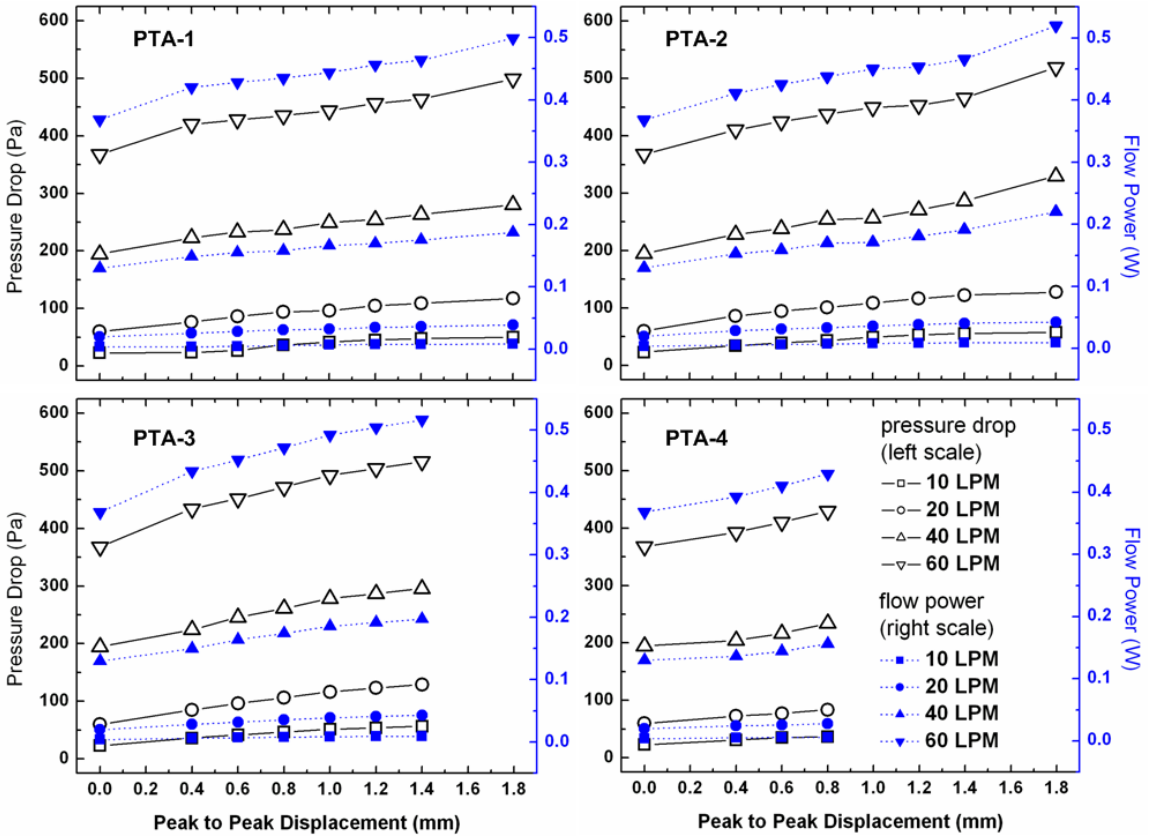

Figure 3.4: Pressure drop and corresponding flow power comparisons of the test section with the channel flow and agitator operated

When the PTA is idle, the pressure drop increases 1500% purely due to the raise of a flow rate from 10 LPM to 60 LPM. For all the PTAs, as the flow rate rises and the displacement remains unchanged, the increasing rate of pressure drop is similar to that

observed with channel flow-only. Similarly, the effect of increasing PTA displacement on pressure drop is insignificant, compared to the effect of the flow rate on pressure drop. Agitator PTA-2 showed the largest increase of pressure drop of 150% above the zero displacement case when the agitator is operated with 1.8 mm displacement at 10 LPM of flow rate. As the flow rate rises, increases of the pressure drop due to displacement decrease to around 40% at the 60 LPM flow rate. The pressure drop ranges between 20 Pa and 520 Pa, according to operating conditions of the PTA and channel flow rate. The flow power ranges between 0.003 W and 0.35 W under the various experimental conditions. The pressure drop and flow power presented here can provide an estimate of fan power needed when the translational agitator is coupled with the external fan to provide channel flow and agitation within the heat sink system.

In addition, PTA-1 and PTA-2 were tested with the channel ends open and without the flow forced by the fan, to study the sole performance of the PTA as a stand-alone cooling device. For the experiment, the cover plate in Figure 3.2(d) was removed to make the channel open to the ambient air. Then, the PTA is placed in the same position as it was in the channel flow tests. For the open channel test, the heat transfer coefficient of the heated surface was calculated as:

$$h = q / A \cdot (T_{sur} - T_{air}) \tag{3.9}$$

where T_{air} is the averaged ambient air temperature measured by three thermocouples adjacent to the heated surface area. Figure 3.5 compares the heat transfer coefficients of the heated surface cooled by PTA-1 and PTA-2 in the open channel to the cases of the PTAs and a cross flow of 10 LPM.

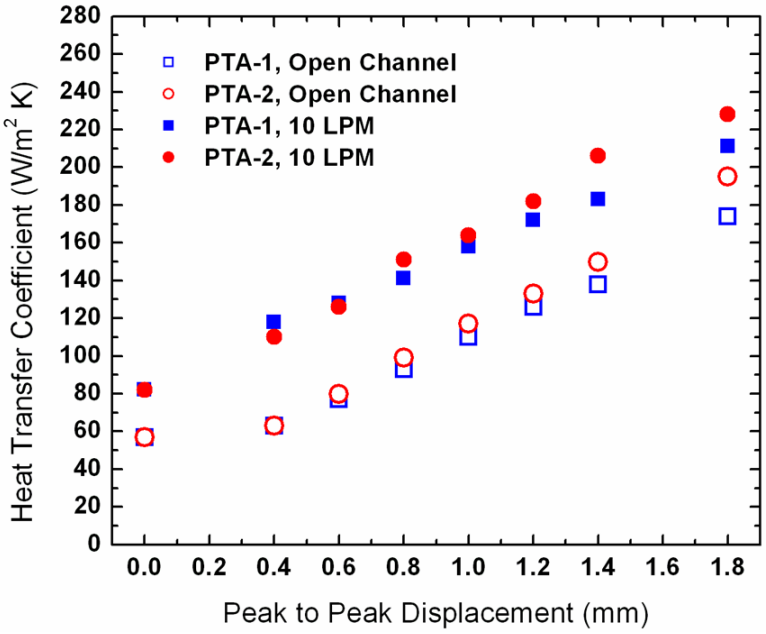

Figure 3.5: Heat transfer coefficient comparisons between the open channel and closed channel with the channel flow of 10 LPM for PTA-1 and PTA-2

In the open channel, the heat transfer coefficient at a displacement of 0.0 mm shows rather higher levels considering it is a natural convection condition. It is recorded that the ambient air currents were strong in the test room. Similar currents may be seen in a forced-air vented electronics cabinet. The results show that the PTA alone can provide fairly large cooling performance compared to those of the combined system of a PTA and channel flow. When PTA-1 and PTA-2 are operating at 1.8 mm of displacement in the open channel, 174 W/m² K and 195 W/m² K of heat transfer coefficients were achieved which are 83 % and 86 % of the heat transfer coefficients from the cases with PTAs and 10 LPM of channel flow.

3.3 Total Reynolds Number and Stanton Number Analysis

For more detailed analysis of the heat transfer experimental results, a total Reynolds number (Re_{tot}) was proposed to characterize the combined effects of the

translational agitation and channel flow. The channel flow Reynolds number (Re_c) is defined as:

$$Re_c = \frac{V_{in} D_h}{\nu} \tag{3.10}$$

where V_{in}, D_h and ν are the channel flow bulk velocity, hydraulic diameter of the channel, and the kinematic viscosity of air, respectively. The Reynolds number (Re_{pta}) for the PTA is defined with the maximum blade velocity and the hydraulic diameter of the blade as:

$$Re_{pta} = \frac{\omega A D_b}{\nu} \tag{3.11}$$

where ω, A, and D_b are the angular frequency in rad/sec, the maximum mean-to-peak displacement, and the hydraulic diameter of the blade, respectively. The blade hydraulic diameter is defined as:

$$D_b = 4P_b / A_b \tag{3.12}$$

where P_b and A_b are the perimeter (2L + 2H) and area ($L \times H$) of the blade, respectively. From the two Reynolds numbers shown above, the total Reynolds number can be defined with the second power relation as follows:

$$Re_{tot} = \sqrt{Re_c^2 + Re_{pta}^2} = \frac{\sqrt{(V_{in} D_h)^2 + (\omega A D_b)^2}}{\nu} \tag{3.13}$$

In Figure 3.6, the heat transfer coefficients of all the cases shown in Figure 3.3 were plotted with respect to this total Reynolds number.

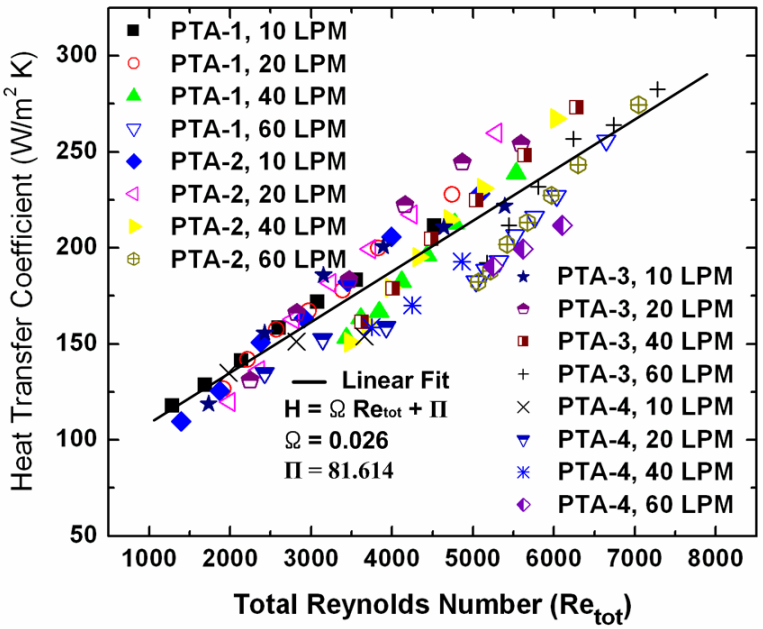

Figure 3.6: Heat transfer coefficients of all the experiment cases with respect to the total Reynolds number

The heat transfer coefficients are distributed in a linear relation with total Reynolds number, as displayed in the figure. From the relation, the expression for Nusselt number is derived:

$$\mathrm{Nu} = \frac{(h - \Pi)D_h}{k_{air}} = C\,\mathrm{Re}_{tot}\,\mathrm{Pr} \qquad \therefore C = \frac{\Omega}{\mathrm{Pr}} \cdot \frac{D_h}{k_f} \tag{3.14}$$

where k_{air} and Pr are the thermal conductivity and Prandtl number of air, assumed to be constant. The constants Π and Ω are calculated from the linear relation between the heat transfer coefficients and total Reynolds numbers (Figure 3.6). The Nusselt numbers are plotted with respect to total Reynolds number in Figure 3.7.

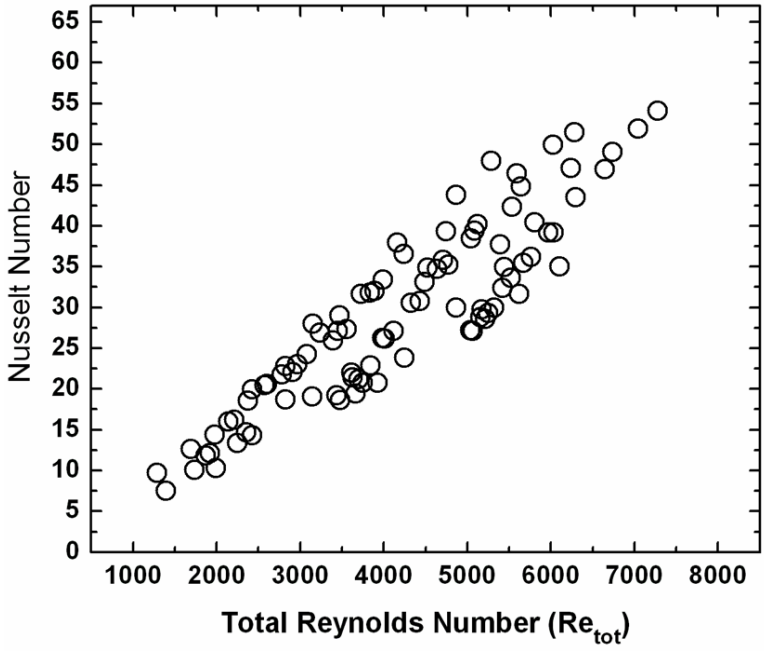

Figure 3.7: Measured Nusselt numbers vs. total Reynolds number

Equation (3.14) has a very familiar form with a relationship between Nusselt number, Reynolds number, and Prandtl number for convective heat transfer. By substituting Equation (3.13) into Equation (3.14) and writing Prandtl number as $\rho c\nu/k_f$, Equation (3.14) becomes as:

$$\frac{(h-\Pi)D_h}{k_f} = C\frac{\sqrt{(V_{in}D_h)^2+(\omega AD_b)^2}}{\nu}\cdot\frac{\rho c\nu}{k_f},\ (\because \mathrm{Pr}=\frac{\rho c\nu}{k_f}) \tag{3.15}$$

with the further arrangement, the equation becomes the form of Stanton number (St):

$$\mathrm{St} = \frac{(h-\Pi)}{\rho c\sqrt{(V_{in})^2+(\omega A)^2(\frac{D_b}{D_h})^2}} = C \tag{3.16}$$

which contains the effective velocity defined as:

$$V_{eff} = \sqrt{(V_{in})^2+(\omega A)^2(\frac{D_b}{D_h})^2} \tag{3.17}$$

From the Stanton number and the effective velocity defined above, it is possible to estimate the desired operating conditions of the PTA in terms of the operating frequency, peak-to-peak oscillating amplitude, and cross-flow rate based on the required cooling capacity. In Equation (3.16), the Stanton number is equivalent to the constant C. Therefore, the Stanton number or constant C could be directly calculated from the definition of C in Equation (3.14) and the value is 0.0099. The Stanton number could also be computed from Equation (3.16) with the effective velocity. Figure 3.8 presents the comparisons between these calculations for the Stanton number. The Stanton numbers calculated from the effective velocity showed an average error of 15.2 %.

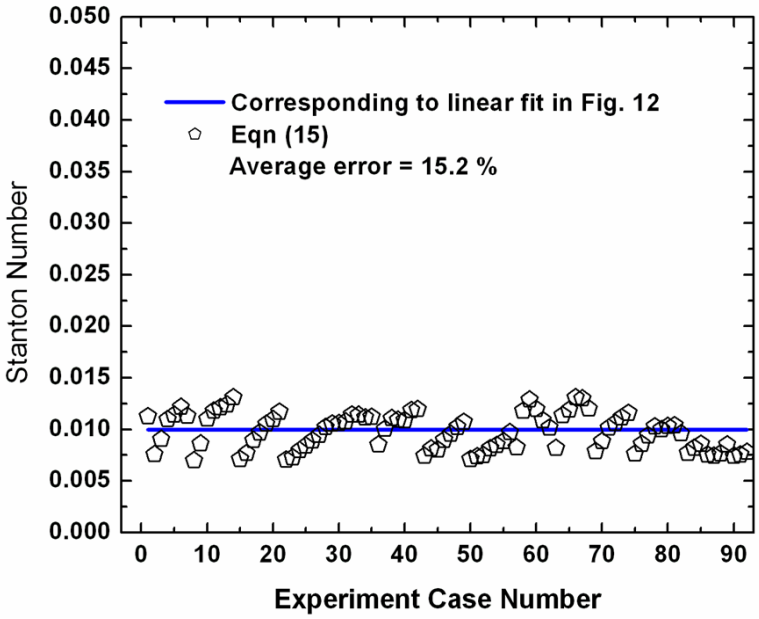

Figure 3.8: Stanton number data for the various cases

3.4 Coefficient of Performance (COP) of Single-Blade PTAs

The electrical power consumption of the PTAs was measured to investigate their feasibility as electronics cooling devices; results are shown in Figure 3.9.

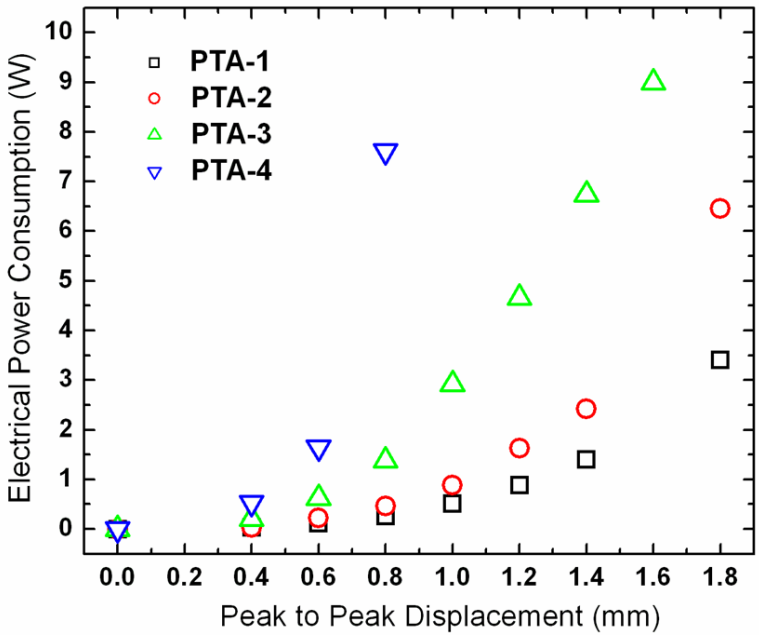

Figure 3.9: Electrical power consumption measurement of the PTAs

The actuator PTA-3, which provided the best cooling performance among the PTAs, consumes about 9 W when it is operating at 1.4 mm displacement at the second resonance mode. Additionally, the Coefficient of Performance (COP) values of the PTAs were defined as:

$$COP = \frac{q_{30-80}}{P_{in}} \tag{3.19}$$

where q_{30-80} is the heat transfer rate when channel inlet and convection surface temperatures ($T_{in=30}$ and $T_{sur=80}$) are assumed to be 30 °C and 80 °C, respectively. This is generally a desired operating condition of chips or CPUs in electronic devices. Therefore,

$q_{30\text{-}80}$ values are computed from the measured heat transfer coefficients at different operating conditions shown in Figure 3.3, assuming that inlet and surface temperatures are 30 °C and 80 °C, by the two methods shown below:

$$q_{30-80} = h \cdot A \frac{(T_{sur=80} - T_{in=30}) - (T_{sur=80} - T_{out})}{\ln\left(\frac{T_{sur=80} - T_{in=30}}{T_{sur=80} - T_{out}}\right)} \tag{3.20}$$

$$q_{30-80} = \rho_{air} Q \cdot c(T_{out} - T_{in=30}) \tag{3.21}$$

where Q, c, and T_{out} are volume flow rate, specific heat, and the outlet temperature when the inlet and surface temperatures are 30 °C and 80 °C, respectively. Herein, the outlet temperature, T_{out}, is unknown. From Equations (3.20) and (3.21), the outlet temperature (T_{out}) can be found as:

$$T_{out} = T_{sur=80} + (T_{in=30} - T_{sur=80}) \exp\left(-\frac{h \cdot A}{\rho_{air} Q \cdot c}\right) \tag{3.22}$$

Therefore, $q_{30\text{-}80}$ is calculated after substituting Equation (3.22) into either Equation (3.20) or (3.21). The power, P_{in} includes the electrical power input to the PTA (Figure 3.9) and flow power required to drive the flow through the test section (Figure 3.4). Figure 3.10 shows the calculated COPs in a log-scale with respect to the total Reynolds number defined previously.

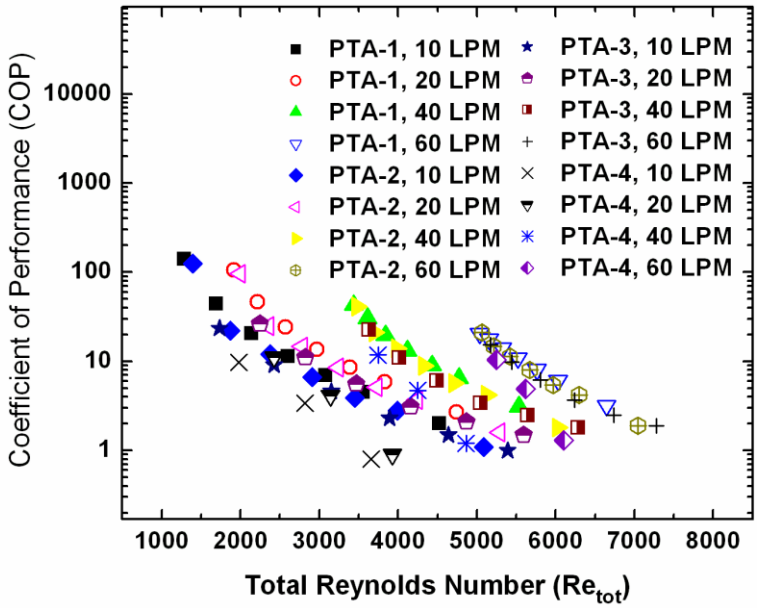

Figure 3.10: Coefficients of performance of PTAs with respect to the total Reynolds number at different operating conditions

Overall, COP tends to decrease with increasing total Reynolds number. The PTA with a lower operating frequency shows a higher COP at a fixed displacement and channel flow velocity. In addition, PTAs are more efficient at a lower channel flow velocity and smaller oscillation displacement. The COP analysis indicates that the PTA system is providing good cooling performance even at a less active operating condition with lower power consumption. This reflects a positive side in terms of the noise aspect as the PTA with a smaller displacement and lower frequency generates much less noise.

3.5 Conclusions

Four PTA designs were fabricated and tested in a single channel heat transfer facility. The operating frequencies of the four PTAs range from 596 Hz to 1080 Hz with amplified peak-to-peak displacements of up to 1.8 mm. The cooling performance of each PTAs was tested in a channel flow situation with one side heated and through-flow rates

of between 10 LPM and 60 LPM, representing laminar to turbulent flows. The best cooling performance was provided by a systems operated with 1.4 mm displacement and 60 LPM. This was a 55% improvement in heat transfer coefficient compared to the non-agitated state with the same channel flow. In addition, the pressure drop in the test section and the corresponding required flow power to drive the flow through the channel against the oscillating blade were measured. The pressure drop ranges between 20 Pa and 400 Pa according to the different operating conditions of the PTA and the rates of channel flow. The flow power ranges between 0.003 W and 0.274 W for different experimental conditions. The PTAs were also tested in the open channel to examine the sole effect of the PTA and to demonstrate the possibility of using it for stand-alone cooling.

It was shown that the proposed agitators with the single-blade carbon fiber structure demonstrated excellent capability to enhance the traditional fan-cooled heat sink or to operate as a stand-alone cooling device. For collapsing the data, a PTA Reynolds number and a total Reynolds number were defined to characterize the combined effects of cross flow and agitation. Measured heat transfer coefficients from all the test conditions were fit with a linear relationship in terms of total Reynolds number. This relationship gave a Stanton number that allows predicting the operating performance of the PTA-activated cooling module. Additionally, the coefficients of performance of the PTAs were presented.

Chapter 4:
Heat Transfer of Micro Pin-Fin Surfaces

4.1. Introduction

A pin fin array has been a popular method for increasing heat transfer area and convective heat transfer. Many application examples of the pin fins could be found in cooling turbine blades that experience extremely high temperature working conditions. In turbine blade cooling, the pin fin array augments convective heat transfer at the internal coolant passages of turbine blades in addition to the role of structural bridges between the two blade surfaces pressure and suction [99]. Another traditional application area of such pin fin arrays is in heat exchanger designs in which a flow passes among an array of cylinders. The pin fin arrays of earlier studies had relatively large geometric dimensions ranging over several millimeters in height, diameter, and pitch [99-107]. Sparrow and Ramsey [100] studied heat transfer and pressure drop characteristics of staggered array cylinders with tip clearances of various sizes. They measured mass transfer coefficients with the naphthalene sublimation technique and applied the analogy between mass transfer and heat transfer in order to get heat transfer coefficients for every individual row of the cylinder array. The working fluid was air. The results indicated that heat transfer was insensitive to cylinder height, while pressure drop increased significantly with increasing the cylinder height. Sparrow et al. [101] repeated similar experiments with an in-line pin fin array and compared the performance to the results of staggered pin fin array under the same conditions of pumping power and heat transfer area. Three different

tip clearances were introduced. They concluded that the fully developed heat transfer coefficients of the staggered pin fin arrays were higher than those of the in-line arrays. However, the in-line arrays showed smaller pressure drops over the staggered arrays. Metzger et al. [102] experimentally studied heat transfer and pressure drop aspects of staggered arrays of circular pin fins with a length-to-diameter ratio of unity. The tip clearance was zero in this case. With segmented construction of a test section, they were able to investigate locally resolved heat transfer coefficients for each row of the pin fin array. They noticed an initial rise of Nusselt number in the first three to five rows and a decrease in the downstream rows.

In the following studies, Metzger et al. [103] compared heat transfer and pressure drop performance of circular- and oblong-cross-section pin fins with various array orientations. The results revealed that the oblong pin fins increased heat transfer 20 %, but induced 100 % pressure drop increase over the circular pin fins. Peng [104] performed experiments with both staggered pin fins and full cross fins under air flow in a narrow rectangular channel to study the characteristics of heat transfer and friction factor. The test section simulated similar situation to a general turbine blade cooling passage. The results were presented in terms of the Colburn factor for heat transfer and friction coefficient for pressure drop. The results indicated that the pin fin configuration provided lower pressure drop while maintaining reasonably high heat transfer performance. In addition, the author concluded that pin fin pitch has less effect on heat transfer and friction loss than a pin fin height. Chyu [99] utilized the naphthalene sublimation technique to investigate pin-endwall fillet effects on heat transfer and pressure drop in

both staggered and in-line arrays. Similar to the results in the previous work [101], the staggered array generally produced larger heat transfer performance and larger pressure drop, compared to the in-line array. The other finding was that the endwall fillet diminished heat transfer for both staggered and in-line arrays.

Chyu et al. [105] evaluated heat transfer performance of cubic- and diamond-shape pin fins in both in-line and staggered arrays. The authors applied the naphthalene sublimation technique in order to get row-resolved heat transfer coefficients of pin fin arrays. The pin fins were positioned in a rectangular channel under air cross flow. Their results exhibited the pattern that a staggered array provided higher heat transfer than an in-line array. In addition, better heat transfer performance was found from a cubic element rather than a diamond element. Elliptic-shaped pin fins were investigated by Li et al. [106]. A tip clearance was not provided and air was utilized as a cross flow. The results showed that heat transfer of the elliptic pin fins was higher than that of the circular pin fins. However, pressure drop of the elliptic pin fins was lower compared to that of the circular pin fins. Moores and Joshi [108] studied the effects of tip clearance over micro pin-fin surfaces with a pin fin diameter of 400 μm and different height-to-diameter ratios. The working fluid was water. The tip clearance was up to 25 % of the pin height. The results showed that there existed an initial heat transfer increase at small tip but increasing clearances since the pin tips provided more heat transfer area. However, a further increase of tip clearance resulted in lower heat transfer than that of a back of pin fins due to bypassing of the flow through the tip clearance region.

As discussed so far, a considerable amount of experimental studies about conventional size pin fins have been accumulated with different pin shapes, array configurations, tip clearances, height-to-diameter ratios, diameter-to-pitch ratios, etc. and the data provided generally agreed. More recently, the advent of micro fabrication technologies has triggered size shrinking of pin fin structures to micro scales that could be utilized for cooling applications in compact spaces such as in electronics. Marques and Kelly [109] fabricated a flat micro pin-fin heat exchanger by directly electroplating Nickel using the LIGA micro fabrication process. The focused application was primarily for cooling gas turbine blades. The pin fin diameter and height were 500 μm, and there was no tip clearance. Their micro pin-fin structures achieved a 36% area increase, which led to 300 ~ 450% enhancement of heat transfer under a cross flow of air. They also demonstrated fabrication of more complex heat exchanger designs on a simple cylinder structure. Koşar et al. [110] studied hydrodynamic characteristics of micro pin fin arrays in both staggered and in-line configurations with a de-ionized water flow. The pin fin height was 100 μm with two pin fin diameters of 50 μm and 100 μm. Reynolds numbers between 5 and 128 were investigated. It was found that correlations of conventional size pin fins cannot estimate hydrodynamic performance of the micro pin fins correctly. Therefore, a modified correlation for the micro pin fins was proposed based on experimental results seen from the results that staggered array and diamond pin fins generated higher friction factors compared to those for an in-line array of circular pin fins. This trend matched well with the previous results of conventional-scale pin fin studies. Peles et al. [111] derived an analytic expression of a total thermal resistance model for a

bank of micro pin fins. The analytical results were experimentally validated. They concluded that densely packed pin fins are more adequate for high Reynolds number flows while sparse pin fins are suitable for low Reynolds number flows. Prasher et al. [112] performed extensive experiment studies with silicon-based staggered micro pin fin array under water flow. The micro pin fins were both circular and square shapes. The pin fin diameter ranged from 55 μm to 153 μm and the height-to-diameter ratio varied from 1.3 to 2.5. The results were compared in terms of the thermal performance parameter that represents the heat transfer per unit pumping power. Liu et al. [113] experimentally investigated heat transfer of square micro pin-fin heat sink with liquid cross flow. The square micro pin fins had dimensions of 559 μm × 445 μm with 3 mm height. No tip clearance was allowed. They concluded that heat transfer increased with the fin Reynolds number. They also noticed that the previous correlations in the literature for the conventional size pin fins had overpredicted heat transfer. They proposed new correlations of Nusselt number for their micro pin fins.

4.2 Objective of the Chapter

Most of the micro pin fins in the previous literature are shrouded-type micro pin fins that completely occupy narrow and small channels. A few micro pin fins in the literature are housed with small tip clearances, which are only small fractions of pin fin heights. In this chapter, we focus on thermal and frictional characteristics of micro pin fin arrays in a relatively large channel that provides a large tip clearance to the pin fin structures. This configuration is coming from the idea that micro pin fins could be applicable to the channel surfaces of the active heat sink. The active heat sink possesses a

large number of channels between each fins and cross flow generated by an external blower or a fan passes through these channels. It is truly apparent that numerous micro pin fins positioned on the surfaces of the heat sink would increase heat transfer area dramatically and could readily enhance cooling capability. Thus, heat transfer experiments with micro pin-fin surfaces are performed in a single channel facility without agitators installed. Totally, eleven configurations of staggered micro pin fin arrays were fabricated by electroplating copper onto a thin copper substrate. Heat transfer and pressure drop characteristics of such micro pin fin arrays with large tip clearances in an air-flow channel will be presented in the following sections.

4.3 Fabrication of Micro Pin-Fin Surfaces

Photolithographic techniques are suitable for high-aspect-ratio microstructures and high-volume batch production since they are faster than Electrical Discharge Machining (EDM), casting, extrusion, sintering, and machining techniques, etc. Recently, pin fin structures onto silicon substrates are attempted by the Deep Reactive Ion Etching (DRIE) process or using nickel plating LIGA processes [114, 115]. In the present work, the copper micro pin fins are developed on a copper substrate due to its high thermal conductivity and low cost. Therefore, the LIGA approach was utilized to construct copper micro pin fin plate samples. The fabrication process of the micro pin fins is shown in Figure 4.1. First, the copper substrate is cut as 4-inch silicon wafers to make the fabrication process easier. Then, the substrate is cleaned using acetone, methanol, isopropyl alcohol, potassium hydroxide (2% weight ratio) and sulfuric acid (10% weight ratio), respectively. As the next step, the protective layer of Ti is deposited on the copper

wafer after wafer cleaning (Figure 4.1(a)). A KMPR photoresist (MicroChem corp.) mold is developed on the copper substrate, as shown in Figure 4.1(b). Then, the Ti metal layer is etched with diluted hydrofluoric acid (Figure 4.1(c)). Micro pin fins are electroplated in copper plating bath. Finally, the KMPR photoresist is removed and the copper micro pin fin array is obtained, as shown in Figure 4.1(d). The SEM (Scanning Electron Microscope) image of fabricated micro pin fin array is shown in Figure 4.1(f).

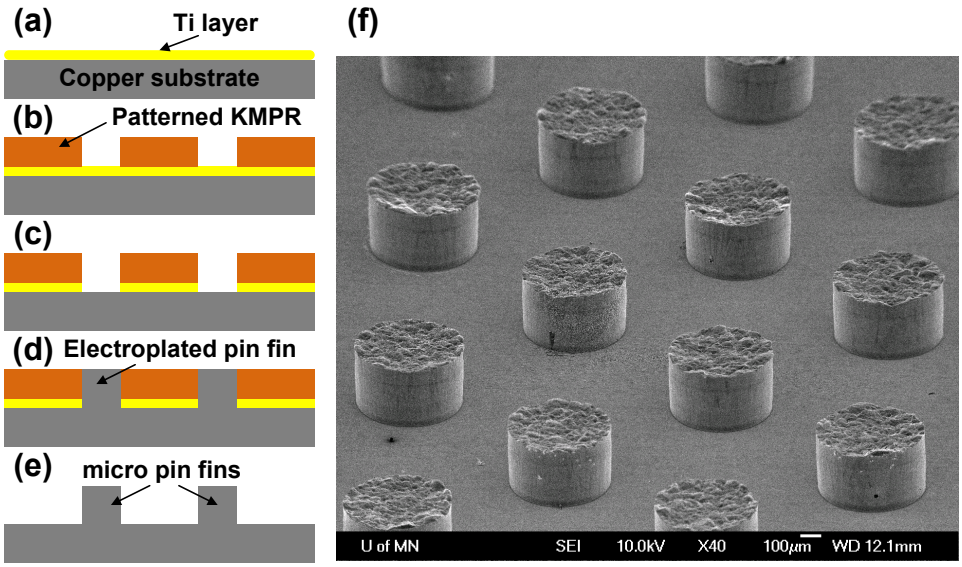

Figure 4.1: Fabrication process of the copper micro pin fin plate, (a) Ti metal layer deposition, (b) KMPR photoresist mold development, (c) Ti layer etching, (d) Copper pin fin electroplating, (e) KMPR photoresist removal, (f) SEM image of micro pin fin array

4.4 Heat Transfer and Pressure Drop Experiments

4.4.1 Experimental Set Up

An overall schematic of the heat transfer experiment for micro pin-fin surfaces is shown in Figure 4.2. The test facility is similar to the experimental set up for the single-blade PTA introduced in Chapter 3.

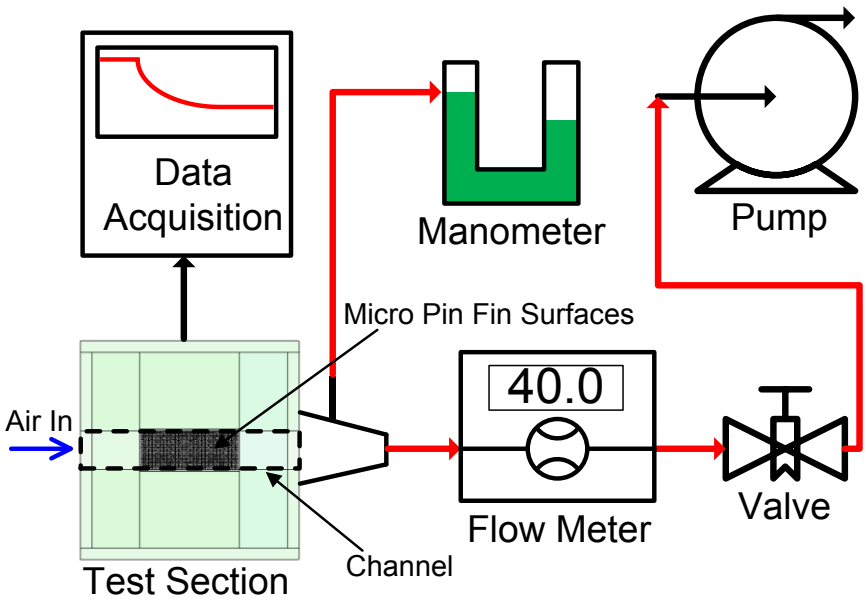

Figure 4.2: The diagram of heat transfer experiment facility loop

The test section is a narrow rectangular channel with a micro pin-fin surface housed in the center. An air flow is created by an external blower and enters from the left side of the channel. The test section was designed to simulate a portion of the active heat sink channel without agitators. At the outlet of the channel, a pressure tap is mounted at an adaptor that connects the channel to a pipeline and then to the blower. Pressure drop through the test section of the channel is measured with a u-shape manometer filled with dyed water. A volumetric flow meter and valve are positioned in sequence between the test section and the blower. All thermocouples and heater in the test section are connected to a data acquisition facility for data analysis. A detailed illustration of the test section is featured in Figure 4.3.

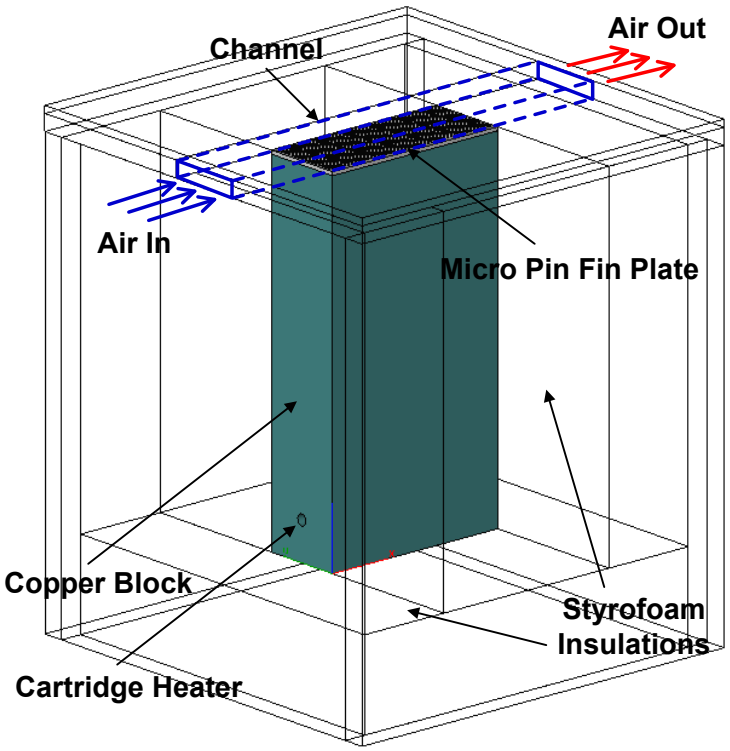

Figure 4.3: Test section of the heat transfer experiment

A long rectangular copper block is utilized to create a heat flow path from a heater to a convection surface. At the end of the copper block, a cartridge heater is inserted for providing heat input to the system. At the other side is attach a thin copper plate that has micro pin fins. Therefore, it is possible to easily switch micro pin-fin surfaces of different configurations for different experiments. The channel is created along the micro pin-fin surface with transparent plastic plates and has adiabatic extensions at the upstream and downstream to form fully-developed channel flow upstream of the micro pin-fin surface. All the other surfaces are enclosed by thick Styrofoam insulation to eliminate heat loss. Temperatures are measured 1 mm below the contact surface between the micro pin-fin plate and the copper block, as shown in Figure 4.4.

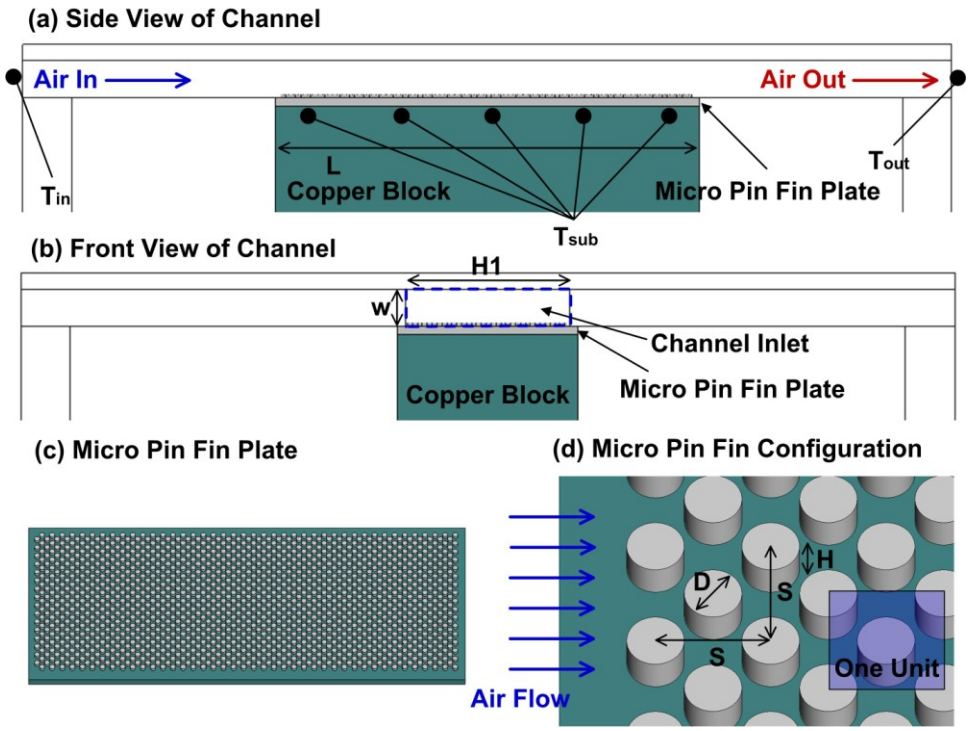

Figure 4.4: Configurations of the channel and micro pin fins

From these temperature measurements, surface temperatures of the micro pin-fin surface are found by extrapolation. A fin efficiency of the micro pin fins is assumed to be 100 % due to their micron size. Therefore, the base temperature of the micro pin-fin plate is used as surface temperature of the micro pin-fin surface. Two thermocouples measure flow inlet temperature and one thermocouple measures flow outlet temperature. Figures 4.4(a) and (b) show the side and front view of the channel, respectively. The micro pin-fin plate is attached to the copper block using thermal paste to minimize thermal contact resistance at the gap. The heated length (L), channel width (H1), and channel height (W) are 52 mm, 20 mm, and 4.3 mm, respectively. Figures 4.4(c) and (d) show the configuration of micro pin fins. The plate has a base thickness of 1mm. The eleven micro pin-fin surfaces were fabricated and tested. The entire micro pin-fin surfaces are

staggered array since thermal performance of the staggered array was shown to be superior to those of the in-line arrays in the literature [99, 101, 105, 110]. Dimensions in the figure, 'H', 'D', and 'S' are pin fin height, diameter, and pitch (both in horizontal and vertical directions), respectively. The dimensions of the micro pin fins are listed in Table 1 as well as porosity and area enhancement ratio over a plane surface. One unit of the pin fin array contains one fin in the center and four quarter fins at each corner of the square area with an edge length of 'S,' as shown in Figure 4.4(d). Herein, porosity (ξ) is defined as a ratio of pin fin occupied area to base area:

$$\xi = N_{mp}\pi(D/2)^2 / A_{base} \tag{4.1}$$

where, N_{mp} and A_{base} are the number of pin fins and the base area of the micro pin-fin plate, respectively. The number of pin fins on the plate is calculated as:

$$N_{mp} = 2(A_{base} / S^2) \tag{4.2}$$

Pin fin arrays are classified with different pin fin heights of 150 μm, 250 μm, 350 μm, and 400 μm. Each group has several pin fin diameters, as listed in Table 4.1. All the cases have the same S/D ratio of 3 except for the case of H150D75, which has a S/D ratio of 6. The area increase ratio is computed as:

$$\text{Area increase (\%)} = (N_{mp}\pi DH / A_{base}) \times 100 \tag{4.3}$$

Among the eleven samples, case H400D250 has the largest area increase ratio of 103.6% and the case of H150D75 has the smallest area increase ratio of 29.7%.

Table 4.1: Dimensions of micro pin fins

Micro Pin Fin	H (μm)	D (μm)	S (μm)	Tip Clearance (mm)	S/D	Porosity (%)	Area Increase (%)
H150D75	150	75	450	4.15	6	4.2	29.7
H150D150	150	150	450	4.15	3	16.8	63.3
H150D200	150	200	600	4.15	3	16.8	46.5
H250D250	250	250	750	4.05	3	16.8	63.3
H250D400	250	400	1200	4.05	3	16.8	38.1
H350D350	350	350	1050	3.95	3	16.8	63.3
H350D450	350	450	1350	3.95	3	16.8	48.4
H400D250	400	250	750	3.90	3	16.8	103.6
H400D400	400	400	1200	3.90	3	16.8	63.3
H400D600	400	600	1800	3.90	3	16.8	40.9
H400D700	400	700	2100	3.90	3	16.8	34.5

4.4.2 Data Reduction

Heat transfer experiments are performed with the micro pin fin plates and corresponding heat transfer coefficients and Nusselt numbers are presented to investigate the thermal performance of the micro pin-fin structures. Heat transfer coefficient (h) is computed with a Log Mean Temperature Difference (LMTD) method as below:

$$h = q / A \cdot \Delta T_{LMTD} \tag{4.4}$$

where q, A, and ΔT_{LMTD} represent heat from the cartridge heater, the convection surface area, and the log mean temperature difference, respectively. ΔT_{LMTD} can be computed from Equation (3.8). The surface temperatures ($T_{surface,i}$) are extrapolated from the temperatures ($T_{sub,i}$) measured at the slightly lower positions into the copper block under the micro pin fin plate. In addition, temperature drop at the interface between the copper block and the micro pin-fin plate due to the thermal contact resistance is compensated in the calculation. Therefore, the extrapolated surface temperature of the micro pin fin base is:

$$T_{surface,i} = T_{sub,i} - \frac{q}{A_c}\left(\frac{l}{k} + \frac{x}{k_p}\right) \tag{4.5}$$

where l_{sub}, x, k, k_p, and A_c are the distance between the micro pin-fin plate and temperature measuring position, the gap distance at the interface, copper thermal conductivity, thermal paste conductivity, and the cross sectional area of the copper block, respectively. Then, the extrapolated surface temperatures are averaged as below:

$$T_{sur} = \frac{\sum_{i=1}^{N} T_{sur,i}}{N}, \quad N = 10 \tag{4.6}$$

Accordingly, Nusselt number is calculated as:

$$Nu = hD_h / k_{air} \tag{4.7}$$

where D_h and k_{air} are the hydraulic diameter in the test section and thermal conductivity of air. A flow resistance study is performed by measuring a total pressure difference between the inlet and the outlet of the channel with a u-shape manometer filled with dyed water. A pressure tap is on the wall of an adaptor with a contracting flow passage area at the outlet of the channel. The pressure drop through the test section can be calculated by the same way done in the single-blade PTA tests through Equations (3.3) to (3.6) in Chapter 3.

Uncertainty analysis is performed on the heat transfer coefficients and pressure drop calculations based on propagation of uncertainties with constant confidence intervals. The cartridge heater utilizes alternating current (AC); time varying voltage and current are measured with an oscilloscope. The resistance of 0.2 Ω with 0.1% of error was set to measure the current through the heater. The oscilloscope has a measurement accuracy of 3% + 1mV. The corresponding uncertainty in power input is calculated as 4.4%. The convection surface area has 4% uncertainty and the uncertainty in temperature

measurements is set to 0.5 °C. As a result, the total uncertainty in heat transfer coefficient is 6.1%. For the pressure drop calculations, 2% of uncertainty is given to the reading of the manometer. The repeatability in pressure drop measurements is 6.2 %.

4.4.3 Heat Transfer Experimental Results

Heat transfer coefficients of the micro pin fin arrays under various cross flow rates are compared in four groups classified according to pin fin height. Two types of heat transfer coefficient are calculated from the base area (A_{base}) of the micro pin fin plates and actual increased heat transfer area (A_{actual}) due to the micro pin fins. The heat transfer coefficients calculated from the base area account for heat transfer enhancement due to both area increase and fluid dynamic effects, while the other counts only fluid dynamic effects. Figure 4.5 shows heat transfer coefficients for the group with a height of 150 μm.

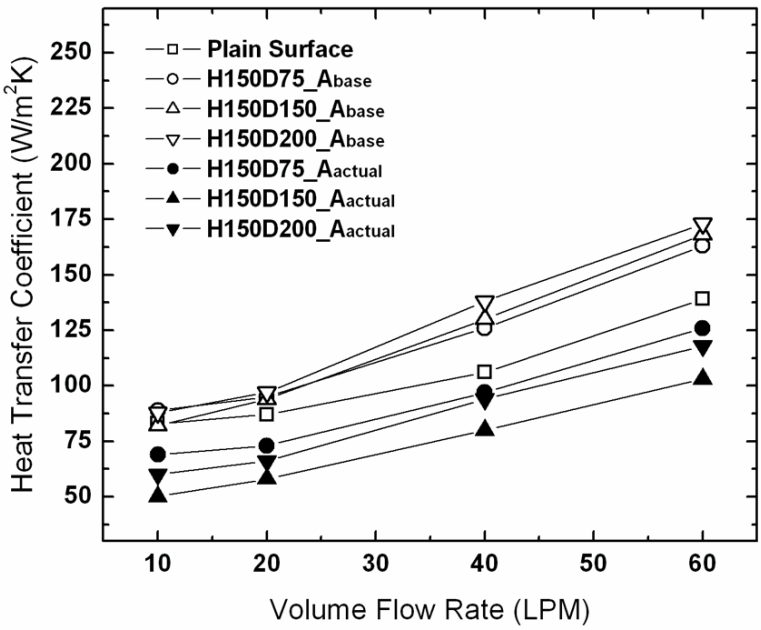

Figure 4.5: Heat transfer coefficient comparisons of micro pin fin arrays with the height of 150 μm and different fin diameters

It is confirmed that micro pin fins with larger diameters provide larger heat transfer rate at a fixed height when the coefficients are calculated based on the base area. The case of H150D200, which has the largest heat transfer among the three, based on the base area, generates the smallest heat transfer coefficient when it is based on increased area. On the other hand, H150D75, which has the smallest heat transfer coefficient based on the base area, has the largest increased-area based heat transfer rate. The result is that H150D75 generates the strongest fluid dynamic effects such as flow mixing and wall turbulence, but has the smallest area increase of only around 30%, resulting in lowest heat transfer rate among this group. The large heat transfer rate of H150D200 is mainly due to the area increase of around 63%. Overall, the group with a height of 150 μm shows 20 % heat transfer enhancement at higher cross flow rates of 40 and 60 LPM. Figure 4.6 presents the results of the group with a height of 250 μm.

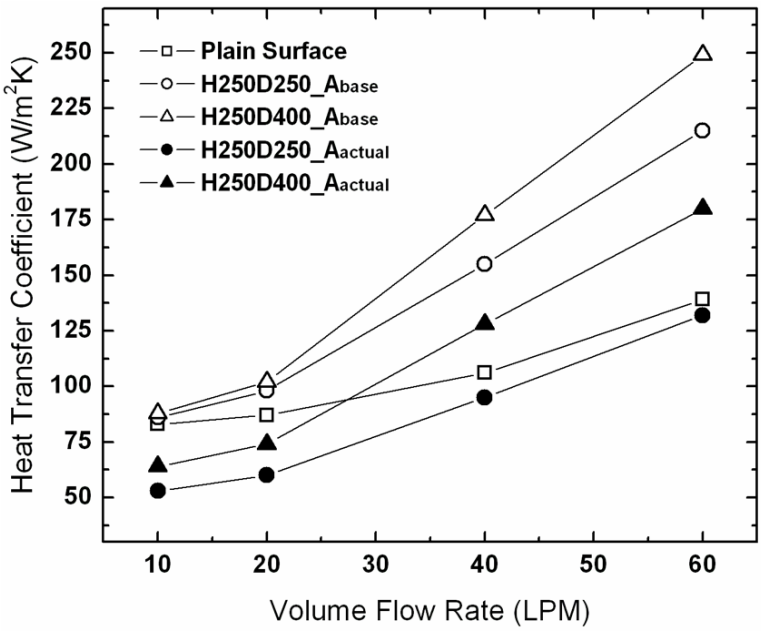

Figure 4.6: Heat transfer coefficient comparisons of micro pin fin arrays with the height of 250 μm and different fin diameters

In terms of the heat transfer coefficient based on the base area, a larger diameter gives larger heat transfer rates at all the cross flow rates even though area increase of H250D400 case is much smaller than the case of H250D250. This implies that fluid dynamic effects generated from the case of H250D400 overwhelm the area increase of H250D250 case. This could be confirmed again from the heat transfer coefficients based on increased area. The H250D400 case showed much larger heat transfer coefficients than H250D250. From the results, it is also notable that fluid dynamic effects for enhancing heat transfer performance becomes more dominant at higher cross flow rates. The case of H250D400 provides the most superior heat transfer performance among all eleven micro pin fin arrays when calculated based on the base area in spite of its small area increase rate of 38%. At a cross flow rate of 60 LPM, H250D400 enhances heat transfer coefficient by 79% over that of a plain surface. The heat transfer test results of the groups with pin fin heights of 350 μm and 400 μm are shown in Figures 4.7 and 4.8.

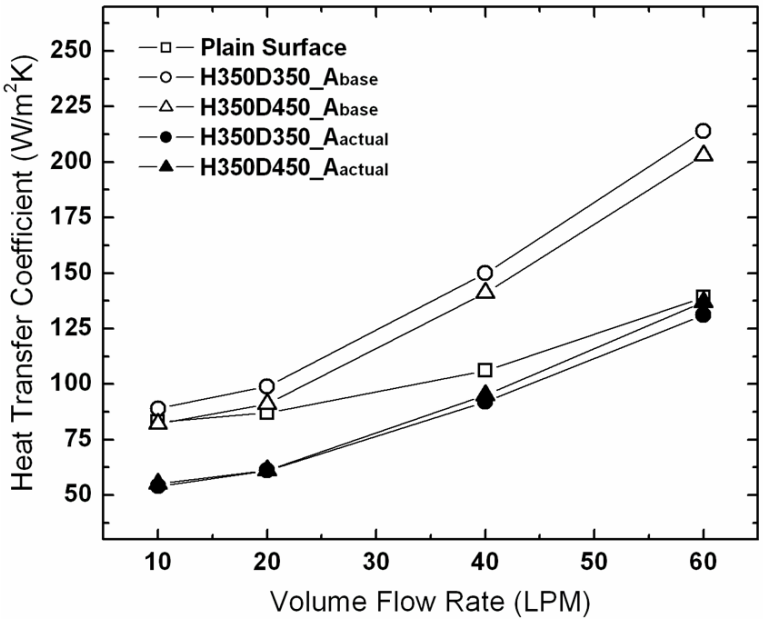

Figure 4.7: Heat transfer coefficient comparisons of micro pin fin arrays with the height of 350 μm and different fin diameters

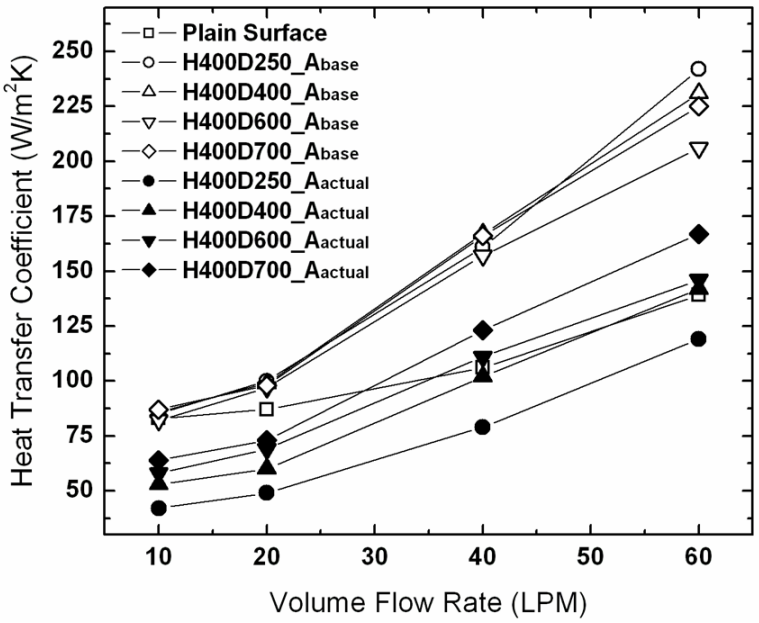

Figure 4.8: Heat transfer coefficient comparisons of micro pin fin arrays with the height of 400 μm and different fin diameters

The two cases in the group of 350 μm provide almost similar thermal performance as their diameter change is small compared to the pin fin height. The last group with a pin fin height of 400 μm has the widest range of diameter from 250 μm to 700 μm. Overall heat transfer performance computed using the base area suggests that all four cases showed comparable performance at all cross flow rates except for the 60 LPM cases, where the case with a diameter of 250 μm shows the largest improvement of 74%. This is slightly lower improvement compared to the case of H250D400. Unlike the similar overall heat transfer performances based on the base area, obvious deviations among the cases could be found from the heat transfer coefficients calculated based on actual increased area. The case of H400D250, which shows the greatest enhancement overall, has a smallest heat transfer coefficient based on the increased area, indicating that the major enhancement mechanism of this case is from area increase (103%) rather than fluid

dynamic effects. From the given heat transfer coefficient results so far, it is not easy to sort out a role of the pin fin height or pin fin diameter in terms of overall heat transfer. However, one apparent pattern could be found from the heat transfer coefficients based on the actual increased area (Figures 4.5, 4.6, 4.7, and 4.8) is that fluid dynamic effects for enhancing heat transfer performance increase with increasing pin fin diameter at a fixed height. One exception is found from the group with a height of 150 μm (Figure 4.5). The case of H150D75 showed the largest heat transfer coefficient based on actual increased area in spite of its smallest diameter among the group. However, this exception is acceptable as this case possesses a S/D ratio of 6 while all the other cases have a *S/D* ratio of 3. It is interesting to see that a larger S/D ratio and smaller porosity generates a stronger fluid dynamic effect for enhancing heat transfer performance.

4.4.4 Pressure drop and friction factor

Measured pressure drops over the micro pin fin arrays in the test section are shown in Figure 4.9 at different Reynolds numbers. Pressure drop differences between the micro pin fin arrays are small and even negligible at lower Reynolds number ranges below 2000, which represent the laminar flow regime. In spite of the small pressure drop differences, it is not difficult to find that the case of H400D250, which showed the largest heat transfer enhancement, generates the largest pressure drop among the eleven cases.

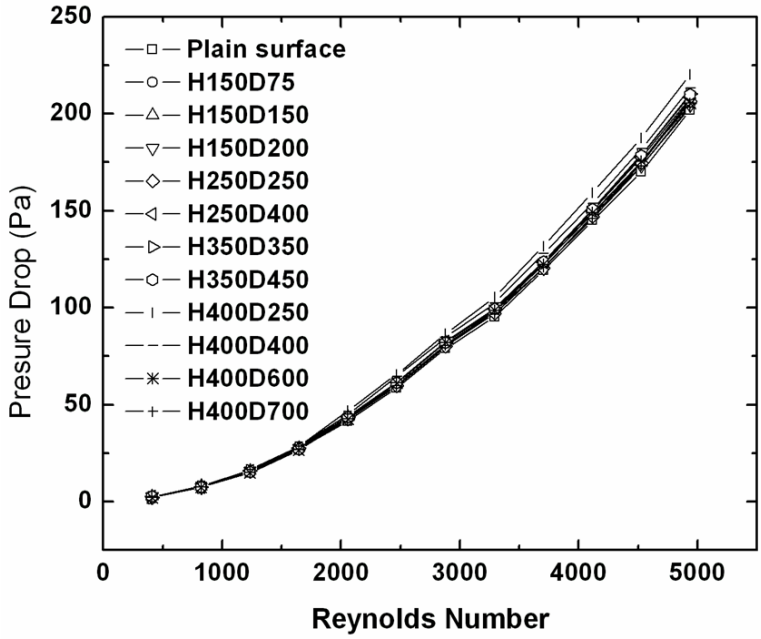

Figure 4.9: Pressure drops over micro pin fin arrays at different Reynolds numbers

More detailed comparisons of pressure drop at higher Reynolds numbers above 4000 are shown in Figure 4.10. Again, the results are classified into four different groups based on a pin fin height. At each group, pressure drop tends to increase with decreasing pin fin diameter except for the group with a pin fin height of 150 μm. This might have a relationship with the area increase for micro pin fin arrays, since a smaller pin fin diameter provides larger area increase at a fixed pin fin height and *S/D* ratio, as shown in Table 4.1.

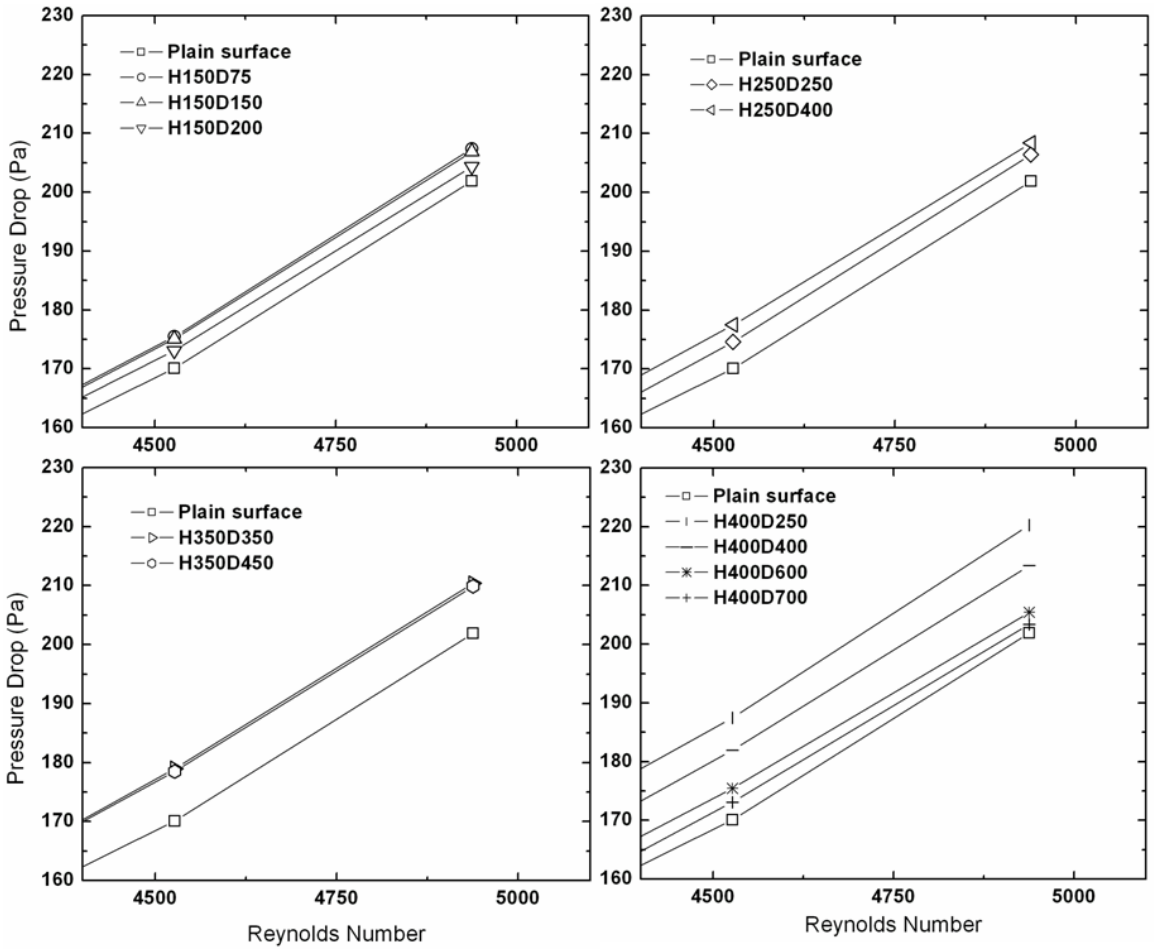

Figure 4.10: Pressure drops over micro pin fin arrays at high Reynolds numbers of above 4000

Figure 4.11 presents friction factors corresponding to pressure drops of each micro pin fin array and their results are compared with the well-known correlations of plain surfaces with different wall roughness. For the correlation of the laminar flow regime, f = 64/Re [116], which is independent of wall roughness, was utilized. Correlations for turbulent flow regime by Blasius and Haaland are given as [117]:

$$f = 0.316 Re^{-1/4} \quad , 4000 < Re < 10^5 \qquad \text{(Blasius)} \qquad (4.8)$$

$$f = 1/\sqrt{-1.8\log\left[\frac{6.9}{Re}+\left(\frac{\varepsilon/D_h}{3.7}\right)^{1.11}\right]} \qquad \text{(Haaland)} \qquad (4.9)$$

where ε represents an equivalent roughness height of a micro pin fin.

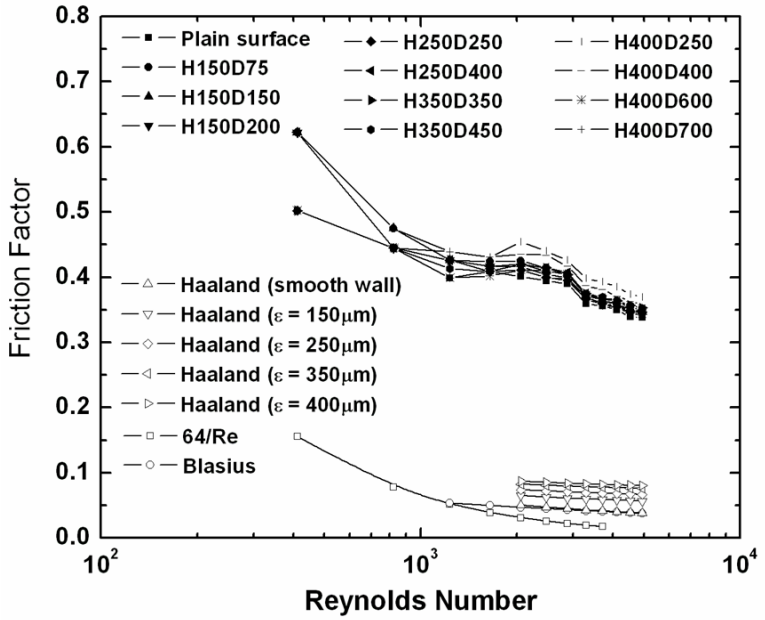

Figure 4.11: Friction factors of micro pin fin arrays at different Reynolds numbers

From Figure 4.11, one seems that the friction factors of the micro pin-fin surfaces in the current study, including the plain surface case, forms at relatively higher level compared to the correlations over the entire Reynolds number range tested. There might be uncounted factors in calculating pressure losses in the test section since it consists of several different parts and their interfaces are not smooth enough to be assumed as zero-pressure loss sections. This may have accounted for the deviation between the correlations and experimental results. However, the pattern for the friction factor of the current study along with Reynolds number matches well with the correlations. The Haaland correlation with different wall roughness heights suggests that the friction factor

is a function of pin fin height and is independent of pin fin diameter in the turbulent flow regime. The experimental results also provide a similar tendency that the higher micro pin fins exhibits larger friction factors in the turbulent flow regime as shown in Figure 4.12. However, it might be undeniable that a micro pin fin diameter also has an effect on the friction factor as some reversed friction factor curves are found from Figure 4.12.

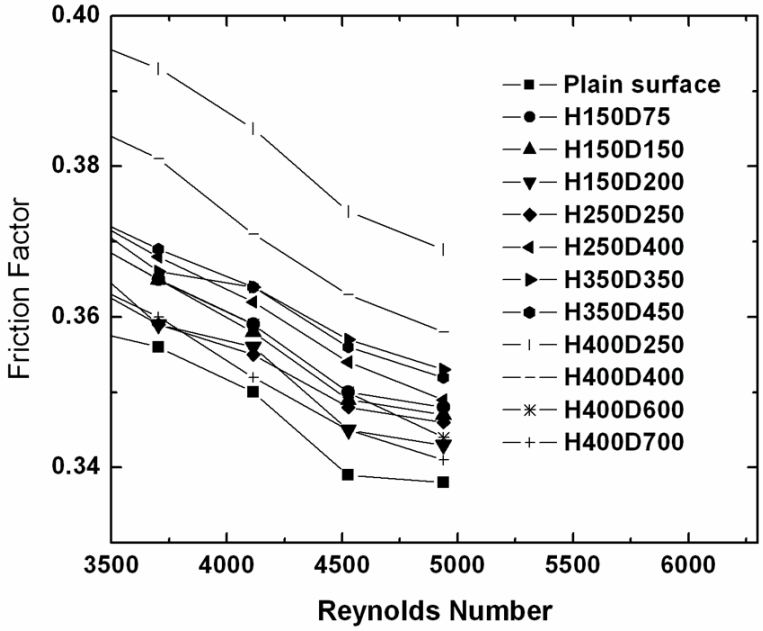

Figure 4.12: Friction factors of micro pin fin arrays at higher Reynolds numbers

4.5 Nusselt Number and Performance Index

Previous studies about micro pin fins presented various correlations for Nusselt numbers [108, 109, 112, 113]. Most of these cases are shrouded micro pin fins in micro channels that allow no clearance or very small clearances between tips of micro pin fins and channel walls. Therefore, the conditions resemble the well-known problem of flow across a bank of cylinders. On the other hand, the micro pin fin arrays in the current study are positioned in the channel with large tip clearances, which range from around ten

times to more than twenty times of pin fin heights. The large tip clearances allow the flow to bypass in the clearance area rather than go through the bank of micro pin fin. Therefore, it seems not reasonable to compare the results of the current study with the correlations for shrouded micro pin fins in the literature. Instead, we treat the micro pin fins as wall roughness in the channel, and thereby, the correlation by Norris [118] was used for Nusselt number estimation:

$$\frac{\mathrm{Nu}}{\mathrm{Nu}_{\mathrm{smooth}}} = \left(\frac{\mathrm{f}}{\mathrm{f}_{\mathrm{smooth}}} \right)^{\mathrm{n}} \tag{4.10}$$

where $n = 0.68Pr^{0.215}$. Figure 4.13 shows Nusselt numbers of each micro pin fin arrays compared to the Norris correlation with the friction factors calculated by the Haaland correlation at different micro pin fin heights. The results from the correlations advocate that the higher micro pin fin arrays generate larger Nusselt numbers. This tendency is corresponding to the experimental results with an exception that the case of H250D400 showed the largest Nusselt number among all the cases. This particular case might be the most desirable design of micro pin fin arrays in the current study. It increases fluid dynamic activities to create heat transfer augmentation. The Nusselt numbers from the correlations agree well with the experimental results and fall in a reasonable error range. The error becomes even less significant at the lower Reynolds numbers.

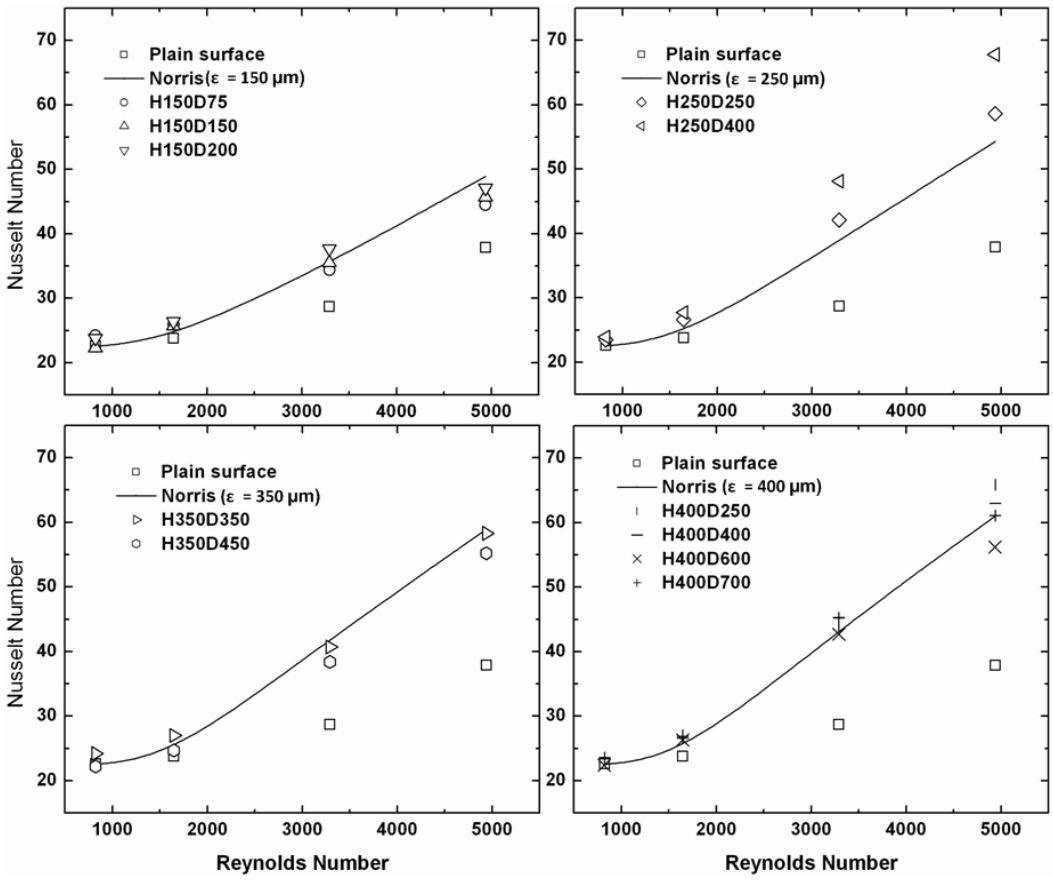

Figure 4.13: Nusselt numbers of micro pin fins compared to the correlations at different micro pin fin heights

Some literature introduced thermal performance ratio to judge performance of micro pin fins in terms of both pressure drop and heat transfer enhancement. Siw et al. [107], Marques and Kelly [109], and Prasher et al. [112] defined the performance ratio (PI) as:

$$PI = \frac{(Nu / Nu_p)}{(f / f_p)^{1/3}} \tag{4.11}$$

where subscript p represents plain surface. The calculated performance ratio of the micro pin fin arrays with the above definition are shown in Figure 4.14. According to the results,

the case of H400D250, which has the largest area increase, showed the best performance in terms of both heat transfer and friction aspects over all the flow rate range. In the mean time, Moores and Joshi [108] used a slight different definition of the performance ratio:

$$PI = \frac{(Nu / Nu_p)}{(f / f_p)} \tag{4.12}$$

This equation places more emphasis on friction factors than the former one does.

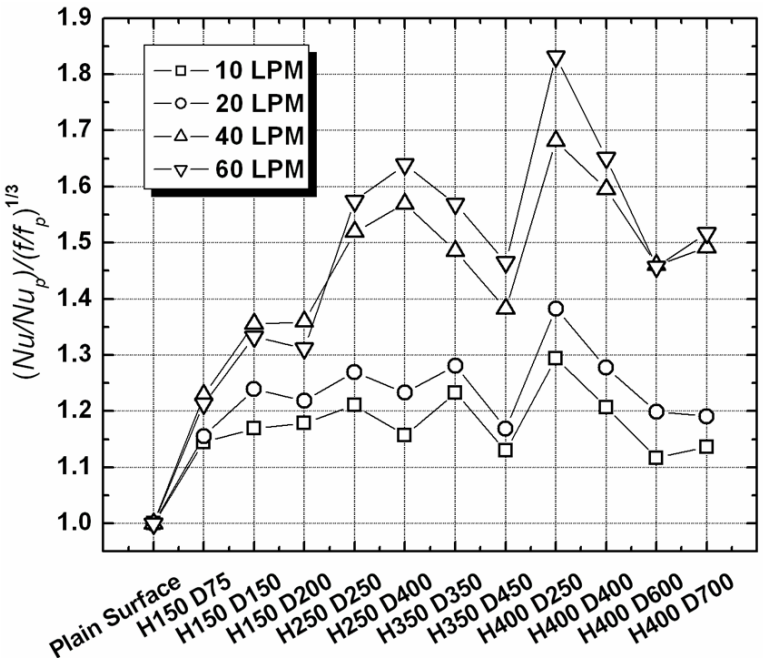

Figure 4.14: Performance ratios of micro pin fin arrays based on Equation (4.11)

The performance ratio of the micro pin fin arrays at different flow rates based upon the latter definition is presented in Figure 4.15 and the case of H250D400 showed the best performance. From the results of two performance ratio analyses, the case of H250D400 and H400D250 are shown to be the best configurations among the micro pin fin arrays of the present study. The former one is assumed to have the maximum fluid

behavior for augmenting heat transfer rate and the other one provides good performance mainly due to the largest surface area increase by the micro pin fins.

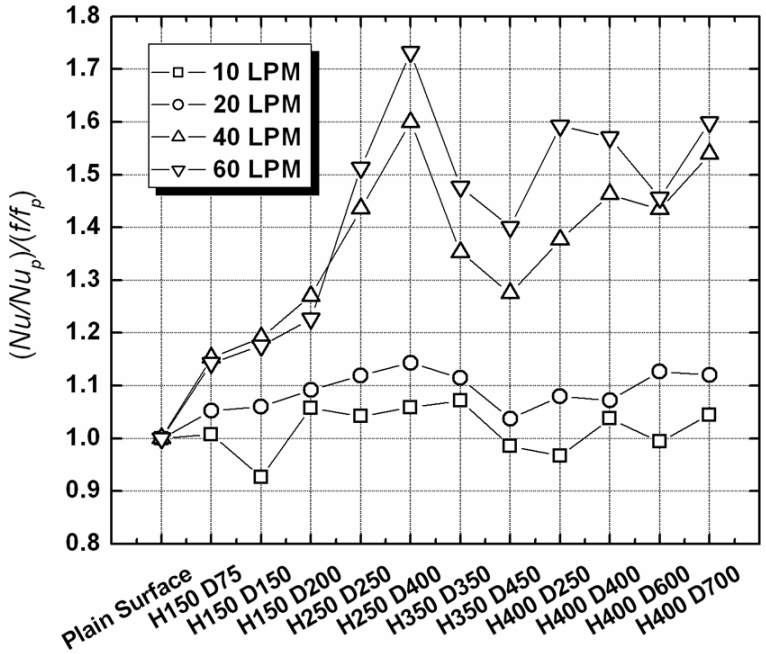

Figure 4.15: Performance ratios of micro pin fin arrays based on Equation (4.12)

4.6 Conclusions

In this chapter, heat transfer and pressure drop aspects of micro pin fin arrays in a rectangular channel with large tip clearances were studied experimentally. The copper micro pin fin arrays were fabricated on the copper substrate using LIGA photolithography process. Heat transfer experiments were conducted with different air cross flow rates. The summarized results of current study are given as:

- In the group with smaller micro pin fin heights of 150 μm and 250 μm, a larger diameter tends to provide higher heat transfer rate when the coefficients are calculated based on the base area.

- In the group with larger micro pin fin heights of 350 μm and 400 μm, the effect of diameter on heat transfer becomes less important.
- The maximum heat transfer enhancement of 79% is achieved from the micro pin fin arrays with a height of 250 μm and a diameter of 400 μm. Main contributions to the enhancement is fluid dynamic effects rather than area increase. The fluid dynamic effects to enhance heat transfer performance become more significant at higher Reynolds numbers.
- The case of H400D250, which has the largest area increase of 103%, shows the second highest heat transfer rate.
- The apparent pattern is found from the heat transfer coefficients based on the actual increased area of which the fluid dynamic effects for enhancing heat transfer become stronger with increasing pin fin diameter at a fixed height. This represents that a larger *S/D* ratio and smaller porosity generates a stronger fluid dynamic effect for enhancing heat transfer performance.
- Pressure drop tends to increase with decreasing pin fin diameter, since a smaller pin fin diameter provides larger friction area at a fixed pin fin height and *S/D* ratio.
- Nusselt numbers from experimental results are compared with the Norris correlations and show good agreement.
- Performance ratio analyses suggest that the cases of H250D400 and H400D250 are the best micro pin fin arrays of the current study in terms of both heat transfer and pressure drop aspects.

Chapter 5:
Translational Agitation over Micro Pin-Fin Surfaces

5.1 Objective of the Chapter

In this chapter, the advanced air cooling technique that combines both active and passive methods for developing an active heat sink system is investigated. Herein, the active method is a piezoelectric translational agitator that generates strong air currents from oscillating blade plates with high frequency translational displacements. The concept of the agitator with an oval loop shell piezo actuator was proposed and demonstrated in Chapter 2. In addition, Chapter 3 presented experimental studies on heat transfer performance of the piezoelectric translational agitator over plain heated surfaces in a channel with different operating conditions. The current chapter extends these previous studies and provides intensive heat transfer experimental results for the piezoelectric translational agitator operating over micro pin-fin surfaces. In addition, the thermal performance of the full-size active heat sink system aided by a multiple-blade agitator is anticipated, based on the results from single channel heat transfer experiments.

5.2 The PTA over micro pin-fin surfaces

In order to demonstrate thermal performance of the agitator and micro pin-fin surface combination for active heat sink technology, a single channel test section is considered as a first step. Figure 5.1 shows a conceptual illustration of the single channel test facility housed with the piezoelectric translational agitator and micro pin-fin surface.

In the center of the channel, the heated micro pin-fin plate is positioned and the agitator is operated over the micro pin-fin surface with high-frequency translational oscillation (expressed as white arrows in Figure 5.1). The micro pin-fin surface simulates one portion of the side surface of the active heat sink channel. Air flow enters from the left side of the channel and leaves to the right side of the channel. The micro pin fin has a diameter of D and a height of H as introduced in Chapter 4. The pitch between the pin fins is S and they are identical both in the horizontal and vertical directions. The detailed fabrication process of micro pin-fin plates is in the discussion of Figure 4.1.

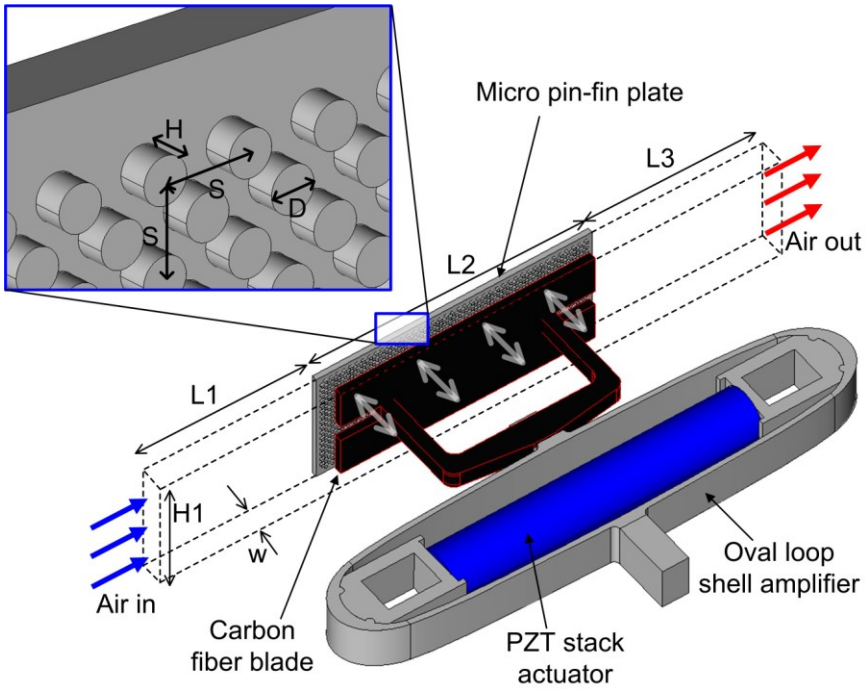

Figure 5.1: Illustration of translational agitator operating over micro pin-fin plate in a narrow channel

The same single channel test facility utilized for the experiments in Chapters 3 and 4 are used for the experiments in this chapter. A detailed test section of the heat transfer experiment is depicted in Figure 5.2. A long rectangular copper block is utilized as a heat

flow path to the micro pin-fin plate. At one end of the copper block, a cartridge heater is inserted. At the other end, the micro pin-fin plate is attached using thermal paste. The rest of the copper block is insulated with Styrofoam to prevent heat loss. The micro pin-fin surface is exposed to air flow in the channel, as shown in Figure 5.1. The channel is formed along the micro pin-fin surface with plastic plates. The channel has adiabatic extension sections (L1 and L2 in Figure 5.1) at the upstream and downstream. The agitator blade is positioned in the center of the channel and the frames that connect the blade to the oval loop shell pass through the holes in the plastic wall of the channel. The holes for the frames are sealed using flexible latex to ensure that there is no leakage.

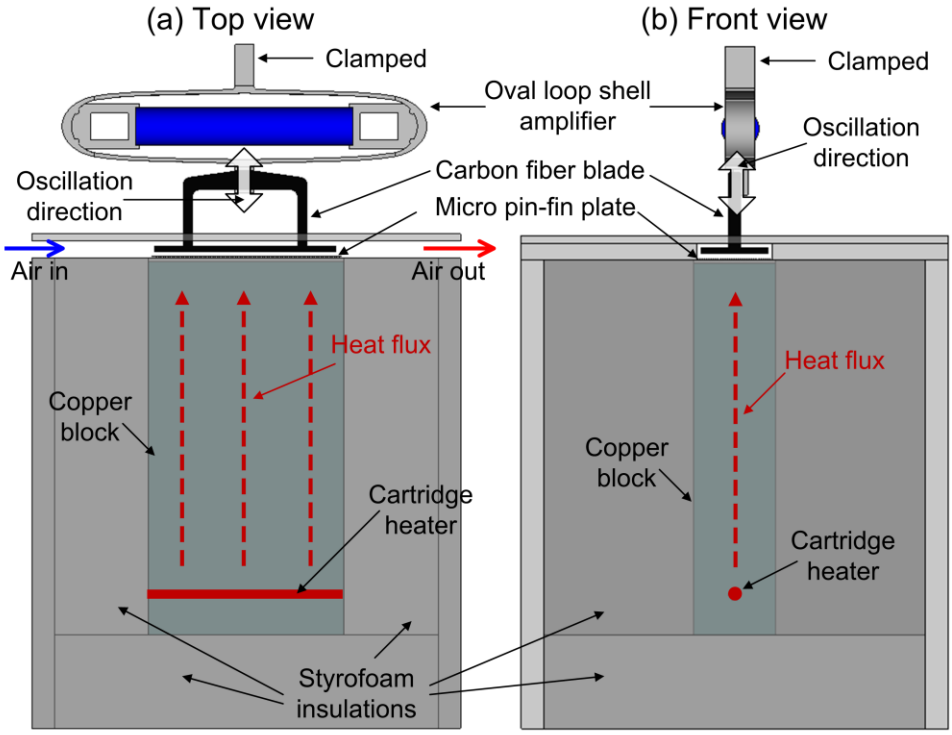

Figure 5.2: Test section of the single channel heat transfer experiment with micro pin-fin surface and PTA, (a) top view, (b) front view showing the inlet of the channel

The entire heat transfer experiment loop is described in Figure 5.3. An external

blower generates air flow through the channel. A flow meter and a valve to measure and control channel flow rate are positioned between the test section and the blower. A pressure tap is used at the outlet adapter of the channel and is connected to a manometer to measure pressure drop through the test section. A function generator and voltage amplifier provide an amplified sinusoidal voltage signal to the agitator.

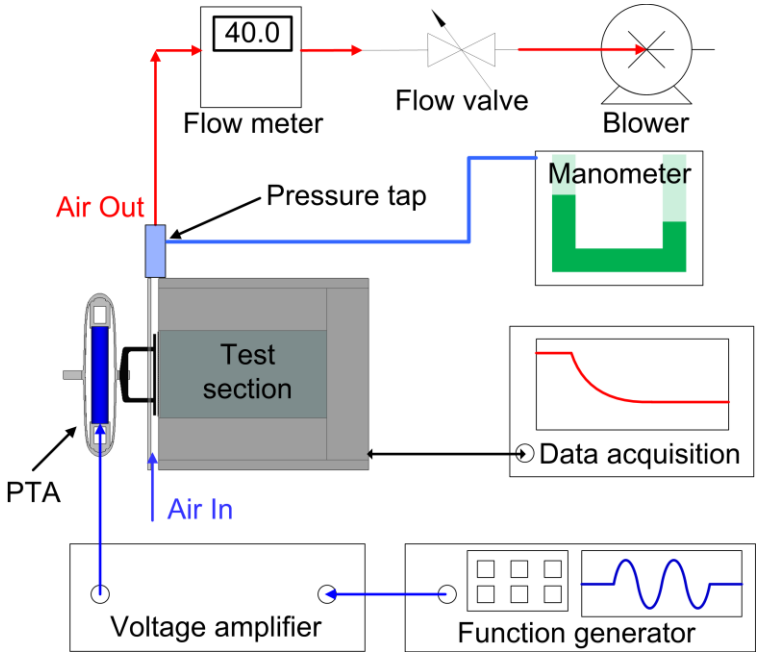

Figure 5.3: Schematic of single channel heat transfer experiment facility

5.3 Heat transfer and pressure drop experiments

5.3.1 Heat transfer experimental results

Heat transfer coefficients and Nusselt numbers are calculated to investigate the thermal performance of the micro pin-fin structures with and without the agitator. A detailed data reduction process is discussed in Chapter 3 between Equations (3.1) through (3.14). In Chapter 4, eleven micro pin-fin plates are fabricated and tested in a channel without an agitator. Dimensions and structural properties of eleven micro pin-fin plates

are listed in Table 4.1. The heights of the pin fins vary from 150 μm to 400 μm. The diameters change from 75 μm to 700 μm. For all the cases, the pitch, S, is kept as 3, except for the case H150D75, which has the pitch of 6. The case of H400D250 has the largest area increase of 103.6% among the eleven samples. In order to compare the overall performance of the micro pin-fin surfaces without agitation effects, the performance ratio is evaluated for the eleven micro pin-fin surfaces with Equations (4.11) and (4.12) in Chapter 4.

Figures 4.14 and 4.15 in Chapter 4 show the comparisons of performance ratios for the eleven micro pin-fin surfaces tested in the single channel test without the agitation. If the ratio is larger than 1, the heat transfer enhancement over the plain surface is greater than the pressure drop increase due to the micro pin-fin surfaces. The greater performance ratio represents the better performance of the micro pin-fin surfaces, considering both thermal enhancement and pressure drop aspects on an equal basis. As a result, the surface H400D250 showed the best performance among the eleven surfaces for all the channel flow rates tested and based on Equation (4.11). It is selected for the experiment in this chapter. However, the surface of H400D250 is not necessarily the best sample under the agitation effects. Therefore, surface H250D400, which showed the best performance based on Equation (4.12) is also selected for the experiments with the agitator.

The heat transfer experiments of the selected micro pin-fin surfaces are performed with the PTAs operating at two different frequencies, 596 and 920 Hz. Heat transfer coefficients of the micro pin-fin surfaces under the agitation effect at channel flow rates

of 10, 20, 40, 60 LPM are shown in Figures 5.4, 5.5, 5.6, and 5.7, respectively. The detailed channel flow conditions are listed in Table 5.1.

Table 5.1: Channel flow conditions of single channel heat transfer experiments

Cross flow rate	10 LPM	20 LPM	40 LPM	60 LPM
Velocity at inlet (m/s)	1.9	3.9	7.8	11.6
Velocity at test section (m/s)	2.8	5.7	11.3	16.9
Reynolds number (inlet)	823	1646	3293	4938

The PTAs operate at different peak-to-peak displacements between 0.4 mm and 1.4 mm with an increase of 0.2 mm according to different applied voltages to the PZT stack. At a channel flow rate of 10 LPM (Figure 5.4), a heat transfer coefficient of around 80 W/m^2 K is achieved from the plain surface.

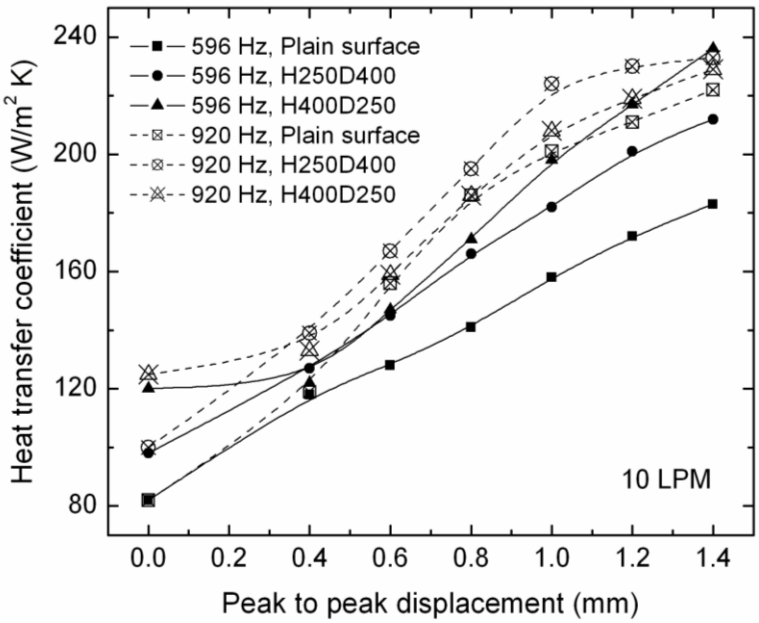

Figure 5.4: Heat transfer coefficients of micro pin-fin surfaces under translational agitations at a channel flow rate of 10 LPM

The micro pin-fin surface of H250D400 increased a heat transfer coefficient by 20 % up to around 100 W/m^2 K when the agitators are not operated. When there is no

agitation applied, the surface of H400D250 provided obviously better thermal performance over the case of H250D400. Once the agitators are turned on, the effects of translational agitation are clearly seen from all the surfaces. At a lower operating frequency of 596 Hz, two micro pin-fin surfaces gives similar performance at a displacement of 0.4 mm. At a frequency of 920 Hz, the surface H250D400 shows higher heat transfer coefficients at the entire displacement range. However, this falls within an uncertainty of 6.1 %. At a lower cross flow rate of 10 LPM, the two micro pin-fin surfaces show similar heat transfer performance when agitation effects are present. Once the peak-to-peak displacement reaches 1.4 mm, the micro pin-fin surfaces do not have a noticeable benefit over the plain surface at the higher frequency of 920 Hz. Overall, at a flow rate of 10 LPM, the micro pin-fin surface with the translational agitation improved heat transfer coefficient up to around 236 W/m^2 K, by 180 % over the non-agitated plain surface.

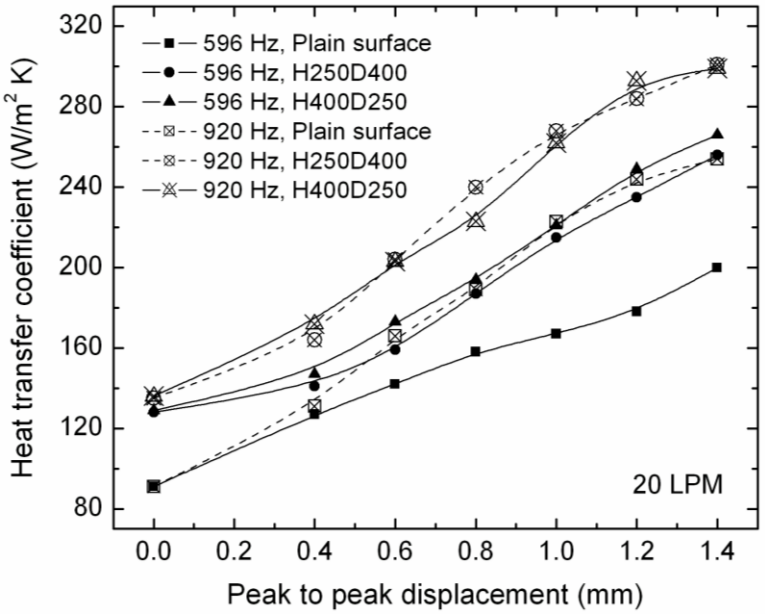

Figure 5.5: Heat transfer coefficients of micro pin-fin surfaces under translational agitations at a channel flow rate of 20 LPM

When the flow rate is increased to 20 LPM, similar patterns are found; Figure 5.5. The micro pin-fin surfaces provide obvious improvement in heat transfer compared to the plain surface. However, it is hard to distinguish the difference in thermal performance between the two micro pin-fin surfaces under the agitation effects. On the other hand, as the flow rate increases to 40 LPM (Figure 5.6), the surface of H400D250 starts to show better thermal performance over the H250D400 surface. At a frequency of 596 Hz, the H400D250 surface keeps superiority throughout the entire range of displacement values. However, at a higher frequency of 920 Hz, as the displacement increases the differences between the two micro pin-fin surfaces' performances becomes negligible.

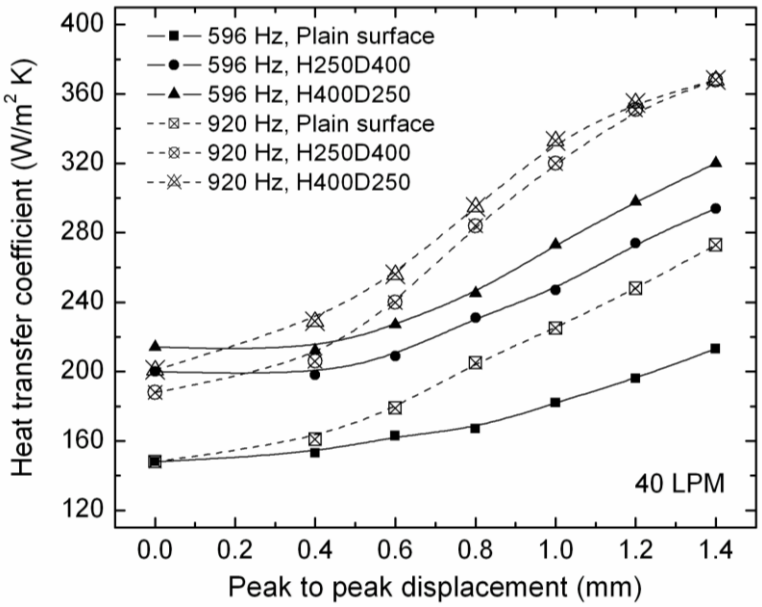

Figure 5.6: Heat transfer coefficients of micro pin-fin surfaces under translational agitations at a channel flow rate of 40 LPM

Overall, higher frequency agitation gives more heat transfer with a micro pin-fin surface of H400D250 at 40 LPM. A heat transfer coefficient of 368 W/m^2 K is achieved from the micro pin-fin surface of H400D250 cooled by 920 Hz agitation at a peak-to-

peak displacement of 1.4 mm and this is about 150 % improvement in heat transfer over the non-agitated plain surface at 40 LPM. At a highest flow rate of 60 LPM, the effects of micro pin-fin surfaces and translational agitation becomes more lucid, as shown in Figure 5.7. The heat transfer enhancement rate due to the micro pin-fin surfaces is larger than those of the lower flow rate cases. Among the two micro pin-fin surfaces, H400D250 shows better performance for all the operating conditions. The translational agitation at 920 Hz increases the heat transfer coefficient of the surface H400D250 up to 422 W/m^2 K. This is about 130 % improvement in heat transfer over the non-agitated plain surface at 60 LPM. From the heat transfer test results done at different operating conditions, it is noted that the micro pin-fin surfaces and agitators perform better at a higher channel flow rate in terms of heat transfer enhancement.

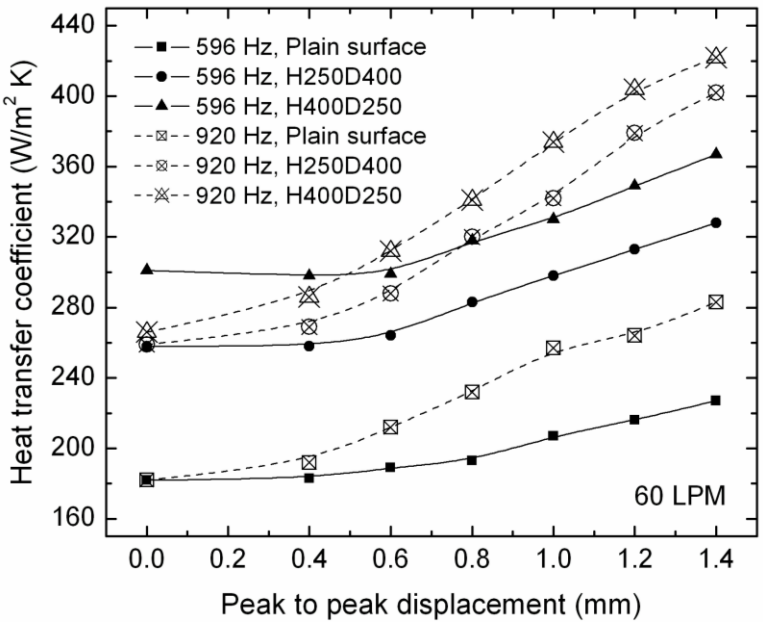

Figure 5.7: Heat transfer coefficients of micro pin-fin surfaces under translational agitations at a channel flow rate of 60 LPM

Figures 5.8, 5.9, and 5.10 present the heat transfer coefficients with respect to the product of displacement and frequency of the agitator at different channel flow rates. The product equals the peak velocity of the oscillating blade. Therefore, these thermal performance comparisons enable us to evaluate the relative importance of displacement and operating frequency of the agitator. If the agitator with a higher operating frequency provides better performance than the lower frequency agitator at the same peak velocity, frequency has a larger effect than that of displacement. Figure 5.8 shows the results over the plain surface. It shows the tendency that the agitator with a higher operating frequency of 920 Hz provides larger heat transfer rates than the lower frequency agitator over almost the entire range of peak velocity.

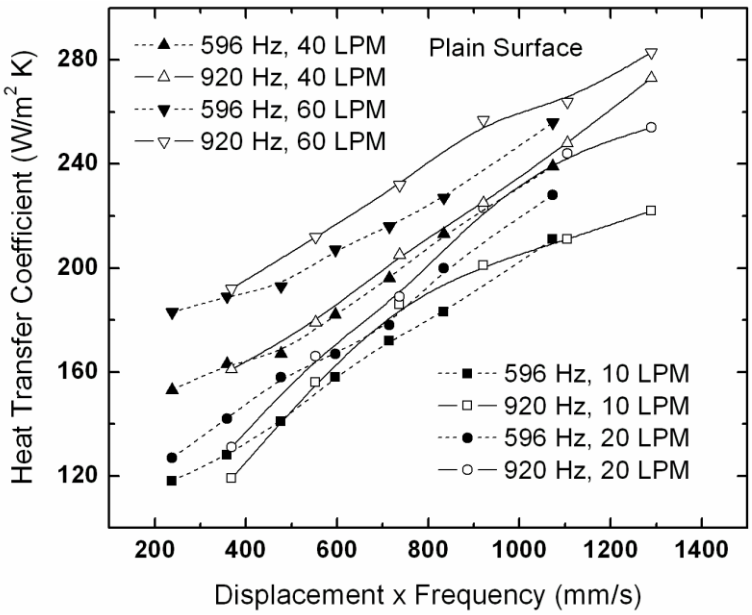

Figure 5.8: Heat transfer coefficients of plain surface with respect to the peak velocities of the agitators

This indicates that the operating frequency is more important than the displacement for the plain surface, though the difference is not quite distinguishable over

certain ranges of frequencies. In this case, agitation from the blade could easily reach the surface regardless of oscillation size since there are no micro pin fins, which possibly play the role as obstacles. On the other hand, if there are micro pin fins employed on the surface, an effect of displacement starts to develop. The results in Figures 5.9 and 5.10 support this. From Figure 5.9, two agitators with different operating frequencies over the micro pin-finned surface of H250D400 provide nicely matched heat transfer coefficients with respect to peak velocity. A larger displacement of oscillation has more of a chance to push the flow through the forest of micro pin fins. This phenomenon becomes even clearer over the micro pin-fin surface of H400D250.

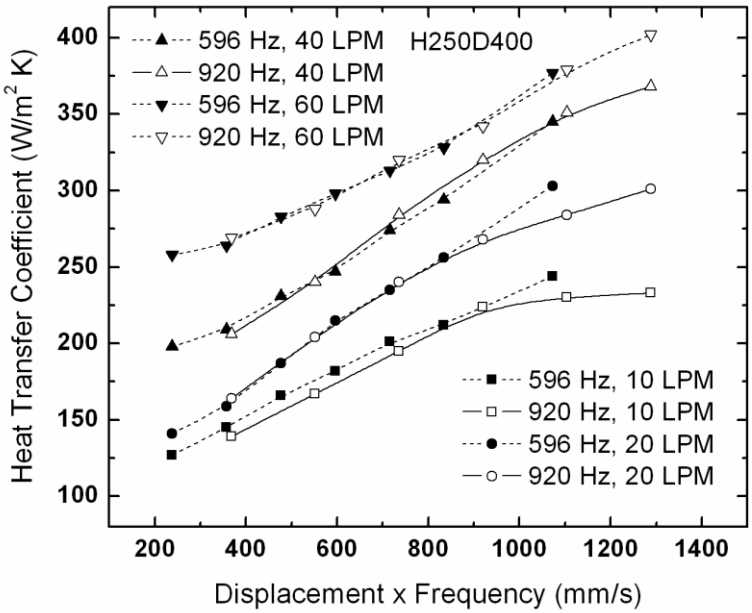

Figure 5.9: Heat transfer coefficients of micro pin-fin surface, H250D400, with respect to the peak velocities of the agitators

Figure 5.10 shows that the heat transfer coefficients of the lower frequency agitator are larger than those of the higher frequency agitator. Over the micro pin-fin surface H400D250, displacement has a stronger effect on heat transfer than frequency.

This is mainly due to the effect of the clearance between the tips of the micro pin fins and the blade. The agitator maximum stroke decreases as the pin fin height increases. As the clearance decreases, a larger oscillating displacement can push more air to the micro pin fins and this overwhelms the frequency effect. From the results, it is easy to notice that relatively larger importance shifted from frequency to displacement as the micro pin fins are used and their heights are increased.

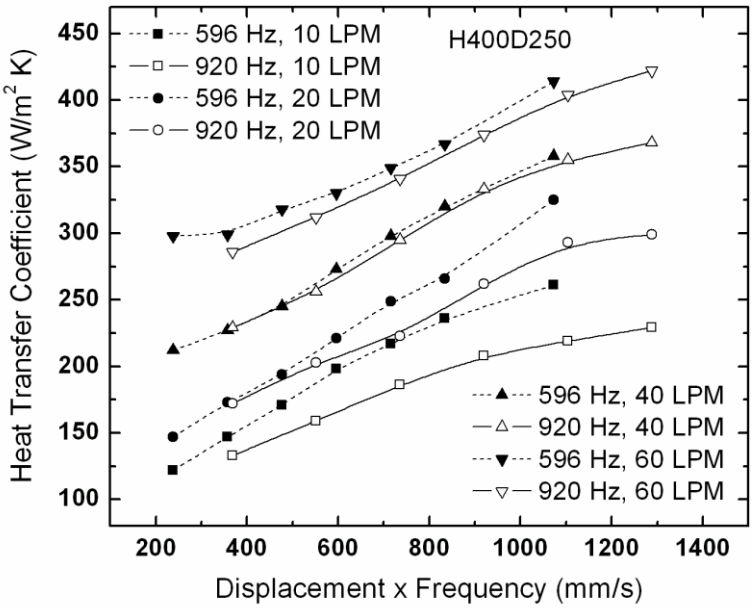

Figure 5.10: Heat transfer coefficients of micro pin-fin surface, H400D250, with respect to the peak velocities of the agitators

5.3.2 Pressure drop experimental results

Pressure drops over the micro pin-fin surfaces under translational agitation at different channel flow rates are presented in Figure 5.11. At lower flow rates of 10 and 20 LPM, the pressure drops due to micro pin-fin surfaces are not significant. In addition, the agitation also do not increase pressure drop too much, whether low or high agitation frequency. On the other hand, channel flow rate has a significant impact on increasing

pressure drop according to the results. At the lower flow rates of 10 and 20 LPM, there is a tendency for surface H400D250 to have larger pressure drop.

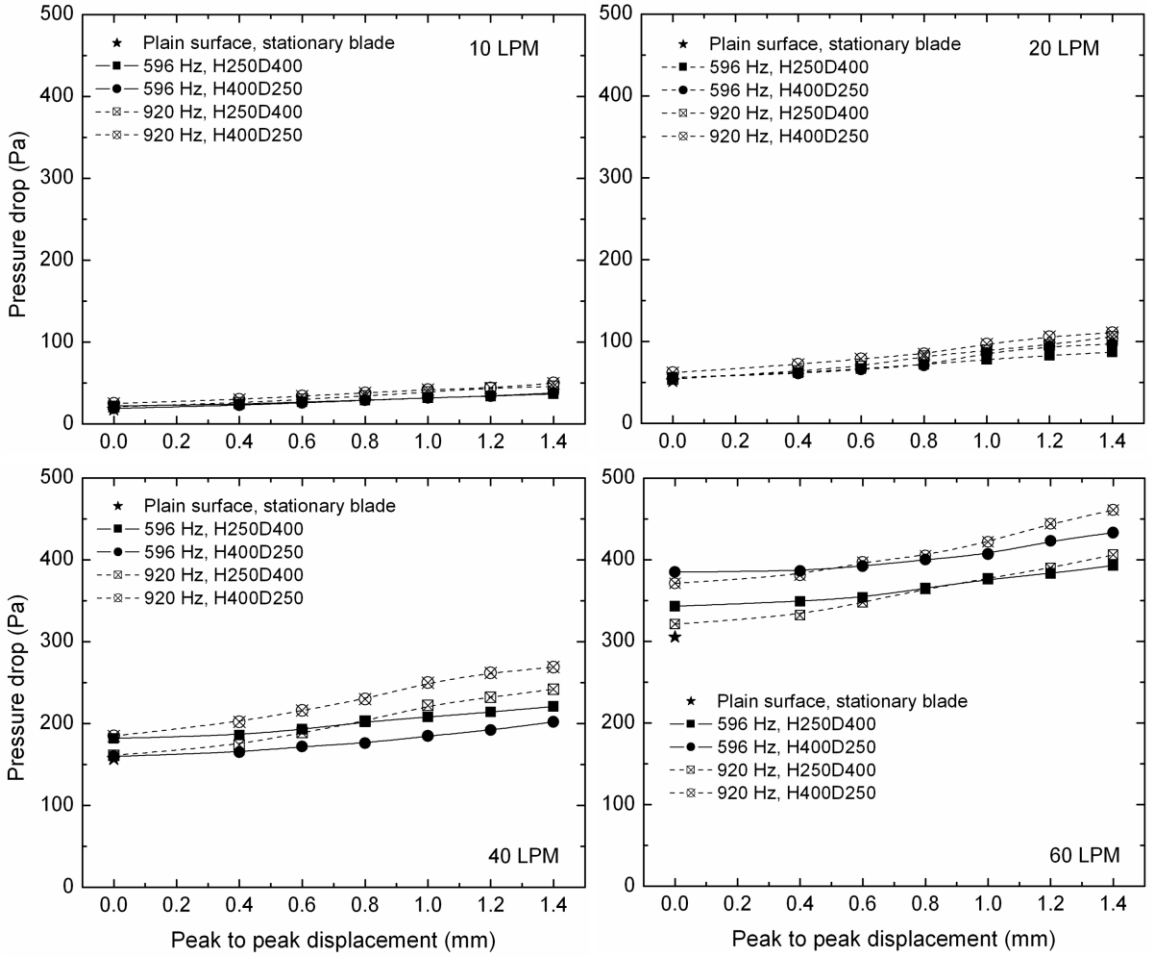

Figure 5.11: Pressure drops over micro pin-fin surfaces under translational agitations

The pressure drop range within the same flow rate shows remarkable jump compared to the lower level flow rates. When a flow rate increases to 40 LPM, the deviation in pressure drop between the two micro pin-fin surfaces becomes more apparent. At 40 LPM, the H250D400 surface has a larger pressure drop over the H400D250 surface at 596 Hz. However, at a higher frequency of 920 Hz, the H400D250 surface of has a larger pressure drop. The entire pressure drops at 40 LPM range between

150 Pa and 270 Pa. When a flow rate increases to 60 LPM, the pressure drop surpasses 300 Pa and reaches 461 Pa with the PTA operating at 920 Hz and 1.4 mm peak-to-peak displacement over the H400D250 surface. At a flow rate of 60 LPM, the H400D250 surface shows larger pressure drops at both operating frequencies over the entire displacement range. It is also interesting to see that the higher frequency operation does not necessarily ensure higher pressure drop over lower frequency agitation. At 40 LPM, the 596 Hz agitation over H250D400 generates larger pressure drops compared to the 920 Hz agitation over the same surface when the displacement is less than 0.6 mm. However, the higher frequency agitation gives larger pressure drops with displacements above 0.8 mm. At 60 LPM, a similar situation is observed. At the displacements less than 0.6 mm, lower frequency agitation of 596 Hz shows larger pressure drops for both micro pin-fin surfaces. Once the displacement rises over 0.8 mm, the pressure drops from the higher agitation of 920 Hz are shown to be larger than the ones from 596 Hz agitation. In sum, it is not easy to find certain patterns of pressure drop in respect to different operating frequencies and micro pin-fin surfaces. The measurement errors possibly can make some contributions to this. On the other hand, some unveiled factors might exist for tangling results of pressure drops since currently induced flow fields from the high frequency translational agitation with micro pin-fin surfaces must be extremely complex; there might be certain combinations of operating conditions (frequency and flow rate) that induce resonance in fluid resulting in excessive pressure drops. The investigations to reveal this phenomenon might be an interesting topic for future work.

5.4 Nusselt number and Stanton number

In order to characterize the combined effects of channel flow rates and translational agitation of the system, a total Reynolds number is defined in Equation (3.13). The total Reynolds number contains all the aspects of air currents generated in the test section by the channel flows and agitations. This leads the heat transfer coefficients (in Figures 5.4 ~ 5.7) to be re-plotted with respect to the total Reynolds number. Figure 5.12 shows heat transfer coefficients of the plain surface with the corresponding total Reynolds number at each operating condition point. The heat transfer coefficients are linearly distributed along with total Reynolds number. The R-squared error of the linear fit is 85.9% for the plain surface.

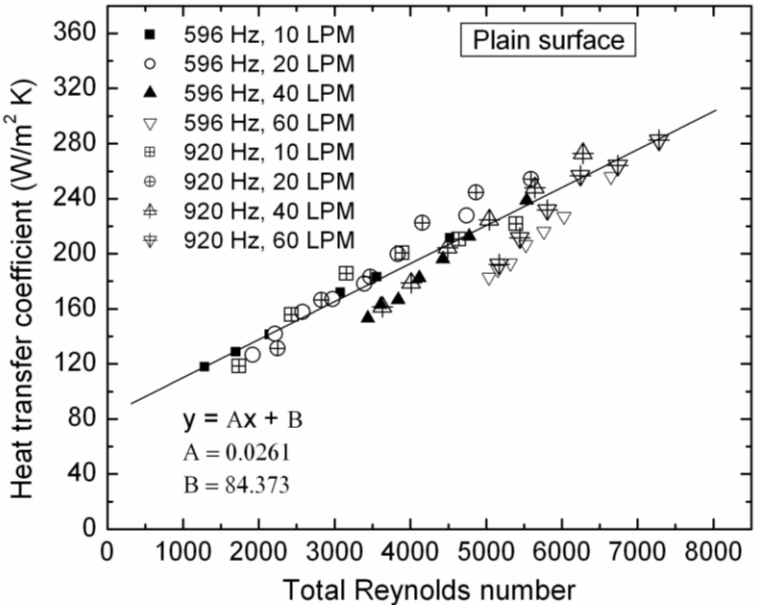

Figure 5.12: Heat transfer coefficient of plain surface in respect to total Reynolds number

The heat transfer coefficients of two micro pin-fin surfaces also show linear relationships with the total Reynolds number as shown in Figures 5.13 and 5.14.

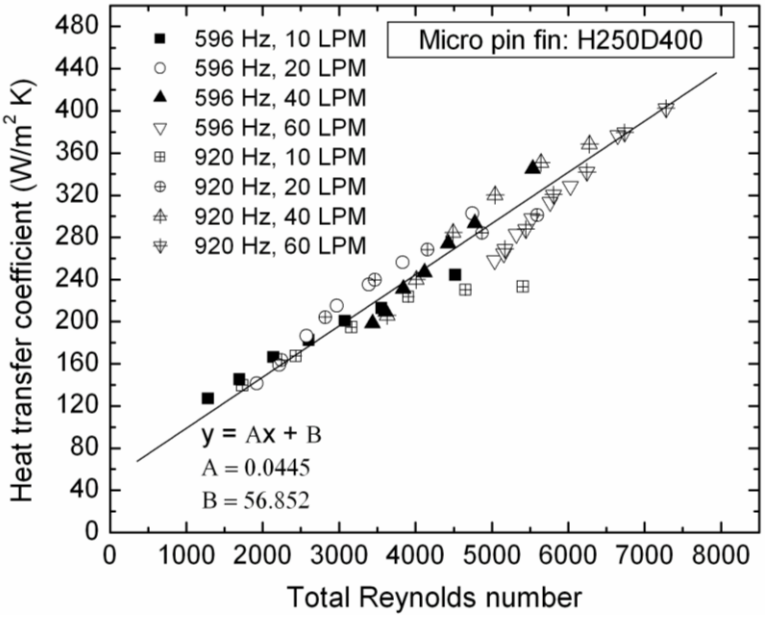

Figure 5.13: Heat transfer coefficient of the surface H250D400 in respect to total Reynolds number

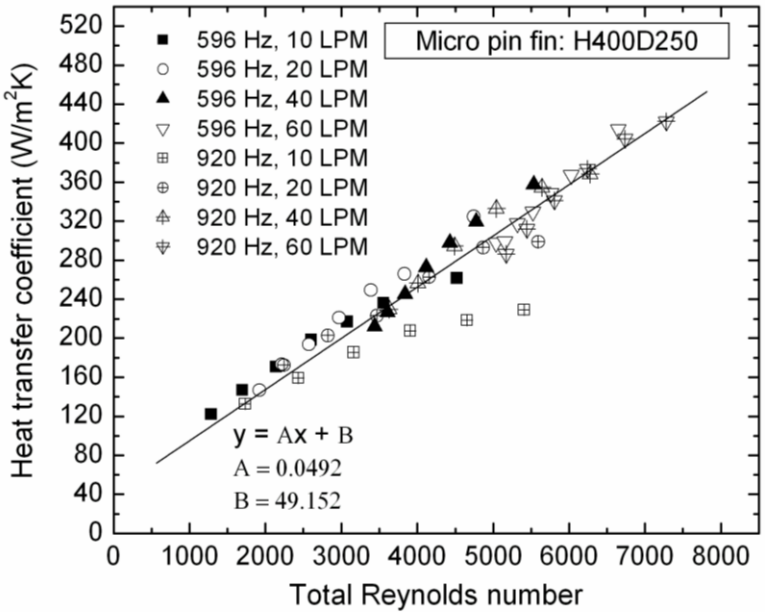

Figure 5.14: Heat transfer coefficient of the surface H400D250 in respect to total Reynolds number

The micro pin-fin surfaces have linear fits with increased gradients compared to those of plain surface. The constants, Π and Ω, of the linear relations of three surfaces are summarized in Table 5.2.

Table 5.2: Constants of linear relations between the heat transfer coefficients and total Reynolds numbers

	Ω	Π	R-squared error (%)	Stanton number
Plain surface	0.0261	84.4	85.9	0.00999
H250D400	0.0445	56.8	81.3	0.01730
H400D250	0.0492	49.2	80.9	0.01913

From the linear relationships between the heat transfer coefficients and the total Reynolds numbers, the expression for Nusselt number (Nu) is derived as:

$$\mathrm{Nu} = \frac{(h - \Pi)D_h}{k_{air}} = C\,\mathrm{Re}_{tot}\,\mathrm{Pr} \tag{5.1}$$

where k_{air} and Pr is the thermal conductivity and Prandtl number of air. The constant C is:

$$C = \frac{\Omega}{\mathrm{Pr}} \cdot \frac{D_h}{k_{air}} \tag{5.2}$$

The Nusselt numbers of the surfaces calculated based on Equation (5.1) is presented in respect to the total Reynolds number in Figure 5.15.

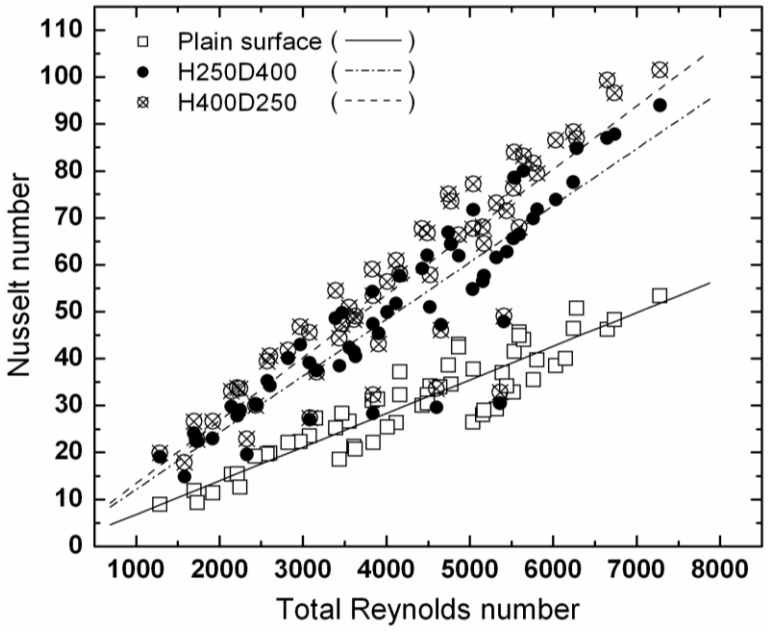

Figure 5.15: Nusselt number in respect to total Reynolds number

The results show that the micro pin-fin surface H400D250 provides slightly better cooling capability over the H250D400 surface under the translational agitations with channel flows. It is noted that the H400D250 surface also showed the best performance among eleven micro pin-fin surfaces with only channel flows. By substituting Equation (3.13) into Equation (5.1), the Stanton number, the non-dimensionalized heat transfer coefficient, could be obtained with further arrangement:

$$St = \frac{(h - \Pi)}{\rho_{air} c V_{eff}} = C \tag{5.3}$$

where the effective velocity of the system is given by:

$$V_{eff} = \sqrt{(V_{in})^2 + (\omega A)^2 (\frac{D_b}{D_h})^2} \tag{5.4}$$

Therefore, one can estimate the cooling capability of the PTA in the channel flow at specific operating conditions in terms of the operating frequency, displacement, blade

size, and channel flow rate using the definitions of Stanton number and effective velocity. According to Equation (5.3), the constant C is identical to the Stanton number of the surfaces. Figure 5.16 compares the Stanton numbers calculated both from Equations (5.2) and (5.3) for two micro pin-fin and plain surfaces. Therefore, the cooling performance of each surface could be characterized by the Stanton number. In addition, the heat transfer enhancement of the micro pin-fin surfaces under the translational agitation could be clearly confirmed over the plain surface. The calculation errors of the Stanton numbers from Equation (5.3) are shown in Figure 5.16. Comparing the Stanton numbers of three surfaces, the micro pin-fin surface H400D250 improved thermal performance about 91% over the plain surface while surface, H250D400, achieved an enhancement of 73%.

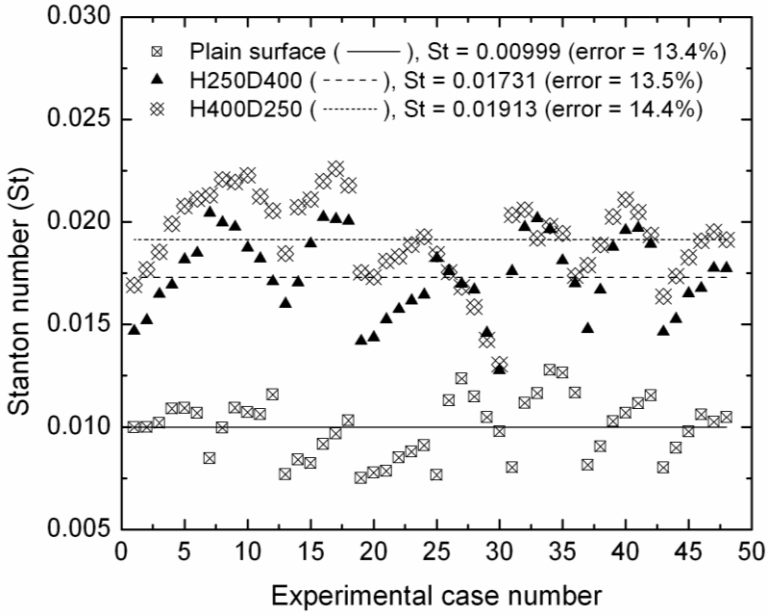

Figure 5.16: Stanton number of the micro pin-fin surfaces and plain surfaces

5.5 Thermal performance estimation of full size active heat sink

The single channel test section used for the heat transfer experiments of the current study represents one portion of the active heat sink equipped with the agitator and micro pin-fin surfaces. Therefore, estimating the overall thermal resistance of the full size active heat sink based on the results of the single channel experiments would be desirable and helpful for better understanding of the proposed cooling technology. Figure 5.17(a) shows the virtual heat sink that consists of 26 channels and a flow diverter in the center. The heat sink channels are assumed to have the H400D250 surface as it shows better thermal performance than the H250D400 surface. Air flow come from the both sides of the heat sink (blue arrows in Figure 5.17) and turns its direction 90 degrees using the slope of the diverter and leaves upward (red arrows in Figure 5.17) in the center of the heat sink. The upper side of the heat sink except for the channel inlets and outlet is covered by adiabatic plates. Figure 5.17(b) shows the cross sectional view of the heat sink channel. The two agitator blades positioned in the each side of the channel have adopted a shape to be fitted to the channels with a clearance of 1 mm all around the edges. The channel has a height and width of 23.5 and 3.4 mm at the inlet plane. The heat sink fin thickness is 1.1 mm. The agitator blade thickness is 0.6 mm. It is assumed that the heat transfer coefficients measured from the single channel test at the previous section are the average heat transfer coefficients of the entire active heat sink surfaces at the equivalent operating conditions.

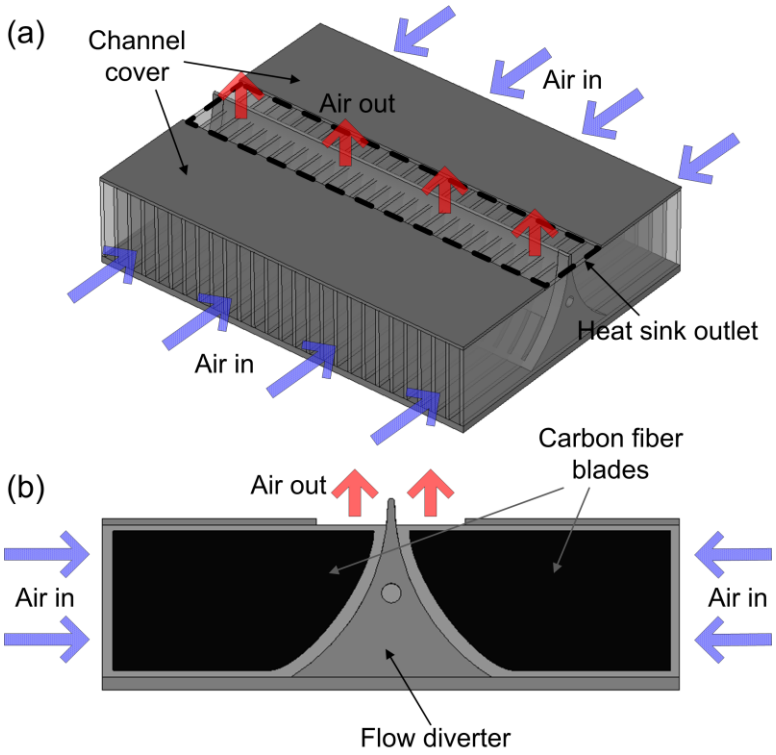

Figure 5.17: Schematic of virtual active heat sink module (a) heat sink and flow path, (b) single heat sink channel with agitator blades installed

The overall heat dissipation (q_{sink}) and inlet air temperature (T_{in}) of the active heat sink is assumed as 1 kW and 30 °C, respectively. Then, the air outlet temperature (T_{out}) of the heat sink can be calculated as:

$$T_{out} = T_{in} + \frac{q_{sink}}{\rho_{air} Q_{sink}} \tag{5.5}$$

where Q_{sink} is the converted heat sink flow rate that provides the same test section velocity with the single channel heat transfer experiments. The converted heat sink flow rates are summarized in Table 5.3.

Table 5.3: Flow rate conversion between single channel test and full size active heat sink

Single channel test flow rate (LPM)	10	20	40	60
Converted system flow rate (LPM)	589	1181	2362	3543

Herein, it is assumed that the heat sink has an isothermal temperature distribution across the entire surfaces. The heat sink base temperature (T_{sink}) must be calculated to get the thermal resistances of the active heat sink module with the assumed operating conditions of the heat sink. With the heat transfer coefficients (h) measured from the single channel heat transfer experiments, the following is valid with LMTD:

$$q_{sink} = h \cdot A_{sink} \frac{(T_{sink} - T_{out}) - (T_{sink} - T_{in})}{\ln\left(\frac{T_{sink} - T_{out}}{T_{sink} - T_{in}}\right)} \tag{5.6}$$

where A_{sink} is the convection surface of the active heat sink without considering the area increase due to the micro pin-fin surfaces. From Equation (5.6), the heat sink base temperature is calculated as:

$$T_{sink} = \frac{T_{out} - T_{in}\exp(Z)}{1 - \exp(Z)} \tag{5.7}$$

where Z is expressed as:

$$Z = \frac{h \cdot A_{sink}(T_{in} - T_{out})}{q_{sink}} \tag{5.8}$$

Therefore, the thermal resistance (R_{th}) of the active heat sink can be computed as:

$$R_{th} = \frac{T_{sink} - T_{in}}{q_{sink}} \tag{5.9}$$

Figure 5.18 shows the thermal resistance of the virtual active heat sink calculated from Equation (5.9) with respect to the total Reynolds number of the heat sink channel.

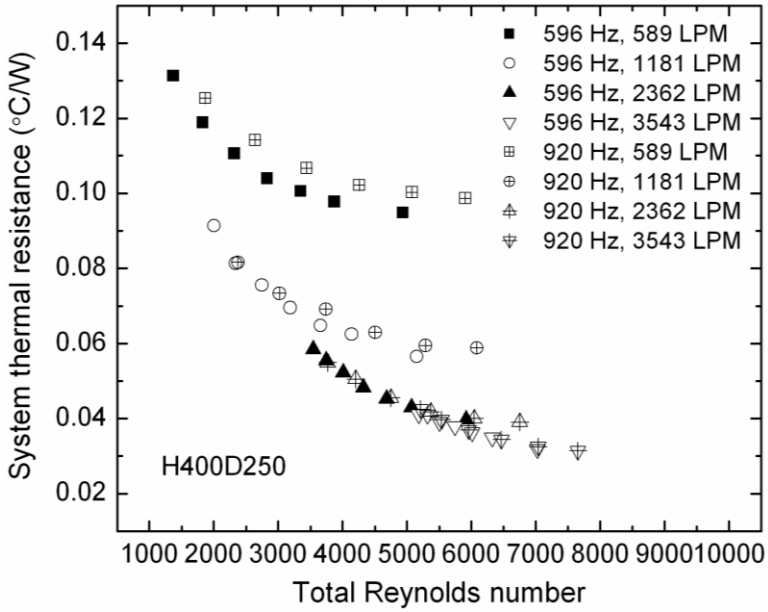

Figure 5.18: Thermal resistance estimation of the virtual active heat sink based on single channel test results

It is apparent that higher operating frequency, large displacement, and flow rates lead a lower thermal resistance. The effect of a displacement on the thermal resistance is significant, but tends to decrease as the total Reynolds number increases at a given operating frequency and flow rate. However, a frequency has a little impact on the thermal resistance as the agitations with two different frequencies generate the similar ranges of thermal resistance at given flow rates. The thermal resistance significantly improves as the flow rate increases. The active heat sink can achieve a thermal resistance of less than 0.04 °C/W at a high flow rate of 3543 LPM that gives the heat sink inlet velocity of 14.2 m/s and a total Reynolds number of around 7700.

5.5 Conclusions

In this chapter, the new cooling concept that combines both active and passive components was proposed to achieve efficient removal of heat from high power

electronics. The active component is the piezoelectric translational agitator that can generate high-frequency translational oscillation of the thin rigid blade. This high-frequency translational agitation is utilized to cool down the micro pin-fin surface which is the passive component of the system. The intensive heat transfer experiments were performed to verify the performance of the proposed technique in the single channel test facility. Eleven micro pin-fin plates were fabricated and their performance indices that characterize both thermal and hydrodynamic performance were compared. As a result, the micro pin-fin surfaces H400D250 and H250D400 were selected for the heat transfer experiments with the piezoelectric translational agitator at the single channel. The agitator operating at 920 Hz with a peak-to-peak displacement of 1.4 mm enhanced heat transfer coefficients of surface H400D250 by 150 and 130 % at the channel flow rates of 40 and 60 LPM compared to the non-agitated plain surface. The corresponding pressure drops across the test section of the single channel facility were measured and compared. It was confirmed that the agitation did not increase pressure drop regardless of operating frequency. However, a channel flow rate has a significant impact on increasing pressure drop. In order to consider the effects of cross flows and translational agitation on cooling performance of the system at the same time, the analyses on the total Reynolds number and Stanton number were conducted. Each surface has its own Stanton number that characterizes thermal performance. As a result, the micro pin-fin surface H400D250 with translational agitation and channel flow improved the overall cooling capability about 91% over the plain surface. The virtual active heat sink module aided with the agitator and micro pin-fin surfaces was proposed and its thermal performance was estimated

based on the heat transfer coefficients measured in the single channel. The proposed virtual active heat sink module with an array of 26 channels installed with 52 agitator blades is shown to provide a thermal resistance of around 0.04 °C/W at its best operating condition. This is fairly a good cooling capability in terms of a system thermal resistance. However, a detailed mechanism for driving multiple-blade structure was not discussed here. The required power consumptions to drive the multiple-blade agitator and channel flow through the heat sink module are the important factors which must be addressed to further develop the proposed active heat sink technology. In Chapter 6, the actual active heat sink module will be introduced with a multiple-blade agitator system. Thermal performance and required power to drive the entire active heat sink module will be discussed.

Chapter 6:
Active Heat Sink System

6.1. Objective of the Chapter

In Chapter 6, an active heat sink system with a piezoelectrically-driven translational agitator and with micro pin fin arrays is fabricated and its thermal and hydrodynamic performance characteristics are demonstrated by conducting single- and multiple-channel heat transfer experiments. A detailed discussion on the characteristics of the multiple-blade agitator's driving system and the required power aspects for the entire active heat sink system are provided.

6.2 Active Heat Sink System

The concept of the active heat sink system was introduced in Chapter 1. Figure 6.1 shows more detailed aspects of the active heat sink with translational agitator blades and a micro pin-fin surface. In general, channel flow induced by the fan or blower falls in the laminar regime in such a heat sink system (Figure 6.1(b)). In the active heat sink system, the blade oscillates with a high-frequency, translational motion and breaks down the thermal boundary layer on the wall by vigorously agitating the flow passing through the channel. The blade could be either short or long, as shown in Figures 6.1(c) and 6.1(d). A long blade directly breaks and thins the thermal boundary layers of the wall mostly by strong favorable and adverse pressure gradients while a short blade produces vortices at the edges of the blade that contribute to convective heat transfer in the channel. Figure 6.1(e) shows a staggered micro pin fin array on the surface of the active heat sink channel

wall. The micro pin fin array contributes to disturbing the thermal boundary layers as well as augmenting heat transfer area.

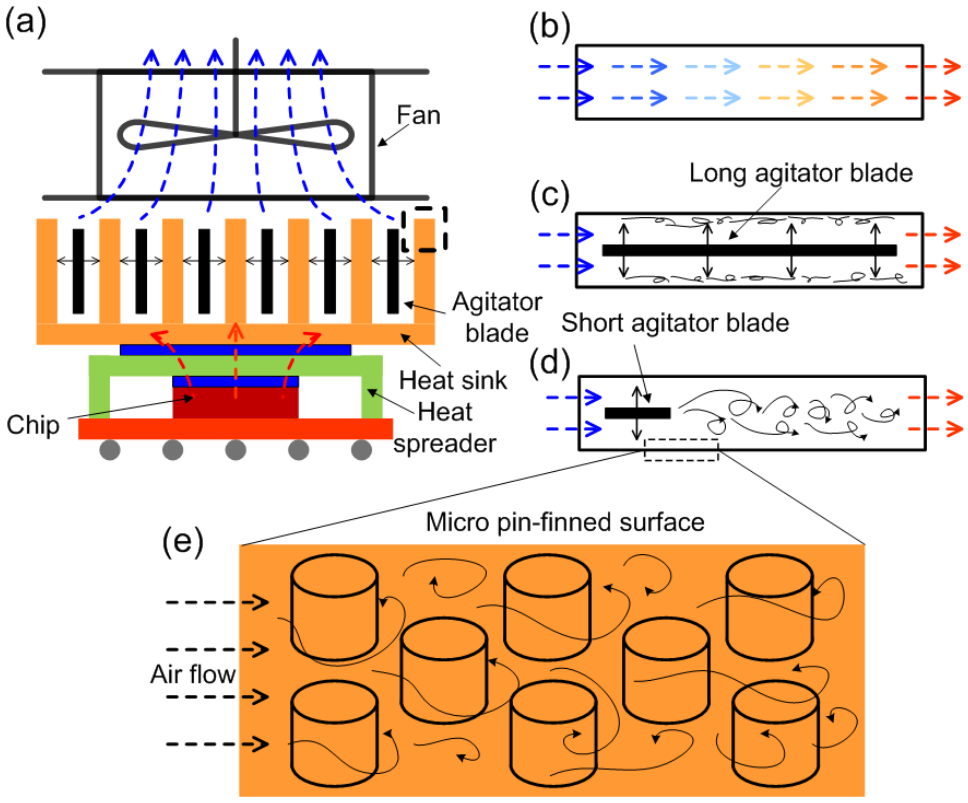

Figure 6.1: (a) Conceptual illustration of active heat sink with translational agitator blades embedded between heat sink channel walls, (b) a traditional plain-surface heat sink channel without an agitator blade, (c) an active heat sink channel with a long agitator blade, (d) an active heat sink channel with a short agitator blade, (e) schematic of staggered arrays of micro pin fins on the active heat sink channel walls.

Figure 6.2(a) shows a detailed view of the heat sink design used in the current study. The heat sink, which is made with pure copper, has 26 channels formed by an array of 27 fins. Air enters from the both sides. Heated air passes through the channels and discharges upward in the center of the heat sink, as directed by a flow diverter. The heat sink base has an area of 114 × 89 mm (4.5 × 3.5 inches) and the fin height is 23.6 mm. The heat sink has four arrays of slots through the fins (distributed in the streamwise

direction) to accommodate the driving frames that hold the agitator blades. The module has either 26 short blades (left in Figure 6.2(a)) or 26 long blades (right in Figure 6.2(a)) on each side of the heat sink. Figure 6.2(b) shows the flow path through the single channel and Figure 6.2(c) shows both short (left) and long (right) blades inserted into the channel.

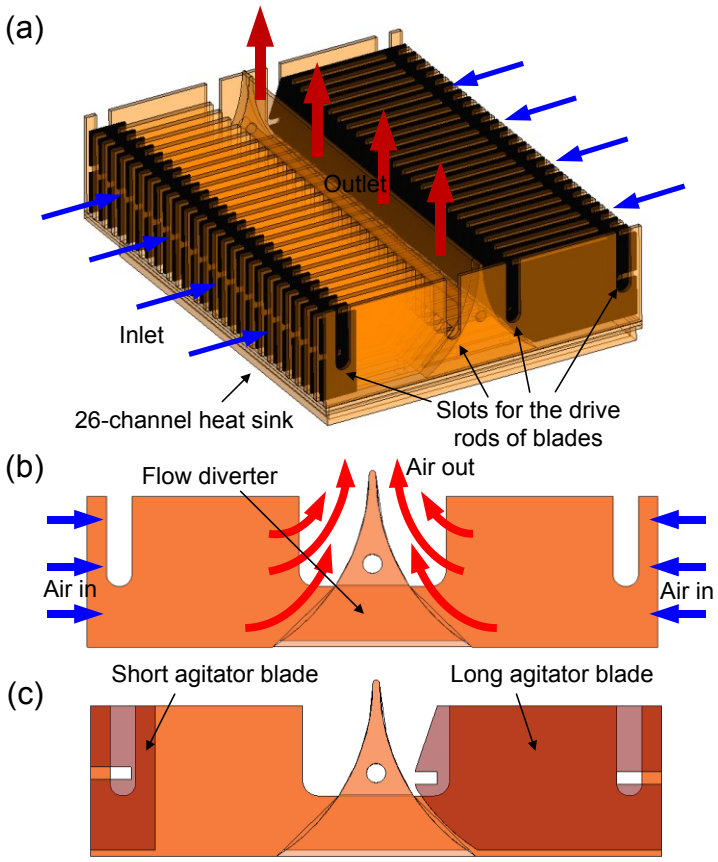

Figure 6.2: (a) Copper heat sink with 26 channels, (b) cross sectional view of the heat sink channel, (c) blades installed in the channel.

6.3 Multiple-Blade Piezoelectric Translational Agitators

A piezoelectrically-driven translational agitator utilizes resonance energy of an oval loop shell to create translational oscillation of the blade in each heat sink channel.

This high-frequency oscillating motion is used for generating strong air currents against the heated surfaces making a very effective cooling device. Figure 6.3 shows the piezoelectric translational agitator with a single-blade carbon fiber structure for a single channel active heat sink system. The oval loop shell amplifies displacement from the micrometer-range displacement (horizontal red arrows) of a piezo stack actuator which is compressed into the structure to the millimeter-range translational displacement (vertical blue arrow) of the agitator. The operating frequency and displacement can be controlled by the height, length, and thickness of arc beams of the oval loop shell, as well as by the mass and stiffness of the blade structures attached. More detailed analyses on the static and dynamic characteristics of the oval loop shell actuator are presented in Chapter 2.

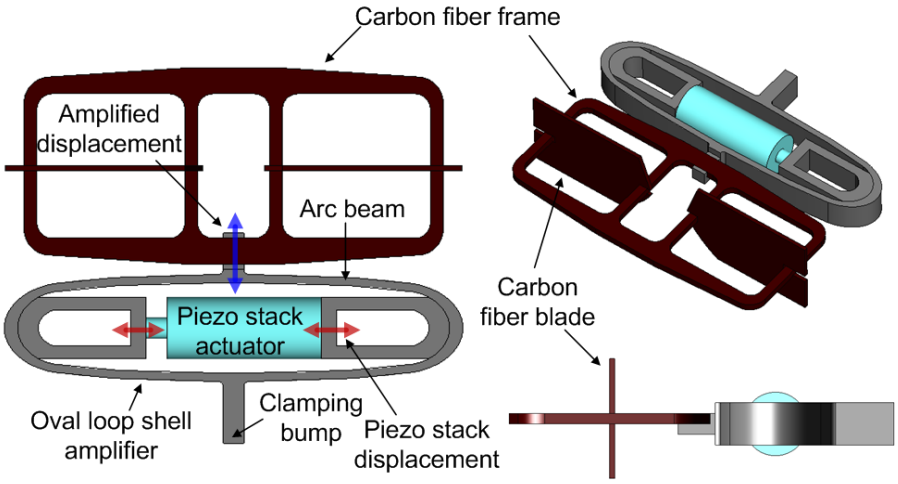

Figure 6.3: The piezoelectric translational agitator for a single channel active heat sink system.

The single-blade structure, one shown in Figure 6.3, can be easily extended to multiple-blade agitators driven by one or two oval loop shell amplifiers by stacking up more blades on supporting frames. In this chapter, several agitators with single- and multiple-blades are introduced in order to demonstrate the heat transfer capacity of the

active heat sink system. The blade structures with either single- or multiple-blades are shown in Figure 6.4. Blade-1 has one array of two long blades that occupy the entire channel length, as shown in Figure 6.2(c). This blade is for the single channel heat transfer test. Blades-2, -3, and -4 are 26-blade arrays of either short or long blades for use in the full-module, 26-channel heat transfer test. The agitators with multiple-blade structures are illustrated in Figure 6.5.

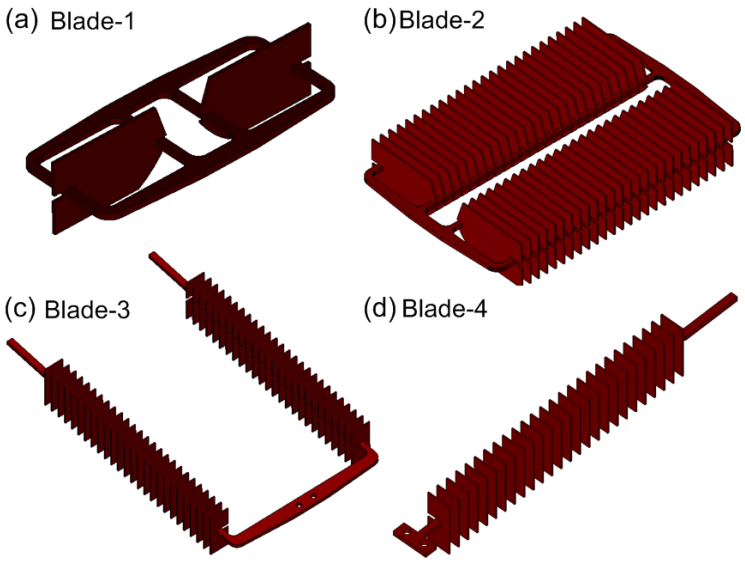

Figure 6.4: Carbon fiber blade structures, (a) one array with long blades, (b) 26-blade array with long blades, (c) 26-blade array of short blades with U-shaped drive frame, (d) 26-blade array of short blades with I-shaped drive frame.

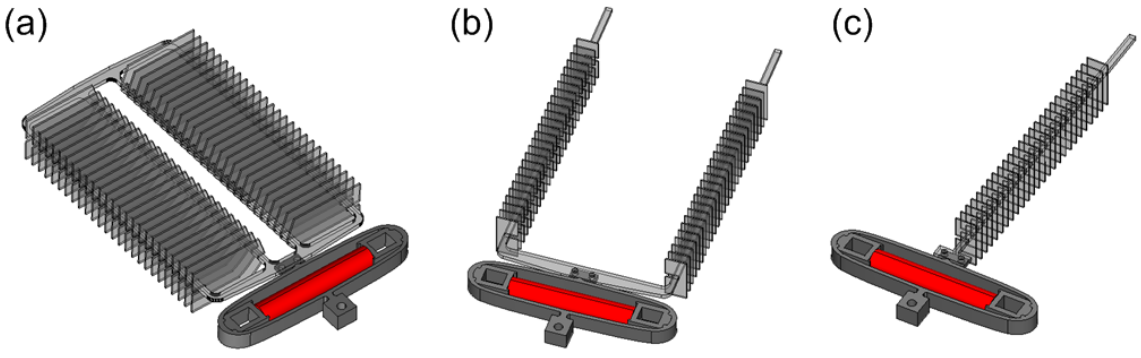

Figure 6.5: Multiple-blade agitators with different blade structures.

Carbon fiber composite plates are used for fabricating the blade structures for they have very high stiffness-to-weight ratio compared to other common metal materials. The high stiffness with small weight of the blade structure ensures higher resonance frequency of the agitator. The multiple blade structures are designed in a way that the driving rods pass through the center of the blade plates so that flapping motion of the blades can be prevented. This scheme also improves the stiffness of the structure and increases resonance frequency of the agitator. Operating conditions of the piezoelectric translational agitators with different blade structures are summarized in Table 6.1.

Table 6.1: Operating conditions of the piezoelectric translational agitators

Agitator type	Blade type	Blade Weight (g)	Operating frequency (Hz)	Power consumption (W)	Peak-to-peak displacement (mm)
A1	Blade-1	4.5	~ 680	7.8	1.4
A2	Blade-2	37.0	222	2.5	1.0
A3	Blade-3	11.5	512	5.0	1.4
A4	Blade-4	5.5	780, 820	5.6, 5.6	1.4

The agitators for the multiple-channel system are driven by one oval loop shell actuator, except for the agitator type A4 which is driven by two actuators, one at each side of the heat sink. With the 26-blade array of long-blades, the agitator operates at 222 Hz with a peak-to-peak displacement of 1.0 mm. As the blade length is shortened, the operating frequency of the agitator increases to 820 Hz for the shorted blade. For the agitator type A4, two different oval loop shell amplifiers with the same design parameters are used to drive two I-shaped blade structures. Due to fabrication imprecision, the two agitators have slightly different operating frequencies of 780 Hz and 820 Hz. Figure 6.6 shows the agitators with multiple blades installed inside the heat sink channels.

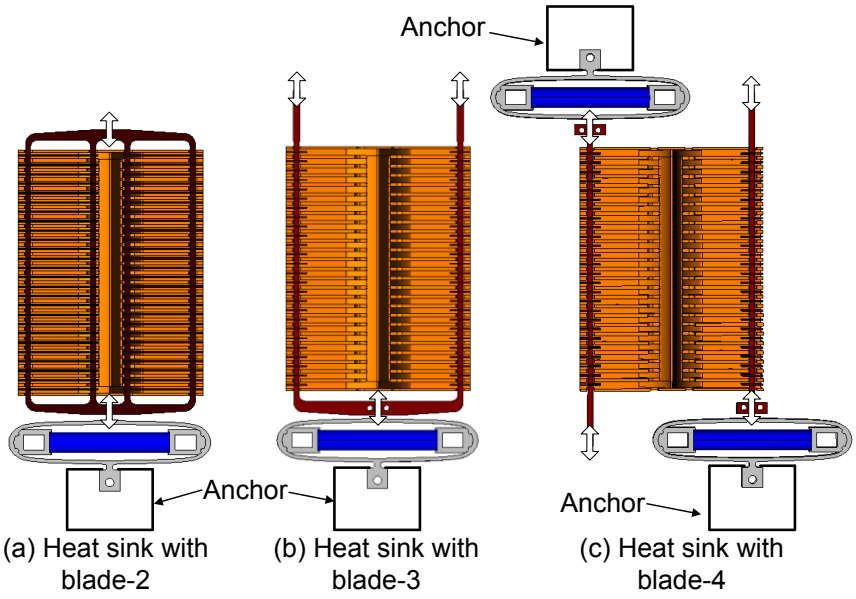

Figure 6.6: Heat sink with different configurations of agitator blades, (a) 26-blade array of long-blade with one drive system, (b) 26-blade array of short-blade with one drive system, (c) 26-blade array of short-blade with two drive systems.

6.4 Double-Sided Micro Pin-Fin Surface

Another important feature of the active heat sink system is the micro pin fin array on the surfaces of the heat sink. They dramatically increase convective heat transfer area. The double-sided LIGA technique is used for fabricating the copper pin fins on the heat sink channel walls. Figure 6.7 shows the fabrication process of the double-sided micro pin-fin surface. First, a 102 mm (4-inch) diameter copper wafer substrate with a thickness of 1.1 mm is prepared and cleaned using acetone, methanol, isopropyl alcohol, potassium hydroxide, and sulfuric acid. Next, the protective layers of Titanium (Ti) are deposited on the both sides of the substrate (Figure 6.7(a)). As the next step, the top and bottom layers of KMPR are coated on the copper substrate (Figure 6.7(b), (c)). The KMPR layers are exposed to UV light and patterned to develop mold structures for electroplating the copper micro pin fins. The etching process of the Ti layers is followed using diluted

hydrofluoric acid (Figure 6.7(e)). Then, copper micro pin fins are electroplated over the patterned copper substrate in a plating bath. Finally, the residual of the KMPR and Ti layers are removed and a double-sided micro pin-fin wafer is achieved. The wafers are then cut into the heat sink fin shape using a wire EDM (Electrical Discharge Machining) process.

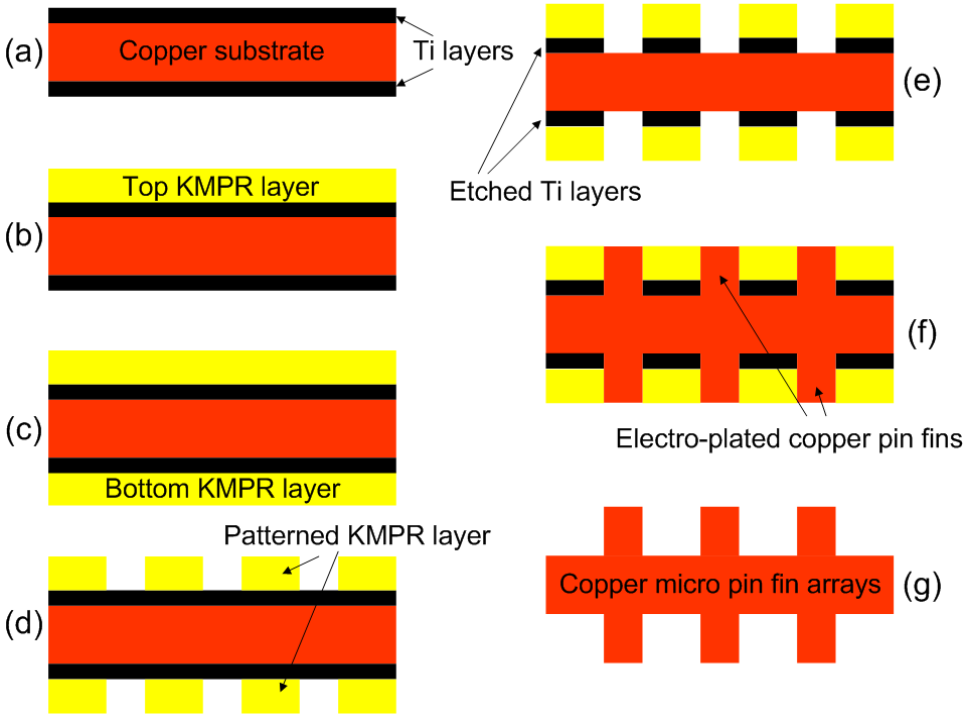

Figure 6.7: Fabrication process of double-sided micro pin-fin surface, (a) double-sided Ti metal layer deposition, (b) top layer KMPR coating, (c) bottom layer KMPR coating, (d) KMPR photoresist mold development, (e) double-sided etching of Ti layers, (f) electroplating of the copper pin fins, (g) removal of the KMPR and Ti layers.

The single heat sink fin with micro pin fins electroplated on both sides is shown in Figure 6.8. Totally, twenty five double-sided micro pin-fin plates to be the inner walls of the heat sink module and two single-sided micro pin-fin plates for the side walls of the module are cut and soldered to the copper heat sink base. Slots are made at the flow diverter to guide the soldering process with an accurate pitch of the fins in the heat sink

module. The micro pin fins have height, diameter, and pitch of 250 μm, 500 μm, and 1500 μm, respectively.

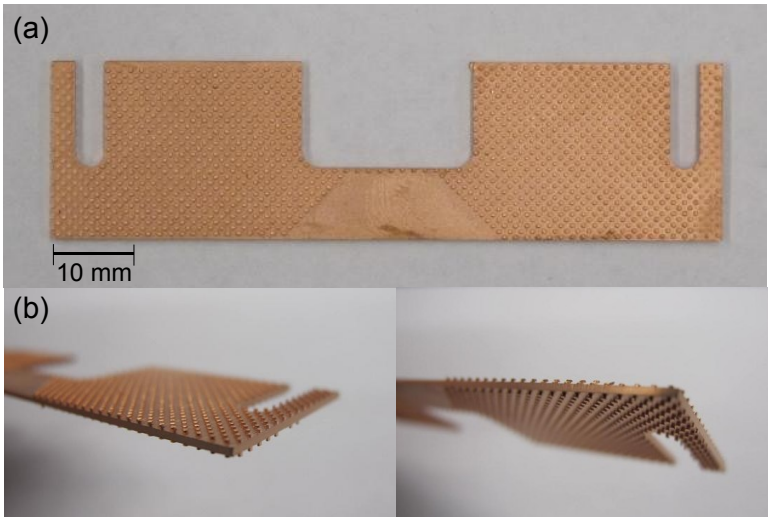

Figure 6.8: (a) Single heat sink fin with double-sided micro pin-fin surfaces, (b) micro pin fin arrays on both sides of fin

6.5 Heat Transfer Test of Single Channel Heat Sink

The concept of the active heat sink was demonstrated in a single-channel system prior to advancing to a full-size system. Yu et al. [119] previously conducted a preliminary study about the thermal performance of a single-channel heat sink with a piezoelectric agitator and synthetic jets. Figure 6.9 shows the schematic of the heat transfer experimental facility. A vacuum pump (blower) is used to generate the channel flow through the active heat sink and a flow meter is positioned between a test section and the blower. A function generator and voltage amplifier produce an amplified sine wave signal to drive the piezoelectric translational agitator. A DC power supply is used to provide power to a heater. A manometer measures local static pressure at the outlet. The Agilent data acquisition system is used to log the data. This test facility could be used for

either the single- of multiple-channel heat transfer experiment by simply switching the test sections.

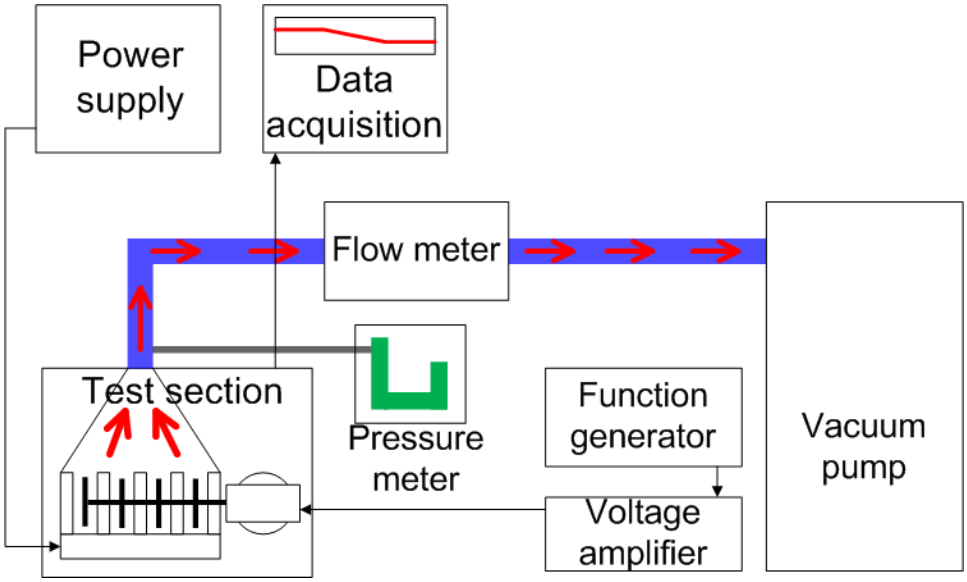

Figure 6.9: Schematic of heat transfer experiments.

The test section of the single-channel heat transfer experiment is shown in Figure 6.10. A long, narrow, and thin copper block is used as a path for heat conduction from the heater to the convectively-cooled channel surfaces. A film heater is attached at one end of the copper block. At the other end, a single channel of active heat sink is simulated by soldering two heat sink fins (Figure 6.8) to the copper block. The outside of channel area is well insulated with bass wood to prevent heat loss. A discharge adapter connects the test section to the external blower. Most of the testing in the single channel experiment is with the long-blade (A1) agitator. The channel has a width of 3.4 mm. The agitator blade of 1.0 mm thickness is placed in the center of the channel. The blade has an edge clearance of 1.0 mm from the bottom of the channel and 2 mm from the top of the channel. The heights of the blade and channel are 22.5 mm and 23.6 mm, respectively.

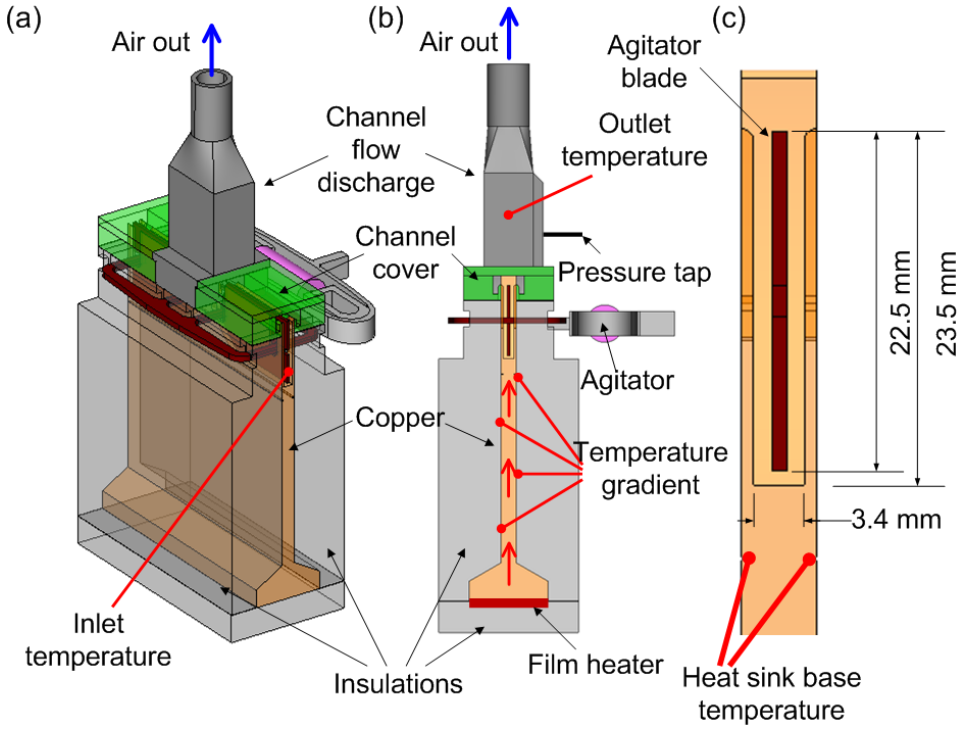

Figure 6.10: (a) Test section of the single-channel heat transfer experiment (b) front view of the test section (c) inlet of the single channel.

Twelve thermocouples are used to measure the base temperatures (T_{base}) of the heat sink. Eight thermocouples are used to measure the temperature gradient (ΔT_c) in the 1-D heat conduction section of the copper block to calculate heat input (q) from the heater as:

$$q = kA_c \Delta T_c / \Delta x \tag{6.1}$$

where k, A_c, and Δx are the thermal conductivity of copper, the cross sectional area of the copper block, and the distance between the thermocouples, respectively. The heat transfer coefficient (h) is calculated by the Log Mean Temperature Different (LMTD) method:

$$h = q/(\Delta T_{LMTD} \times A) \tag{6.2}$$

herein, A is the convective area of the single channel. The ΔT_{LMTD} is computed as below:

$$\Delta T_{LMTD} = \frac{(T_{fin,in} - T_{in}) - (T_{fin,out} - T_{out})}{\ln[(T_{fin,in} - T_{in})/(T_{fin,out} - T_{out})]} \quad (6.3)$$

where T_{in}, T_{out}, $T_{fin,in}$, and $T_{fin,out}$ are the inlet and outlet temperatures of channel flow and heat sink fins. Figure 6.11 presents the temperature variations of the single-channel heat sink with a plain surface after the piezoelectric translational agitator is turned on to operate at a frequency of 770 Hz and a peak-to-peak displacement of 1.4 mm. The flow rate is 96 LPM, which provides a channel velocity of 8.1 m/s. The heater input power is 38.5 W, which is based on the expected heat dissipation of 1.0 kW for the full-size active heat sink system having 26 channels. Therefore, the thermal resistance (R_{th}) of the full size heat sink with 26 channels is estimated from temperature measurements in the single channel heat sink with the expected heat dissipation of 26-channel module as:

$$R_{th} = (T_{base} - T_{in})/(q \times 26) \quad (6.4)$$

where T_{base} is the averaged temperature at the base of the single channel heat sink. Data indicate that the agitator decreases the heat sink temperature 15°C. This corresponds to a thermal resistance for the full-size system of 0.073 °C/W and a heat transfer coefficient of 180 W/m²°C. These represent 22 % and 38 % enhancement over the channel flow-only case. The calculated uncertainty of the heat transfer coefficients in the current study is 7 %, based on the methodology of Moffat [120].

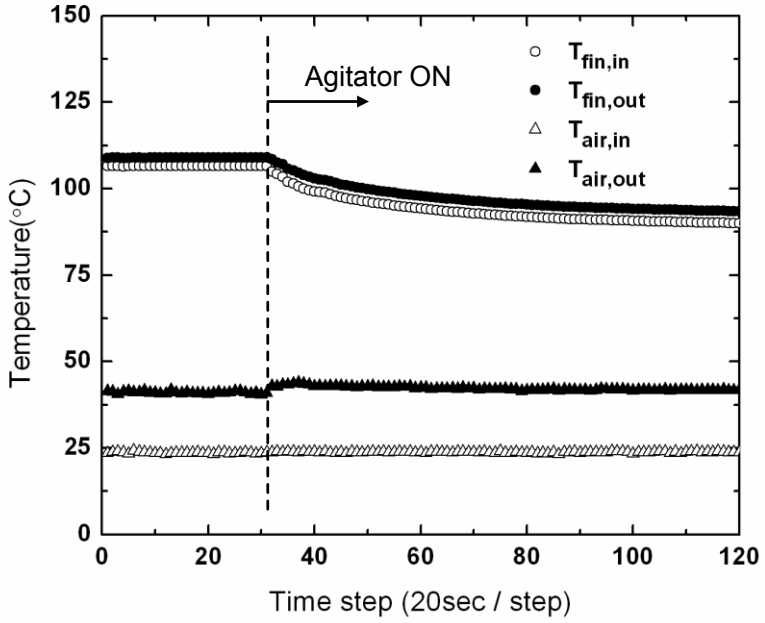

Figure 6.11: Temperature variations of the single channel heat sink with the agitator operational under a channel flow rate of 96 LPM.

The experiments are conducted also with a micro pin-finned single channel heat sink. Instead of the plain surface fins, two single-sided micro pin-fin channel walls are soldered to the copper block base. The agitator ran at 686 Hz with a peak-to-peak displacement of 1.4 mm. The channel flow rate remained at 96 LPM. In addition, the projected area at the inlet plane of the upper tip clearance region was blocked to maximize thermal performance. This reduced bypass flow through the clearance region near the channel entrance and forced more flow through micro pin-finned regions, resulting in better thermal performance of the heat sink. The heat transfer experimental results, including both plain surface and micro pin-fin surface heat sink results, are summarized in Table 6.2. When the agitator is turned off in the micro pin-fin heat sink, but all else is the same, thermal resistance is shown to be 25 % below that of the plain surface heat sink. This is a lower thermal resistance (0.071°C/W) than that of the plain

heat sink with the agitator turned on (0.073°C/W). The single-channel active heat sink equipped with the piezoelectric translational agitator and micro pin-fin surfaces reduces the thermal resistance 44 % below the case with the plain surface heat sink with channel flow-only. However, the pressure drop is increase more than 100 %.

Table 6.2: Summary of the single channel heat transfer experiment results

Heat sink	Channel Flow rate (LPM)	Operating frequency (Hz)	Heat transfer coefficient (W/m^2 °C)	Thermal resistance (°C/W)	Pressure drop (Pa)
Plain	96	0	130	0.094	155
Plain	96	770	180	0.073	163
Micro	96	0	188	0.071	257
Micro	96	686	292	0.053	327

6.6 Heat Transfer Test of Multiple Channel Heat Sink

The agitators with three different blade structures (Figure 6.5) are tested in the 26-channel, full-size heat sink with plain surfaces and micro pin-fin surfaces. Figure 6.12 shows a schematic of the full-size active heat sink test section that replaced the single-channel test section in the heat transfer experimental loop shown in Figure 6.9. In Figure 6.12, the agitator, A2, with the 26 long-blade structure is installed. At the most bottom part, a glass fiber insulation block is supporting a heat spreader with eleven cartridge heaters inserted. The active heat sink either with the plain surface or the micro pin-fin surface is connected to the heat spreader block using a high-conductivity thermal paste. Air temperatures are measured in the vicinity of the inlets, and air outlet temperatures are measured at the discharge adapter using thermocouples inserted through the adapter wall, as shown in Figure 6.12. A pressure tap is located 25 mm (one inch) below the thermocouples used to measure the outlet temperatures. The heat sink base temperatures are measured at different locations in the heat sink base, including the bottom and side

surfaces. These temperatures are averaged to calculate the system thermal resistance, R_{th}, of the active heat sink:

$$R_{th} = (T_{base} - T_{in}) / q \tag{6.5}$$

where T_{base}, T_{in}, and q are the averaged heat sink base temperature, air inlet temperature, and heat dissipation. The heat dissipation through the heat sink is calculated using an energy balance:

$$q = \dot{m}c(T_{out} - T_{in}) \tag{6.6}$$

where $\dot{m}$, c, and T_{out} are the mass flow rate, specific heat, and air outlet temperature, respectively.

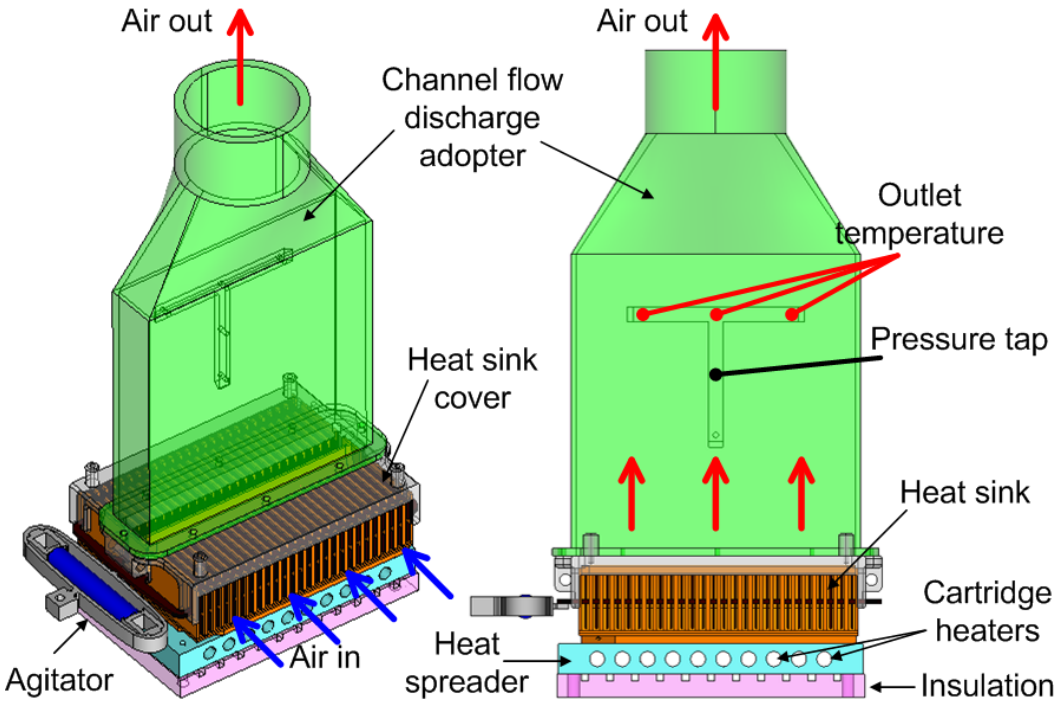

Figure 6.12: Test section of the full-size active heat sink heat transfer experiment.

Figure 6.13 shows the actual short blades of the agitator oscillating in the channel and viewed from above in the orientation of Figure 6.12. It is operating with a frequency of 512 Hz and a peak-to-peak displacement of 1.4 mm. The high-frequency oscillating motion of the agitator blades could be confirmed from the fuzziness of the photo. The oscillating displacement of the blade in the channel is estimated in the photo by comparing the thickness of the fuzzy view with the heat sink fin thickness (1.1 mm).

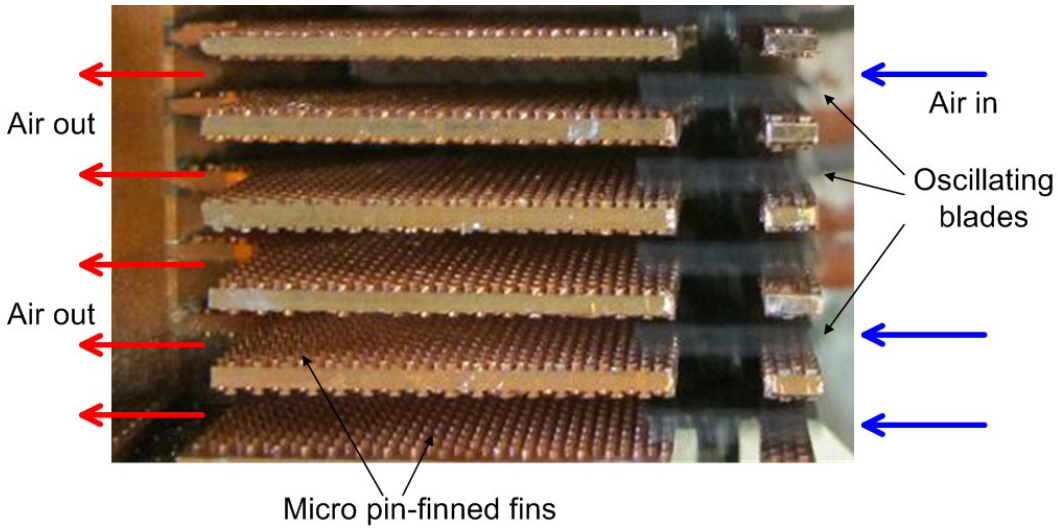

Figure 6.13: Oscillating short blades inside the micro pin-fin heat sink channels.

The thermal resistances of the active heat sink with plain and micro pin-fin surfaces are compared under different heat sink flow rates in Figure 6.14. Actual heat input to the system varied from 630 W to 930 W according to the heat sink temperature, as a temperature of the heat sink that is too high can damage the system when the active heat sink is operating at its lower-level operating conditions. The agitator, A2, with a 26-blade, long-blade structure decreases thermal resistance of the plain surface heat sink system by 3.5% from 0.139 °C/W to 0.135 °C/W. The poor enhancement is mainly due to the lower operating frequency of 220 Hz caused by the large mass of blade structure.

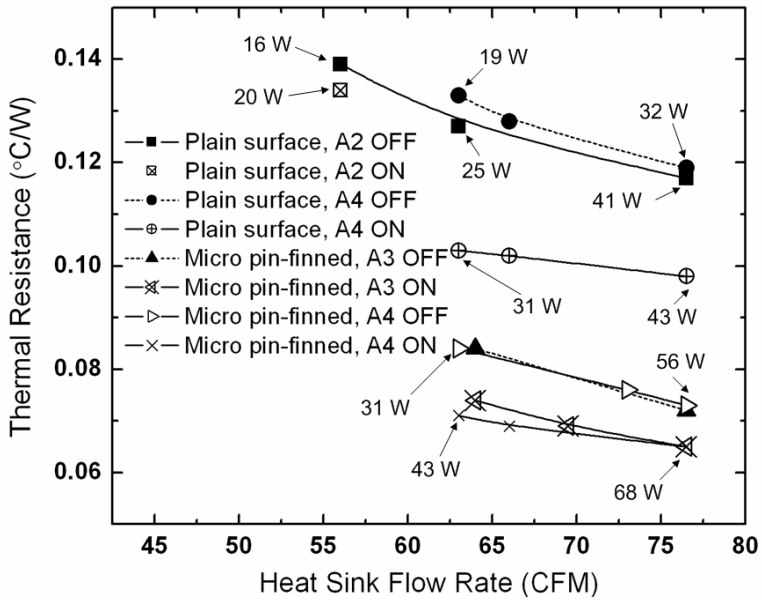

Figure 6.14: Thermal resistances of the active heat sink system.

When the short-blade structure of A4 is installed into the heat sink, but turned off, the thermal resistance is slightly larger than that of the long-blade case. The short blade provides more flow path area and, thereby, decreases channel flow velocity resulting in larger thermal resistance. However, once the agitator is turned on with an operating frequency of 800 Hz, the thermal resistance decreases 18% to 22% over the flow rate range. It is confirmed that the short-blade agitator with a high operating frequency can provide better cooling performance than the long-blade agitator operating with a lower frequency. As the short-blade agitator shows better performance in the plain surface heat sink, the agitators, A3 and A4, were next tested with the micro pin-fin heat sink. First of all, the micro pin-fin heat sink alone was shown to provide large cooling capacity without operation of the agitators, decreasing thermal resistance 37 % compared to the un-agitated plain-surface heat sink. The agitators, A3 and A4, further decrease thermal resistance 11% and 13 %, respectively. It is interesting to note that the two agitators with

short-blade, but with different operating frequencies show similar thermal performance, implying that the effect of displacement might be more import than those of operating frequency. Overall, the active heat sink with the piezoelectric translational agitator and micro pin fins can enhance the thermal performance about 46 % over the non-agitated, plain heat sink case when operating under the most favorable conditions.

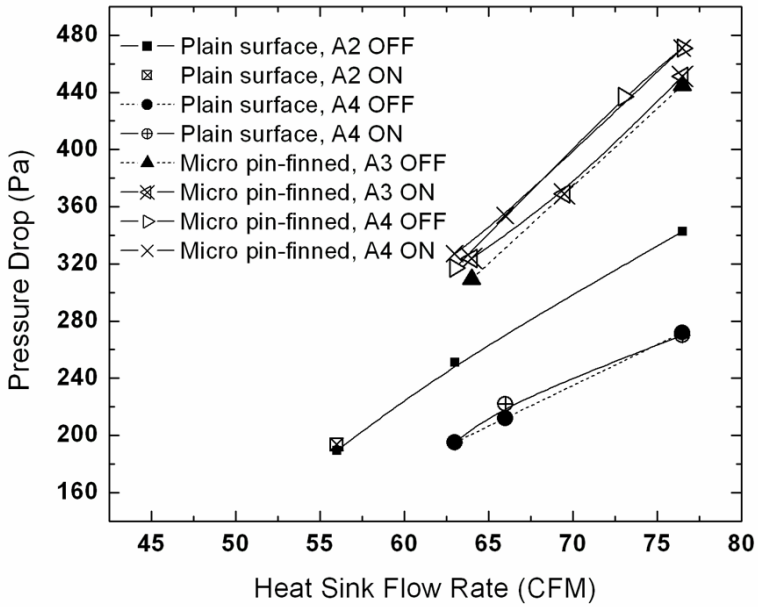

Figure 6.15: Pressure drop of the active heat sink system.

The corresponding pressure drops of the active heat sink system are shown in Figure 6.15. The pressure drop has a similar, but reversed pattern compared with the thermal resistance results. The case with smaller thermal resistance provides larger pressure drop. This is the general fact that increasing cooling performance of a heat sink system generally comes with increased pumping power. It is notable to see that micro pin fins generate much larger pressure drop than do the agitators. The agitators increase pressure drop less than 5%, and around 2%, for most of the cases compared to the cases with the agitators off. It is also very important to see the power consumption of each

component when they operate as a system; therefore, the total power consumption values of the active heat sink when operated under various operating conditions are noted in Figure 6.14. The total power consumption (P_{total}) is the sum of blower power required to drive the flow through the heat sink and electrical power consumption of the agitators as shown below:

$$P_{to} = P_{blower} + P_{agitator} \tag{6.7}$$

The fluid power is calculated by multiplying measured pressure drop (Δp) and volume flow rate (Q). From the fluid power, the blower power is computed assuming the fan efficiency (η) is 30%:

$$P_{blower} = \frac{\Delta p \times Q}{\eta} \tag{6.8}$$

The electrical power consumption of the agitator is calculated by measuring time-varying applied voltage (V(t)) and current (I(t)) to the agitator as:

$$P_{agitator} = \frac{1}{T}\int_0^T V(t) \cdot I(t) dt \tag{6.9}$$

where T is the period of data measurement. When the agitator with the short-blade (A4) is installed, the heat sink having plain surfaces, consumes about 32 W at a flow rate of 36 LPS (76 CFM). With the agitator turned on, the system can achieve much lower thermal resistance with a smaller power consumption of 31 W at around 30 LPS (63 CFM). This indicates that employing the piezoelectric translational agitator is a much more efficient way to enhance heat transfer than just increasing the flow rate through the heat sink channels. In addition, the micro pin-fin heat sink with the agitator off consumes about the same flow power, 31 W, but provides lower thermal resistance (0.084 °C/W) compared

to the agitated plain surface heat sink system (0.103 °C/W) at the same flow rate of 30 LPS (63 CFM). When the heat sink is helped by both the agitator (A4) and micro pin-fin surfaces and operated at 30 LPS (63 CFM), the active heat sink can achieve a 39 % decrease in thermal resistance compared to the non-agitated (A2) plain surface heat sink operated at a flow rate of 36 LPS, or 76 CFM, with the same total power consumption of 43 W. Therefore, the results of the present study suggest that the active heat sink system with the piezoelectric translational agitator and micro pin-fin surfaces can offer much more efficient cooling with less power consumption than the non-agitated plain surface heat sink with a powerful fan or blower. Table 6.3 summarizes the required pumping power for channel flow and the electrical power consumption of the agitators for all the test conditions in the present study.

Table 6.3: Summary of the flow pumping power and agitator electrical power consumptions

Heat Sink type	Flow rate (CFM)	Flow pumping power (W)	Agitator condition (type, on/off)	Agitator power consumption (W)	Total power consumption (W)
Plain	56	16.7	A2, off	0	16.7
Plain	56	17.1	A2, on	2.5	19.6
Plain	63	19.3	A4, off	0	19.3
Plain	66	22.3	A4, off	0	22.3
Plain	76	32.3	A4, off	0	32.3
Micro	64	31.0	A3, off	0	31.0
Micro	64	33.0	A3, on	5.0	38.0
Micro	69	40.0	A3, on	5.0	45.0
Micro	76	54.0	A3, off	0	54.0
Micro	76	54.0	A3, on	5.0	59.0
Micro	63	31.4	A4, off	0	31.4
Micro	73	50.2	A4, off	0	50.2
Micro	76	56.1	A4, off	0	56.1
Micro	63	32.1	A4, on	11.2	43.3
Micro	66	36.9	A4, on	11.2	48.1
Micro	76	56.4	A4, on	11.2	67.6

6.7 Conclusion

Active heat sink systems combined with piezoelectric translational agitators and micro pin fin arrays were proposed and cooling performance was demonstrated. The piezoelectric translational agitator provides strong agitation to the flow inside the heat sink channels by oscillating a blade with high-frequency and large displacement. The micro pin fin arrays on the surfaces of the heat sink dramatically increase heat transfer area as well as directly disturb the thermal boundary layer on the heat sink wall. Agitators with different blade structures were tried. The active heat sink system with the short-blade agitator operating at 800 Hz and with micro pin fin arrays reached a thermal resistance of 0.065 °C/W at a flow rate of 76 CFM. This was 45 % reduction in thermal resistance compared with that of the non-agitated plain surface heat sink system operating at the same flow rate. In addition, the results indicate that utilizing the agitator and micro pin fins is a more efficient method than just adding more blower power to the non-agitated plain surface heat sink to achieve same cooling capability.

Chapter 7:
Conclusions

7.1 Summaries

The objective of current study is to develop and demonstrate the powerful active heat sink system that can push the limit of air cooling scheme to the extreme for high power electronics. The active component of the system denotes a piezoelectric translational flow agitator that can be embedded between the heat sink fins and boost convective heat transfer of heated surfaces coupled with an external blower or fan. In addition to this, micro pin-fin surfaces are introduced onto the heat sink surfaces that allow remarkable increase of heat transfer area.

In Chapter 2, detailed discussion about the driving mechanism of the translational agitator is presented. This includes vibrational and structural analyses of the agitator that are performed through analytical and experimental methods. The piezoelectric actuator with high frequency, large displacement, and low power consumption was successfully designed and fabricated based on the flexural oval loop shell structure. The shell amplifies the displacement of the piezo stack actuator and generates dynamic translational movement using resonant energy of the structure. In order to enhance fatigue strength of the actuator, shot peening was applied to the surfaces of the oval loop shells. A detailed fatigue analysis is provided and results show that the given oval loop shell piezo actuators are secure for the agitator purpose. The theoretical solution is proposed to predict the natural frequencies of the oval loop shell actuator and shows a

maximum error of around 14 % compared to the results of experiments. The calculated actuator efficiency is around 50 % when the minimal load of 3.1 g is applied to shell 3 with an applied voltage of 140 V. The operating conditions, such as the resonance frequency and the amplified displacement, can be easily controlled to fulfill needs of specific applications by changing the design parameters.

In Chapter 3, thermal performance of the agitator over the plain surface demonstrated at single channel heat transfer experiments is provided. Four PTA designs are fabricated and tested in a single channel heat transfer facility. The operating frequencies of the four PTAs range from 596 Hz to 1080 Hz with amplified displacements of up to 1.8 mm. The cooling performance of each PTA is tested in a channel flow situation with one side heated and through-flow rates of between 10 LPM and 60 LPM, representing laminar to turbulent flows. The best cooling performance is provided by the system operated with 1.4 mm displacement and 60 LPM. This is a 55% improvement in heat transfer coefficient compared to the non-agitated state with the same channel flow. The required power to drive the flows through the single channel ranges between 0.003 W and 0.274 W at different experimental conditions.

It is shown that the proposed agitators with the single-blade carbon fiber structure demonstrate excellent capability to enhance the traditional fan-cooled heat sink or to operate as a stand-alone cooling device. For collapsing the data, a PTA Reynolds number and a total Reynolds number are defined to characterize the combined effects of cross flow and agitation. Measured heat transfer coefficients from all the test conditions fit with a linear relationship in terms of total Reynolds number. This relationship gave a Stanton

number that allows predicting the operating performance of the PTA-activated cooling module.

Of particular interest is to figure out thermal characteristics of the agitation effects over micro pin-fin surfaces, and to compare them to cases with plain surfaces. Therefore, in Chapter 4, heat transfer and pressure drop aspects of micro pin fin arrays in a rectangular channel with large tip clearances are studied experimentally. The copper micro pin fin arrays are fabricated on the copper substrate using the LIGA photolithography process. Heat transfer experiments are conducted with the channel flow rates used for the agitator test in the single channel. As a result, in the group with smaller micro pin fin heights of 150 μm and 250 μm, a larger diameter tends to provide a higher heat transfer rate when the coefficients are calculated based on the base area. On the other hand, the effect of diameter on heat transfer becomes less important in the group with larger micro pin fin heights of 350 μm and 400 μm. The maximum heat transfer enhancement of 79% is achieved from the micro pin fin arrays with a height of 250 μm and a diameter of 400 μm. The main contribution is to the enhancement is fluid dynamic effects rather than area increase. The fluid dynamic effects to enhance heat transfer performance become more significant at higher Reynolds numbers. The case of H400D250, which has the largest area increase rate of 103%, shows the second highest heat transfer rate. Pressure drop tends to increase with decreasing pin fin diameter, since a smaller pin fin diameter provides larger friction area at a fixed pin fin height and *S/D* ratio. Performance ratio analyses suggest that the cases of H250D400 and H400D250 are

the best micro pin fin arrays of the current study in terms of both heat transfer and pressure drop aspects.

In Chapter 5, the cooling system that combines both the agitators and micro pin-fin surfaces is studied. The intensive heat transfer experiments were performed to verify the performance of the proposed system in the single channel test facility. The performance index of eleven micro pin-fin surfaces was compared in Chapter 4. As a result, the micro pin-fin surfaces H400D250 and H250D400 were selected for the heat transfer experiments with the piezoelectric translational agitator in a single channel. The agitator operating at 920 Hz with a peak-to-peak displacement of 1.4 mm improves heat transfer coefficients of surface H400D250 by 150 and 130 % at channel flow rates of 40 and 60 LPM, compared to the non-agitated plain surface. The corresponding pressure drops across the test section of the single channel facility are measured and compared. It is confirmed that agitation does not increase pressure drop regardless of operating frequency. However, a channel flow rate has a significant impact on increasing pressure drop. In order to consider the effects of cross flow and translational agitation at the same time on the cooling performance of the system, analyses based on the total Reynolds number and Stanton number are conducted. Each surface has its own Stanton number that characterizes thermal performance. As a result, the micro pin-fin surface H400D250 with translational agitation and channel flow improves the overall cooling capability about 91% over that of the plain surface. The virtual active heat sink module aided with the agitator and micro pin-fin surfaces is proposed and its thermal performance is estimated based on the heat transfer coefficients measured in the single channel. The proposed

virtual active heat sink module with 26 arrays of channels installed with 52 agitator blades is shown to provide a thermal resistance of around 0.04 °C/W at its best operating condition.

In Chapter 6, the actual active heat sink module is introduced with a multiple-blade agitator system. Thermal performance and required power to drive the entire active heat sink module is discussed. Agitators with different blade structures are tried. The active heat sink system with the short-blade agitator operating at 800 Hz and with micro pin fin arrays achieved a 45 % reduction in thermal resistance compared with that of the non-agitated plain surface heat sink system. The results suggest that utilizing the active heat sink system with piezoelectric agitators and micro pin-fin surfaces is a more efficient way than using the plain heat sink with increased blower power to achieve the same cooling capability.

7.2 Recommendations

In this study, the idea of the active heat sink technology has been proposed and realized. The intensive experimental works have been done to demonstrate the thermal performance of the system for advancing it to a real application. The theoretical analyses on the oval loop shell structures provided reasonable predictions for the operating frequency of the piezoelectric translational agitator within an error of 5% for the second resonance mode. The total Reynolds number and Stanton number enabled the estimation of the thermal performance at given operating conditions and size of the system. One of the final goals of this study is to develop the design loop for the piezoelectric translational agitator when the required cooling capability is known with a given heat

sink design. Figure 7.1 shows the design loop of the piezoelectric translational agitator.

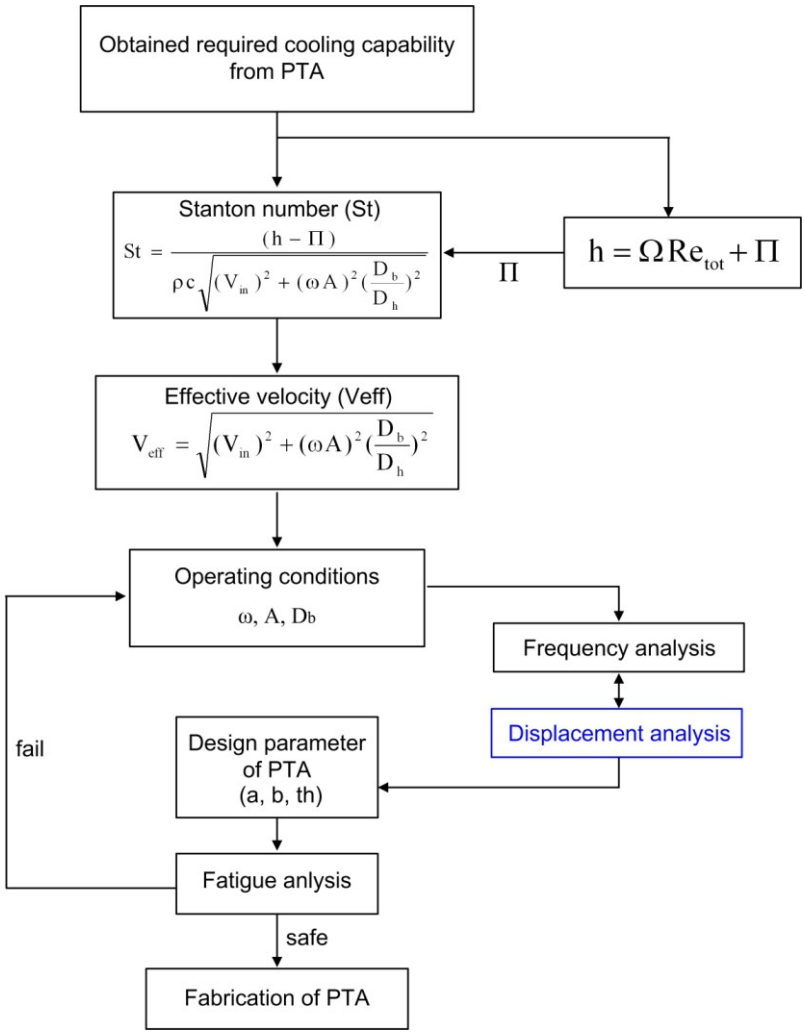

Figure 7.1: Design loop of the piezoelectric translational agitator.

The required improvement of the cooling capability of the heat sink due to the agitator is obtained first in terms of average heat transfer coefficient. Based on the empirical relationships between the total Reynolds number and estimated heat transfer coefficients, the Stanton number could be calculated. The sets of required operating conditions of the PTA such as resonance frequencies, displacements, and blade sizes are decided from the Stanton number and effective velocity calculations. Then, the design

parameters of the PTA could be found by conducting theoretical analyses on frequency and displacement estimations. Then, the fatigue limit of the PTA is performed. If the PTA turns out to be safe within fatigue limit of the structure, the fabrication process is followed with the given design parameters. Otherwise, other sets of operating conditions and design parameters are tried until the fatigue strength is satisfied. In order for this design loop to be possible, the theoretical method for estimating dynamic displacement of the agitator is necessary. The displacement could be computed by solving Equation (2.23) the motion equations of the PTA. To solve these equations for the displacements of x_1 and x_2, the damping coefficient, C_{eq}, and the initial force generation, F_o, of the oval loop shell in the agitation direction should be addressed.

In the heat transfer aspect, the present study focused on intensive experimental studies in the single- and multiple-channel heat sinks. However, the study on the mechanisms of the heat transfer enhancement due to the translational agitation was relatively out of focus. Therefore, the theoretical and numerical studies on revealing the heat transfer mechanisms of the plain or micro pin-fin surfaces under translational agitations will be desirable to better understand the proposed active cooling scheme. This may include the investigations on thermal boundary layer behavior under the agitation effects, the detailed flow fields around the oscillating blades with channel flows, turbulence generations, etc. In addition, the study on electrical aspects of the piezoelectric translational agitator will be helpful to further optimize the agitator's performance. Moreover, developing a frequency- and displacement-tunable piezoelectric translational agitator would be an advanced and interesting topic. This would require profound

theoretical and experimental investigations utilizing many advanced control methodologies.

References

[1] A. Bar-Cohen, State-of-the-Art and Trends in the Thermal Packaging of Electronic Equipment, Journal of Electronic Packaging, 114(3) (1992) 257-270.

[2] Wikipedia, List of CPU power dissipation, in.

[3] J. Francom, D. Turner, Military's Demands Drive Innovative Thermal Management Solutions, in: Power Electronics Technology, Penton Media, Inc., 2011.

[4] S.C. Mohapatra, D. Loikits, Advances in liquid coolant technologies for electronics cooling, in: Semiconductor Thermal Measurement and Management Symposium, 2005 IEEE Twenty First Annual IEEE, 2005, pp. 354-360.

[5] T.E. Salem, D. Porschet, S.B. Bayne, Thermal performance of water-cooled heat sinks: a comparison of two different designs, in: Semiconductor Thermal Measurement and Management Symposium, 2005 IEEE Twenty First Annual IEEE, 2005, pp. 264-269.

[6] P. Wu, W.A. Little, Measurement of the heat transfer characteristics of gas flow in fine channel heat exchangers used for microminiature refrigerators, Cryogenics, 24(8) (1984) 415-420.

[7] J. Pfahler, J. Harley, H. Bau, J. Zemel, Liquid transport in micron and submicron channels, Sensors and Actuators A: Physical, 22(1-3) (1989) 431-434.

[8] H.Y. Zhang, D. Pinjala, T.N. Wong, K.C. Toh, Y.K. Joshi, Single-phase liquid cooled microchannel heat sink for electronic packages, Applied Thermal Engineering, 25(10) (2005) 1472-1487.

[9] J. Linan, W. Man, Y. Zohar, Phase change in microchannel heat sinks with integrated temperature sensors, Microelectromechanical Systems, Journal of, 8(4) (1999) 358-365.

[10] J. Linan, W. Man, Z. Yitshak, Forced convection boiling in a microchannel heat sink, Journal of Microelectromechanical Systems, 10(1) (2001) 80-87.

[11] K.C. Marston, M. Gaynes, R.J. Bezama, E.G. Colgan, A Practical Implementation of Silicon Microchannel Coolers, in: ElectronicsCooling, 2007.

[12] S.-F. Liu, R.-T. Huang, W.-J. Sheu, C.-C. Wang, Heat transfer by a piezoelectric fan on a flat surface subject to the influence of horizontal/vertical arrangement, International Journal of Heat and Mass Transfer, 52(11-12) (2009) 2565-2570.

[13] R.L. Webb, Nucleate Boiling on Porous Coated Surfaces, Heat Transfer Engineering, 4(3-4) (1981) 71-82.

[14] P.J. Berenson, Experiments on pool-boiling heat transfer, International Journal of Heat and Mass Transfer, 5(10) (1962) 985-999.

[15] K.-H. Sun, J.H. Lienhard, The peak pool boiling heat flux on horizontal cylinders, International Journal of Heat and Mass Transfer, 13(9) (1970) 1425-1439.

[16] N. Bakhru, J.H. Lienhard, Boiling from small cylinders, International Journal of Heat and Mass Transfer, 15(11) (1972) 2011-2025.

[17] P.J. Marto, V.J. Lepere, Pool Boiling Heat Transfer From Enhanced Surfaces to Dielectric Fluids, Journal of Heat Transfer, 104(2) (1982) 292-299.

[18] S.K.R. Chowdhury, R.H.S. Winterton, Surface effects in pool boiling, International Journal of Heat and Mass Transfer, 28(10) (1985) 1881-1889.

[19] M. Arik, A. Bar-Cohen, S.M. You, Enhancement of pool boiling critical heat flux in dielectric liquids by microporous coatings, International Journal of Heat and Mass Transfer, 50(5-6) (2007) 997-1009.

[20] I. Mudawar, Direct-immersion cooling for high power electronic chips, in: Thermal Phenomena in Electronic Systems, 1992. I-THERM III, InterSociety Conference on, 1992, pp. 74-84.

[21] S.M. You, T.W. Simon, A. Bar-Cohen, A technique for enhancing boiling heat transfer with application to cooling of electronic equipment, Components, Hybrids, and Manufacturing Technology, IEEE Transactions on, 15(5) (1992) 823-831.

[22] S.M. You, J.H. Kim, K.H. Kim, Effect of nanoparticles on critical heat flux of water in pool boiling heat transfer, Applied Physics Letters, 83(16) (2003) 3374-3376.

[23] S.M. Kwark, R. Kumar, G. Moreno, J. Yoo, S.M. You, Pool boiling characteristics of low concentration nanofluids, International Journal of Heat and Mass Transfer, 53(5-6) (2010) 972-981.

[24] T.A. Shedd, A.G. Pautsch, Spray impingement cooling with single- and multiple-nozzle arrays. Part II: Visualization and empirical models, International Journal of Heat and Mass Transfer, 48(15) (2005) 3176-3184.

[25] M. Fabbri, V.K. Dhir, Optimized Heat Transfer for High Power Electronic Cooling Using Arrays of Microjets, Journal of Heat Transfer, 127(7) (2005) 760-769.

[26] S. Toda, A study of mist cooling, Heat Transfer: Japanese Research, 1 (1972) 39-50.

[27] C. Bonacina, G. Comini, S. Del Giudice, Evaporation of atomized liquid on hot surfaces, Letters in Heat and Mass Transfer, 2(5) (1975) 401-406.

[28] B. Elison, B.W. Webb, Local heat transfer to impinging liquid jets in the initially laminar, transitional, and turbulent regimes, International Journal of Heat and Mass Transfer, 37(8) (1994) 1207-1216.

[29] K.A. Estes, I. Mudawar, Correlation of sauter mean diameter and critical heat flux for spray cooling of small surfaces, International Journal of Heat and Mass Transfer, 38(16) (1995) 2985-2996.

[30] Y. Pan, B.W. Webb, Heat Transfer Characteristics of Arrays of Free-Surface Liquid Jets, Journal of Heat Transfer, 117(4) (1995) 878-883.

[31] K. Oliphant, B.W. Webb, M.Q. McQuay, An experimental comparison of liquid jet array and spray impingement cooling in the non-boiling regime, Experimental Thermal and Fluid Science, 18(1) (1998) 1-10.

[32] M. Fabbri, S. Jiang, V.K. Dhir, A Comparative Study of Cooling of High Power Density Electronics Using Sprays and Microjets, Journal of Heat Transfer, 127(1) (2005) 38-48.

[33] L. Lin, R. Ponnappan, Heat transfer characteristics of spray cooling in a closed loop, International Journal of Heat and Mass Transfer, 46(20) (2003) 3737-3746.

[34] M. Visaria, I. Mudawar, Theoretical and experimental study of the effects of spray inclination on two-phase spray cooling and critical heat flux, International Journal of Heat and Mass Transfer, 51(9-10) (2008) 2398-2410.

[35] M. Visaria, I. Mudawar, Application of Two-Phase Spray Cooling for Thermal Management of Electronic Devices, Components and Packaging Technologies, IEEE Transactions on, 32(4) (2009) 784-793.

[36] A.G. Pautsch, T.A. Shedd, Spray impingement cooling with single- and multiple-nozzle arrays. Part I: Heat transfer data using FC-72, International Journal of Heat and Mass Transfer, 48(15) (2005) 3167-3175.

[37] C.D. Jones, L.F. Smith, Optimum Arrangement of Rectangular Fins on Horizontal Surfaces for Free-Convection Heat Transfer, Journal of Heat Transfer, 92(1) (1970) 6-10.

[38] A.T. Morrison, Optimization of heat sink fin geometries for heat sinks in natural convection, in: Thermal Phenomena in Electronic Systems, 1992. I-THERM III, InterSociety Conference on, 1992, pp. 145-148.

[39] R.-T. Huang, W.-J. Sheu, C.-C. Wang, Orientation effect on natural convective performance of square pin fin heat sinks, International Journal of Heat and Mass Transfer, 51(9-10) (2008) 2368-2376.

[40] A. Bar-Cohen, M. Iyengar, A.D. Kraus, Design of Optimum Plate-Fin Natural Convective Heat Sinks, Journal of Electronic Packaging, 125(2) (2003) 208-216.

[41] S.-H. Yu, K.-S. Lee, S.-J. Yook, Optimum design of a radial heat sink under natural convection, International Journal of Heat and Mass Transfer, 54(11-12) (2011) 2499-2505.

[42] E.A.M. Elshafei, Natural convection heat transfer from a heat sink with hollow/perforated circular pin fins, Energy, 35(7) (2010) 2870-2877.

[43] F. Harahap, D. Setio, Correlations for heat dissipation and natural convection heat-transfer from horizontally-based, vertically-finned arrays, Applied Energy, 69(1) (2001) 29-38.

[44] C. Hilbert, S. Sommerfeldt, O. Gupta, D.J. Herrell, High performance air cooled heat sinks for integrated circuits, Components, Hybrids, and Manufacturing Technology, IEEE Transactions on, 13(4) (1990) 1022-1031.

[45] M. Behnia, D. Copeland, D. Soodphakdee, A comparison of heat sink geometries for laminar forced convection: Numerical simulation of periodically developed flow, in: Thermal and Thermomechanical Phenomena in Electronic Systems, 1998. ITHERM '98. The Sixth Intersociety Conference on, 1998, pp. 310-315.

[46] D. Soodphakdee, M. Behnia, D.W. Copeland, A Comparison of Fin Geometries for Heatsinks in Laminar Forced Convection: Part I - Round, Elliptical, and Plate Fins in Staggered and In-Line Configurations, The International Journal of Microcircuits and Electronic Packaging, 24(1) (2001) 68-76.

[47] S. Al-Sanea, A numerical study of the flow and heattransfer characteristics of an impinging laminar slot-jet including crossflow effects, International Journal of Heat and Mass Transfer, 35(10) (1992) 2501-2513.

[48] F.J. Higuera, M. Martinez, An incompressible jet in a weak crossflow, Journal of Fluid Mechanics, 249 (1993) 73-97.

[49] A.J. Humber, E.W. Grandmaison, A. Pollard, Mixing between a sharp-edged rectangular jet and a transverse cross flow, International Journal of Heat and Mass Transfer, 36(18) (1993) 4307-4316.

[50] L.B.Y. Aldabbagh, I. Sezai, A.A. Mohamad, Three-Dimensional Investigation of a Laminar Impinging Square Jet Interaction With Cross-Flow, Journal of Heat Transfer, 125(2) (2003) 243-249.

[51] A. Glezer, M. Amitay, SYNTHETIC JETS, Annual Review of Fluid Mechanics, 34(1) (2002) 503-529.

[52] B.L. Smith, A. Glezer, The formation and evolution of synthetic jets, Physics of Fluids, 10(9) (1998) 2281-2297.

[53] N. Beratlis, M.K. Smith, Optimization of synthetic jet cooling for microelectronics applications [VCSEL array example], in: Semiconductor Thermal Measurement and Management Symposium, 2003. Ninteenth Annual IEEE, 2003, pp. 66-73.

[54] R. Mahalingam, N. Rumigny, A. Glezer, Thermal management using synthetic jet ejectors, Components and Packaging Technologies, IEEE Transactions on, 27(3) (2004) 439-444.

[55] R. Mahalingam, Modeling of Synthetic Jet Ejectors for Electronics Cooling, in: Semiconductor Thermal Measurement and Management Symposium, 2007. SEMI-THERM 2007. Twenty Third Annual IEEE, 2007, pp. 196-199.

[56] Y. Wang, G. Yuan, Y.K. Yoon, M.G. Allen, S.A. Bidstrup, Active cooling substrates for thermal management of microelectronics, Components and Packaging Technologies, IEEE Transactions on, 28(3) (2005) 477-483.

[57] A. Pavlova, M. Amitay, Electronic Cooling Using Synthetic Jet Impingement, Journal of Heat Transfer, 128(9) (2006) 897-907.

[58] M. Arik, Local Heat Transfer Coefficients of a High-Frequency Synthetic Jet during Impingement Cooling over Flat Surfaces, Heat Transfer Engineering, 29(9) (2008) 763-773.

[59] M. Chaudhari, B. Puranik, A. Agrawal, Effect of orifice shape in synthetic jet based impingement cooling, Experimental Thermal and Fluid Science, 34(2) (2010) 246-256.

[60] M. Chaudhari, B. Puranik, A. Agrawal, Heat transfer characteristics of synthetic jet impingement cooling, International Journal of Heat and Mass Transfer, 53(5-6) (2010) 1057-1069.

[61] M. Toda, S. Osaka, Vibrational fan using the piezoelectric polymer PVF2, in: Proceedings of the IEEE, 1979, pp. 1171-1173.

[62] J.H. Yoo, J.I. Hong, W. Cao, Piezoelectric ceramic bimorph coupled to thin metal plate as cooling fan for electronic devices, Sensors and Actuators A: Physical, 79(1) (2000) 8-12.

[63] T. Açikalin, S.M. Wait, S.V. Garimella, A. Raman, Experimental Investigation of the Thermal Performance of Piezoelectric Fans, Heat Transfer Engineering, 25(1) (2004) 4-14.

[64] S.M. Wait, S. Basak, S.V. Garimella, A. Raman, Piezoelectric Fans Using Higher Flexural Modes for Electronics Cooling Applications, Components and Packaging Technologies, IEEE Transactions on, 30(1) (2007) 119-128.

[65] T. Açikalin, S.V. Garimella, Analysis and Prediction of the Thermal Performance of Piezoelectrically Actuated Fans, Heat Transfer Engineering, 30(6) (2009) 487-498.

[66] M. Kimber, S.V. Garimella, A. Raman, Local Heat Transfer Coefficients Induced by Piezoelectrically Actuated Vibrating Cantilevers, Journal of Heat Transfer, 129(9) (2007) 1168-1176.

[67] J. Petroski, M. Arik, M. Gursoy, Optimization of Piezoelectric Oscillating Fan-Cooled Heat Sinks for Electronics Cooling, Components and Packaging Technologies, IEEE Transactions on, 33(1) (2010) 25-31.

[68] C. Niezrecki, D. Brei, S. Balakrishnan, A. Moskalik, Piezoelectric Actuation: State of the Art, The Shock and Vibration Digest, 33(4) (2001) 269-280.

[69] J.H. Yoo, J.I. Hong, W. Cao, Piezoelectric ceramic bimorph coupled to thin metal plate as cooling fan for electronic devices, Sensors and Actuators A, 79 (2000) 8-12.

[70] L.Q. Yao, J.G. Zhang, L. Lu, M.O. Lai, Nonlinear static characteristics of piezoelectric bending actuators under strong applied electric field, Sensors and Actuators A, 115 (2004) 168-175.

[71] J. Friend, A. Umeshima, T. Ishii, K. Nakamura, S. Ueha, A piezoelectric linear actuator formed from a multitude of bimorphs, Sensors and Actuators A, 109 (2004) 242-251.

[72] T. Acikalin, S.M. Wait, S.V. Garimella, A. Raman, Experimental investigation of the thermal performance of piezoelectric fans, Heat Transfer Engineering, 25(1) (2004) 4-14.

[73] C. Cadou, B. Zhang, Performance modeling of a piezo-hydraulic actuator, Journal of Intelligent Material Systems and Structures, 14 (2003) 149-160.

[74] J.E. Lindler, E.H. Anderson, M.E. Regelbrugge, Design and testing of piezoelectric-hydraulic actuators, in: SPIE Smart Structures and Materials Symposium, Industrial and Commercial Applications of Smart Structures Technology, San Diego, CA, USA, 2003, pp. 96-107.

[75] H.S. Yoon, G. Washington, A millimeter-stroke piezoelectric hybrid actuator using hydraulic displacement amplification mechanism, in: IEEE International Symposium on Industrial Electronics, Montreal, Quebec, Canada, 2006, pp. 2809-2813.

[76] J. Garcia-Bonito, M.J. Brennan, S.J. Elliott, A. David, A novel high-displacement piezoelectric actuator for active vibration control, Smart Materials and Structures, 7 (1998) 31-42.

[77] Y.B. Ham, W.S. Seo, W.Y. Cho, D.W. Yun, J.H. Park, S.N. Yun, Development of a piezoelectric pump using hinge-lever amplification mechanism, Journal of Electroceramics, 23 (2009) 346-350.

[78] M. Joshi, S. Priya, Piezo-Bow: High Displacement and High Blocking Force Actuator, Integrated Ferroelectrics, 82 (2006) 25-43.

[79] H.W. Ma, S.M. Yao, L.Q. Wang, Z. Zhong, Analysis of the displacement amplification ratio of bridge-type flexure hinge, Sensors and Actuators A, 132 (2006) 730-736.

[80] E. Furukawa, M. Mizuno, T. Doi, Development of a flexure-hinged translational mechanism driven by two piezoelectric stacks, JSME International Series C, Dynamics, Control, Robotics, Design and Manufacturing, 38 (1995) 743-748.

[81] J. Juuti, K. Kordas, R. Lonnakko, V.-P. Moilanen, S. Leppavuori, Mechanically amplified large displacement piezoelectric actuators, Sensors and Actuators A, 120 (2005) 225-231.

[82] J. Mulling, T. Usher, B. Dessent, J. Ralmer, P. Franzon, E. Grant, A. Kingon, Load characterization of high displacement piezoelectric actuators with various end conditions, Sensors and Actuators A, 94 (2001) 19-24.

[83] J.H. Kim, S.H. Kim, Y.K. Kwak, Development and optimization of 3-D bridge-type hinge mechanisms, Sensors and Actuators A, 116 (2004) 530-538.

[84] K.H. Lam, X.X. Wang, H.L.W. Chan, Lead-free piezoceramic cymbal actuator, Sensors and Actuators A, 125 (2006) 393-397.

[85] M. Muraoka, S. Sanada, Displacement amplifier for piezoelectric actuator based on honeycomb link mechanism, Sensors and Actuators A, 157 (2010) 84-90.

[86] D. Neal, H.H. Asada, Dynamic Performance of Nonlinear 100X Displacement Amplification Piezoelectric Actuator, in: ASME 2010 Dynamic Systems and Control Conference, Cambridge, Massachusetts, USA, 2010, pp. 65-72.

[87] J. Ueda, T.W. Secord, H.H. Asada, Large Effective-Strain Piezoelectric Actuators Using Nested Cellular Architecture With Exponential Strain Amplification Mechanisms, Mechatronics, IEEE/ASME Transactions on, 15(5) (2010) 770-782.

[88] CEDRAT Technologies, in.

[89] A.S. Grinspan, R. Gnanamoorthy, Effect of oil jet peening duration on surface modification and fatigue behavior of medium carbon steel, AISI 1040, Materials Science and Engineering A, 456 (2007) 210-217.

[90] M.L. Aggarwall, R.A. Khan, V.P. Agrawal, Investigation into the effects of shot peening on the fretting fatigue behavior of 65Si7 spring steel leaf springs, J. Materials: Design and Applications, 219 (2004) 139-147.

[91] H. Mano, S. Kondo, A. Matsumuro, Microstructured surface layer induced by shot peening and its effect on fatigue strength, Transactions of Japan Society of Spring Engineers, 51(17-20) (2006).

[92] V. Sabelkin, S.A. Martinez, S. Mall, S. Sathish, M.P. Blodgett, Effects of shot-peening intensity on fretting fatigue crack-initiation behaviour of Ti-6Al-4V, in: Fatigue & Fracture of Engineering Materials & Structures, Wiley-Blackwell, 2005, pp. 321-332.

[93] T. Jordan, Z. Ounaies, J. Tripp, P. Tcheng, Electrical Properties and Power Considerations of a Piezoelectric Actuator, 2000.

[94] S. Timoshenko, Strength of Materials, Third ed., D. Van Nostrand Company, Inc., 1955.

[95] Piezo Nano Positioning, in: P. Instrumente (Ed.).

[96] R.C. Juvinall, K.M. Marshek, Fundamentals of Machine Component Design, Third Edition ed., John Wiley & Sons, Inc.

[97] A. Mehmet, An investigation into feasibility of impingement heat transfer and acoustic abatement of meso scale synthetic jets, Applied Thermal Engineering, 27(8) (2007) 1483-1494.

[98] A. Selamet, M.B. Xu, I.J. Lee, N.T. Huff, Analytical approach for sound attenuation in perforated dissipative silencers with inlet/outlet extensions, The Journal of the Acoustical Society of America, 117(4) (2005) 2078-2089.

[99] M.K. Chyu, Heat Transfer and Pressure Drop for Short Pin-Fin Arrays With Pin-Endwall Fillet, Journal of Heat Transfer, 112(4) (1990) 926-932.

[100] E.M. Sparrow, J.W. Ramsey, Heat transfer and pressure drop for a staggered wall-attached array of cylinders with tip clearance, International Journal of Heat and Mass Transfer, 21(11) (1978) 1369-1378.

[101] E.M. Sparrow, J.W. Ramsey, C.A.C. Altemani, Experiments on In-line Pin Fin Arrays and Performance Comparisons with Staggered Arrays, Journal of Heat Transfer, 102(1) (1980) 44-50.

[102] D.E. Metzger, R.A. Berry, J.P. Bronson, Developing Heat Transfer in Rectangular Ducts With Staggered Arrays of Short Pin Fins, Journal of Heat Transfer, 104(4) (1982) 700-706.

[103] D.E. Metzger, C.S. Fan, S.W. Haley, Effects of Pin Shape and Array Orientation on Heat Transfer and Pressure Loss in Pin Fin Arrays, Journal of Engineering for Gas Turbines and Power, 106(1) (1984) 252-257.

[104] Y. Peng, Heat Transfer and Friction Loss Characteristics of Pin Fin Cooling Configurations, Journal of Engineering for Gas Turbines and Power, 106(1) (1984) 246-251.

[105] M.K. Chyu, Y.C. Hsing, V. Natarajan, Convective Heat Transfer of Cubic Fin Arrays in a Narrow Channel, Journal of Turbomachinery, 120(2) (1998) 362-367.

[106] Q. Li, Z. Chen, U. Flechtner, H.-J. Warnecke, Heat transfer and pressure drop characteristics in rectangular channels with elliptic pin fins, International Journal of Heat and Fluid Flow, 19(3) (1998) 245-250.

[107] S.C. Siw, M.K. Chyu, T.I.P. Shih, M.A. Alvin, Effects of Pin Detached Space on Heat Transfer and From Pin Fin Arrays, ASME Conference Proceedings, 2010(43994) 491-500.

[108] K.A. Moores, Y.K. Joshi, Effect of Tip Clearance on the Thermal and Hydrodynamic Performance of a Shrouded Pin Fin Array, Journal of Heat Transfer, 125(6) (2003) 999-1006.

[109] C. Marques, K.W. Kelly, Fabrication and Performance of a Pin Fin Micro Heat Exchanger, Journal of Heat Transfer, 126(3) (2004) 434-444.

[110] A. Koşar, C. Mishra, Y. Peles, Laminar Flow Across a Bank of Low Aspect Ratio Micro Pin Fins, Journal of Fluids Engineering, 127(3) (2005) 419-430.

[111] Y. Peles, A. Koşar, C. Mishra, C.-J. Kuo, B. Schneider, Forced convective heat transfer across a pin fin micro heat sink, International Journal of Heat and Mass Transfer, 48(17) (2005) 3615-3627.

[112] R.S. Prasher, J. Dirner, J.-Y. Chang, A. Myers, D. Chau, D. He, S. Prstic, Nusselt Number and Friction Factor of Staggered Arrays of Low Aspect Ratio Micropin-Fins Under Cross Flow for Water as Fluid, Journal of Heat Transfer, 129(2) (2007) 141-153.

[113] M. Liu, D. Liu, S. Xu, Y. Chen, Experimental study on liquid flow and heat transfer in micro square pin fin heat sink, International Journal of Heat and Mass Transfer, 54(25-26) (2011) 5602-5611.

[114] R.S. Prasher, J. Dirner, J.-Y. Chang, A. Myers, D. Chau, D. He, S. Prstic, Thermal Resistance and Pressure Drop of Silicon Based Micro Pin Fin Heat Exchanger Under Cross Flow, ASME Conference Proceedings, 2005(42002) (2005) 717-725.

[115] A. Koşar, Y. Peles, Convective flow of refrigerant (R-123) across a bank of micro pin fins, International Journal of Heat and Mass Transfer, 49(17-18) (2006) 3142-3155.

[116] F.M. White, Viscous Fluid Flow, Third ed., McGraw. Hill.

[117] F.M. White, Fluid Mechanics, Sixth ed., McGraw. Hill.

[118] W. Kays, M. Crawford, B. Weigand, Convective Heat and Mass Transfer, Fourth ed.

[119] Y. Yu, T.W. Simon, M. Zhang, T. Yeom, M.T. North, T. Cui, Enhancing Heat Transfer of Air-Cooled Heat Sinks using Piezoelectrically-Driven Agitators and Synthetic Jets, in: ASME 2011 International Mechanical Engineering Congress and Exposition, Denver, Colorado, USA, 2011.

[120] R.J. Moffat, Using Uncertainty Analysis in the Planning of an Experiment, Journal of Fluids Engineering, 107(2) (1985) 173-178.